

Smectic Phase Transitions in Chiral Liquid Crystals

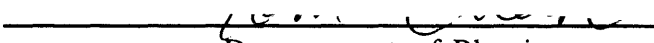
by
Tom Chan

Bachelor of Science in Space Physics
University of Science and Technology of China
July 1986

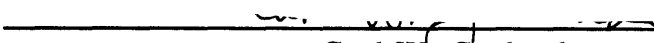
Master of Science in Applied Physics
Columbia University
May 1988

SUBMITTED TO THE DEPARTMENT OF
PHYSICS
IN PARTIAL FULFILLMENT OF THE REQUIREMENTS FOR THE
DEGREE OF
DOCTOR OF PHILOSOPHY IN PHYSICS
at the
Massachusetts Institute of Technology
February 1995
© 1995 Massachusetts Institute of Technology


Signature of Author:


Department of Physics
October 17, 1994


Certified by:


Carl W. Garland
Professor, Department of Chemistry
Thesis Supervisor

Certified by:


A. Nihat Berker
Professor, Department of Physics
Thesis Co-Supervisor

Accepted by:


George F. Koster, Chairman
Departmental Graduate Committee

Science

MASSACHUSETTS INSTITUTE
OF TECHNOLOGY

MAR 02 1995

Smectic Phase Transitions in Chiral Liquid Crystals

by
Tom Chan

Submitted to the Department of Physics on October 17, 1994
in partial fulfillment of the requirements for the Degree of
Doctor of Philosophy in Physics

ABSTRACT

Experimental study on phase transitions in several chiral liquid crystal materials using high-resolution calorimetry is presented.

We analyze high-resolution calorimetry in scanning adiabatic mode, ac mode, and relaxation mode (scanning non-adiabatic mode). Detailed descriptions of a complex calorimeter capable of operating in both ac mode and relaxation mode are given. High-resolution thermal analysis is achieved using qualitative information from ac calorimetry (particularly the phase shift data) and quantitative information of scanning non-adiabatic calorimetry (the effective heat capacity).

Heat capacity measurements with an ac calorimeter are carried out to study the nature of smectic-A to ferroelectric smectic-C* transitions in mixtures of liquid crystals C7 and 1004; the nucleation and growth phenomena in antiferroelectric liquid crystal MHPOCBC; and the phase transitions in twisted-grain-boundary (TGB) materials nFBTFOM. The cholesteric N* to TGB_A transition and TGB_A to SmA transition in liquid crystal 9FBTFOM are studied by a scanning non-adiabatic calorimeter.

Thesis Supervisor: Carl W. Garland
Professor, Department of Chemistry

Thesis Co-Supervisor: A. Nihat Berker
Professor, Department of Physics

Table of Contents

Chapter 1 Introduction

1.1	Structure of Matter.....	7
1.2	States of Matter	8
1.3	Some Simple Liquid Crystals.....	9
1.4	Phase Transitions	15
1.5	Landau Theory of Phase Transitions.....	16
	A. Model 1: System that is not symmetric under inversion of order parameter	18
	B. Model 2: System that is symmetric under inversion of order parameter	23
	C. Some Predictions of Landau Theory	30
1.6	Renormalization Group theory for Phase Transitions.....	31

Chapter 2 High-resolution Calorimetry

2.1	A Simple Model for Thermal Analysis	38
	A. Process without latent heat	41
	B. Process with latent heat.....	42
2.2	Theory of Adiabatic Calorimetry at Constant Pressure.....	48
2.3	Theory of ac Calorimetry at Constant Pressure.....	50
	A. Process without latent heat	50
	B. Process with latent heat.....	55
2.4	Theory of Relaxation Calorimetry at Constant Pressure.....	65
	A. Process without latent heat	66
	B. Measurement of R when there is no latent heat.....	69
	C. Process with latent heat.....	70
2.5	Design and Operation of an ac Calorimeter	71

A. Sample cell	73
B. Temperature control	74
C. Electronic circuitry	77
D. Data acquisition	79
2.6 Design and Operation of a Relaxation Calorimeter	84
A. Sample cell	84
B. Temperature control	85
C. Electronic circuitry	89
D. Computer control	92
E. ac mode of operation	94
F. Relaxation mode of operation	94

Chapter 3 Phase Transitions in Ferroelectric Liquid Crystals

3.1 Ordering in Smectic-C and Smectic-C* Phases	99
3.2 Landau Model for SmA-SmC and SmA-SmC* transitions	100
A. SmA-SmC transitions	100
B. SmA-SmC* transitions	105
3.3 Experiment	107
A. Second-order transitions	111
B. First-order transitions	113
C. Scaling plots	117
3.4 Discussion	117

Chapter 4 Antiferroelectric Liquid Crystals

4.1 Structure and transitions	127
4.2 $\text{SmA} - \text{SmC}_\alpha^* - \text{SmC}_A^*$ transitions	131
4.3 SmC_A to SmI_A transition and freezing	134

Chapter 5 Twisted-Grain-Boundary Phases in Chiral Liquid Crystals

5.1	Structure of TGB_A Phase.....	146
5.2	Experimental Phase Diagram.....	151
5.3	Heat Capacity Data From ac Calorimetry.....	155
	A. Overall view of heat capacity data.....	155
	B. Discussion of the phase shift ϕ	159
	C. Transition temperatures.....	162
	D. Features in N^* phase.....	166
	E. $N_L^* - TGB_A$ transitions.....	166
	F. $TGB_A - SmA$ transitions.....	172
	G. $SmA - SmC^*$ and $TGB_A - SmC^*$ transitions.....	172
5.4	Relaxation Calorimetry Data.....	175
	A. $N^* - TGB_A$ and $TGB_A - SmA$ transitions and feature at T_5	175
	B. $BP_{II} - BP_{III}$ transition.....	180
5.5	Discussion.....	181

Chapter 6 Suggestions for Future Works

6.1	Nonadiabatic Scanning Calorimetry.....	186
6.2	Calorimetry Spectroscopy.....	186

Acknowledgments

I would like to thank Professor Carl W. Garland. Carl has taught me always to keep the highest standards of scientific research. I have benefited greatly from the first-rate research environment of MIT, and the excellent teaching of condensed matter physics by Professors Berker and Kardar.

During my thesis work, I was fortunate to learn many experimental techniques from Drs. Xin Wen, Lei Wu, George Nounesis, Jean-Paul Marcerou, Haruhiko Yao, and Bo Zhou. I especially thank Dr. Haruhiko Yao for broadening my knowledge in many subjects when I worked with him to develop the complex calorimeter. I also found it very useful to study the notes written by Professor Kenji Ema during his stay at MIT.

I am indebted to Professor T.D. Lee for organizing the China-US Physics Exams and Applications (CUSPEA) program which gave me the first chance to pursue graduate study in the United States. The financial supports from Chinese Academy of Sciences in Beijing, fellowships from Columbia University, and research grants from the National Science Foundation and Department of Energy through Columbia and MIT make it possible for me to finish graduate school. I am very grateful to Professor K.C. (John) Chu for rescuing me from a crisis that almost terminated my graduate study in the States.

The early education I received, particularly the undergraduate study at the University of Science and Technology of China (USTC), has been very important for my graduate works. I enjoyed working and learning from many friends at USTC, Columbia and MIT.

Last but not least, I thank my wife Wendy for her love and care.

Chapter 1

Introduction

1.1 Structure of Matter

Physicists have found most of the building blocks of matter. These are quarks, leptons and gauge bosons.¹ The structure of matter is determined by the four fundamental interactions: strong, weak, electromagnetic, and gravitational. Among the four fundamental interactions, strong and weak forces are short-range forces. This means that the interactions are only effective at very small length scales (less than 10^{-15} m). In contrast, electromagnetic and gravitational forces are long-range interactions (their effects reach to very large scales).

Quarks interact with each other through strong forces. The interactions are so strong that no free quark has been found. Quarks bind together to form particles such as protons and neutrons. Protons and neutrons can exist as individual free particles. Or the strong interaction may condense them into a small cluster with a typical size of about 10^{-15} m. We call such clusters nuclei. Because the proton has a positive electrical charge, the nucleus attracts negatively charged electrons by electromagnetic interactions. The most common bound states of nuclei and electrons are atoms and molecules, which are

electrically neutral (the total electric charge is zero) structures with typical sizes in the range 3×10^{-10} m — 30×10^{-10} m. However, atomic and molecular structure can not be explained by classical electromagnetism. Only quantum mechanics gives a satisfactory explanation for the existence of atoms and molecules.

1.2 States of matter

The well-known states of matter are gases, liquids, and solids. In the gas phase, atoms or molecules exist as individual “free” particles and move around independently between collisions. The macroscopic properties of a gas phase are isotropic (they are the same in every direction of three-dimensional space). There is no translational or orientational order among the particles in a gas, and the average interaction between particles is very weak. When the temperature is lowered or the pressure is increased, the particles in a gas can condense into an isotropic liquid state. In this state there is still no ordering of the particles, but they are no longer “free”. Since the system is much denser, every particle is strongly influenced by surrounding particles at a distance of about 5×10^{-10} m. There is almost no free space left in a liquid. As a result, a liquid is almost incompressible whereas a gas has a high compressibility.

An isotropic liquid can develop certain kinds of order when external conditions (temperature, pressure, composition,

electromagnetic fields) change. For some simple molecules, the isotropic liquid changes directly into a crystalline solid on cooling. In the solid state, the average translational position of the molecules is a periodic function in three-dimensional space. However, for some complex molecules, the isotropic liquid does not transform directly into a solid. Instead, partially ordered liquid crystal phases occur between the high-temperature isotropic liquid and the low-temperature fully ordered solid state. The molecular distribution function of a liquid crystal can involve only orientational order or orientational order plus a translational structure that is a periodic function in one or two dimensions.

1.3 Some Simple Liquid Crystal Phases

The states of matter depend not only on external conditions like temperature, pressure, composition, and electromagnetic fields but also on the chemical structure of the constituent particles. A large variety of organic molecules with anisotropic structure exhibit liquid crystal phases.² Such phases occur for either elongated (rod-like) or planar (disk-like) molecules. This thesis is concerned with liquid crystals consisting of elongated molecules. The simplest model for this type of molecule is a rigid rod. One can identify the long axis and the center of mass of the molecule. In the isotropic (I) liquid, there is no long-range order in the translational position

of the center of mass or in the orientational direction of the long axis. As the temperature is decreased, the molecular orientations tend to align in a common direction. Thus the macroscopic properties become uniaxial, with the common orientational direction $\bar{\mathbf{n}}$ called the director (the states $\bar{\mathbf{n}}$ and $-\bar{\mathbf{n}}$ are equivalent). The resulting nematic (N) phase exhibits orientational order but no translational order in the center of mass positions. On further cooling, more ordered smectic phases (layered structures) appear. In these phases, the position of the center of mass has one-dimensional order along the layer normal but no order within the layer. The director is either along the layer normal (parallel to the mass density wave), which is called smectic-A (SmA), or tilted relative to the layer normal which is called smectic-C (SmC).

Nematic phases can exist only in non-chiral materials (no optical activity since there is no distinction between right- and left-handedness). The constituent molecule must be either identical to its mirror image or, if it is not, the system must be a 'racemic' (1:1) mixture of the right- and left-handed species. If the molecule is chiral (i.e., different from its mirror image), there will be a helical structure for the director orientations in the liquid crystal state. As the temperature is decreased, an isotropic liquid can turn into a helical phase called cholesteric (N^*). Locally, a cholesteric is very similar to a nematic, but the distribution of the directors is not uniform and is given by

$\bar{\mathbf{n}} = (\cos(\mathbf{q}_0 z + \phi), \sin(\mathbf{q}_0 z + \phi), 0)$. The structure is periodic along the helical axis (z) and (since the states $\bar{\mathbf{n}}$ and $-\bar{\mathbf{n}}$ are equivalent) the spatial period L is equal to one-half of the pitch: $L = \pi/|\mathbf{q}_0|$. Here we see that chirality acts as a “field” with respect to the natural twisting tendency. That is, the larger the chirality of a molecule, the larger is the value of \mathbf{q}_0 and the shorter the pitch period L . If the molecule is non-chiral, $\mathbf{q}_0 = 0$ and $L = \infty$. It is found that a smectic phase very similar to smectic-C occurs in some chiral materials. The structural difference between this phase, called smectic-C* (SmC^*), and smectic-C is that the tilt of the directors precesses around the layer normal and a helical configuration is obtained; see Fig. 1-1. The SmC phase has monoclinic symmetry:

- there is a plane of symmetry
- there is a twofold symmetry axis C_2 perpendicular to the symmetry plane
- there is an inversion point i .

As for SmC^* , it is obvious that for chiral molecules the symmetry plane and inversion center will be missing. The only symmetry left is the C_2 axis. If the chiral molecule has a dipole moment which has a non-zero component along the C_2 axis, a polarization will appear. Thus, as first noted by R.B. Meyer, SmC^* phases are ferroelectric. The polarization \mathbf{P} is perpendicular to the plane of the layer normal and to the director, and \mathbf{P} precesses to form a helical structure. Applying a

small electric field will unwind the helix and create a macroscopic polarization. These liquid crystals are called ferroelectric liquid crystals (although helielectric would be more accurate).

We will describe more complicated phases that can occur in chiral materials later in this thesis (Chapters 4 and 5). These include antiferroelectric and ferrielectric smectic- C^* (SmC_A^* and SmC_α^*), blue phases (BP_I-BP_{III}), and twisted-grain boundary (TGB_A, TGB_C) phases.

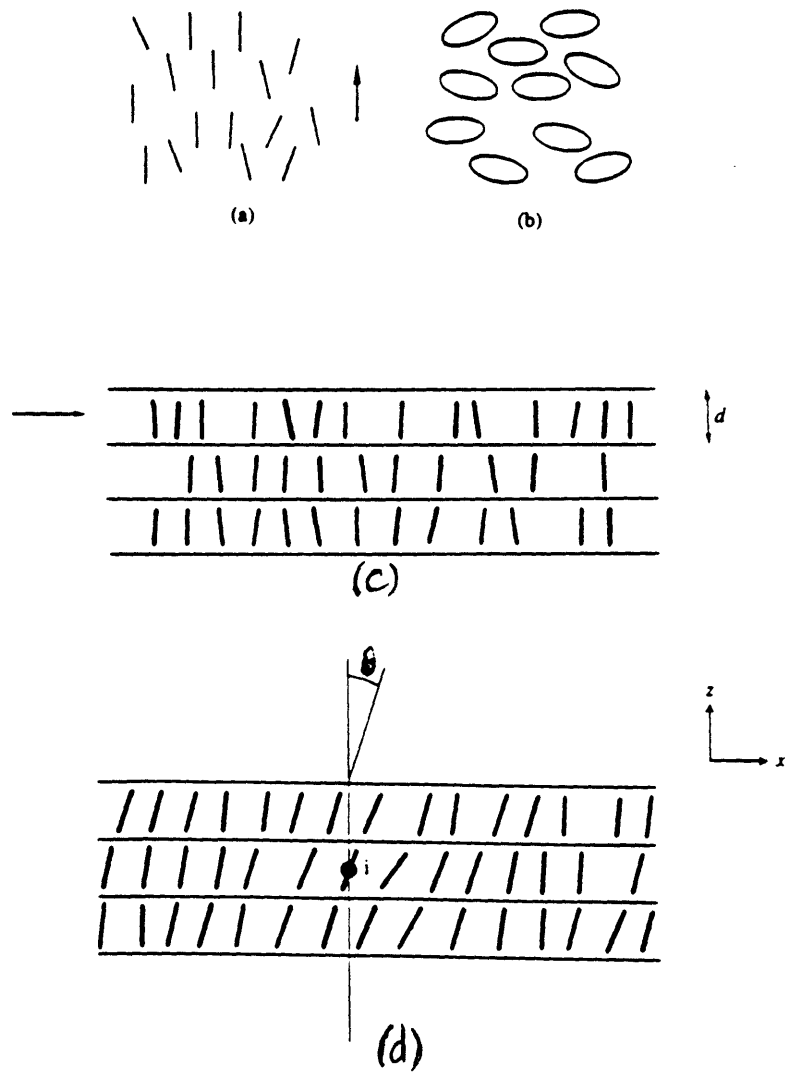


Fig. 1-1. Nematic phase of (a) rod-like molecules and (b) disk-like molecules. (c) Smectic-A layered structure; the director is normal to the layers and there is no translational order within a layer. (d) Smectic-C (director tilt angle θ and inversion point i).

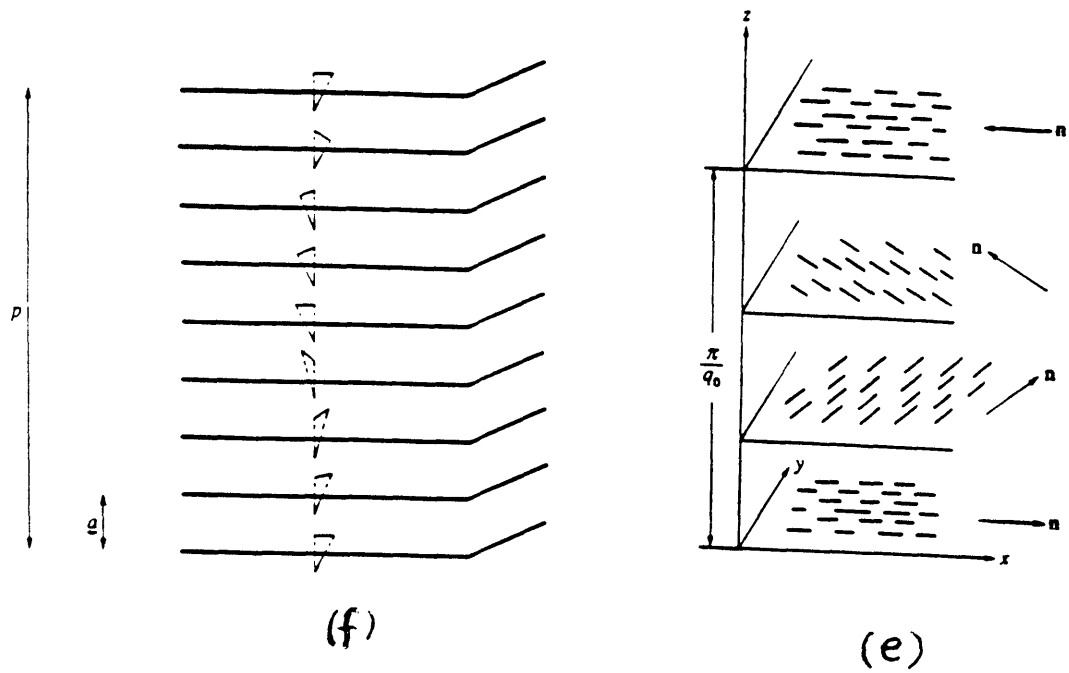


Fig. 1-1. (e) cholesteric (N^*) phase (the planes are guides for the eye and do not have any physical meaning). (f) SmC^* , where the molecular chirality induces a twist in the tilt angle (and in the polarization). The pitch p is much larger than a (typically $p/a \sim 10^3$). Note that p need not to be an exact multiple of a .

1.4 Phase Transitions

Under certain external conditions, the macroscopic properties of a material can change dramatically. The thermodynamic properties may become singular (e.g., divergent), and the material will transform from one state to another. This is called a phase transition. There are two classes of phase transitions: first order and second order. A second-order transition dominated by fluctuation effects is often referred to as exhibiting critical phenomena.

The first derivatives of the Gibbs free energy are $(\partial G/\partial p)_T = V$ and $(\partial G/\partial T)_p = -S$. At a first-order transition, these derivatives (the system volume V and entropy S) change discontinuously: $\Delta V = V_2 - V_1 \neq 0$, $\Delta S = S_2 - S_1 \neq 0$. Note that the Gibbs free energy of the two phases are equal at the transition: $\Delta G = \Delta H - T\Delta S = 0$, thus the latent heat is non-zero: $L = \Delta H = T\Delta S \neq 0$.

At a second-order phase transition, the system volume and entropy are continuous: $\Delta V = 0$, $\Delta S = 0$. Thus there is no latent heat: $L = T\Delta S = 0$. However, the second derivatives of the Gibbs free energy are singular. Thermodynamic properties such as heat capacity $C_p = T(\partial S/\partial T)_p = -T(\partial^2 G/\partial T^2)_p$,

isothermal compressibility $\kappa_T = -\frac{1}{V}(\partial V/\partial p)_T = -\frac{1}{V}(\partial^2 G/\partial p^2)_T$,

and thermal expansion $\alpha = \frac{1}{V}(\partial V/\partial T)_p = \frac{1}{V} \frac{\partial^2 G}{\partial p \partial T}$ diverge at the critical temperature T_c .

The essential distinctions between first and second order phase transitions are:

- A first-order transition has latent heat. Two distinct phases coexist at a first-order transition where their Gibbs free energies are equal. The new phase nucleates and grows within the old phase. A first-order transition often exhibits hysteresis. Metastable phases exist, for example, in supercooling and superheating phenomena.
- A second-order phase transition has no latent heat. There is only one free energy surface. Thus there is no two-phase coexistence, metastability, or hysteresis. Close to a second-order transition, one can observe fluctuations at large length scales (critical phenomenon) and thermodynamic response functions diverge.

1.5 Landau Theory of Phase Transitions

The simplest approach to phase transitions is Landau theory.³ Landau observed that most phase transitions involve a change in the symmetry of the system. If certain symmetry exists in a phase, it can be broken in another more ordered phase. Thus, one can often define a quantity called the order parameter P , which is zero in the more symmetrical (usually high temperature) phase and non-zero in the more ordered (usually low temperature) phase. In this theory, the system free energy is

$$\mathbf{G} = \mathbf{G}_0 + \text{minimum of } \mathbf{L}(\mathbf{P}) \quad (1.1)$$

where $\mathbf{L}(\mathbf{P})$ is an analytic function of \mathbf{P} called the Landau free energy and \mathbf{G}_0 is independent of \mathbf{P} . \mathbf{G}_0 is usually a smooth function of temperature, pressure, composition, and electromagnetic fields and describes the non-configurational (“lattice”) contribution. One can make a Taylor expansion of $\mathbf{L}(\mathbf{P})$ in powers of the order parameter. This expansion is restricted by the symmetry of the system. In the case of a single scalar order parameter \mathbf{P} , the expansion is

$$\mathbf{L}(\mathbf{P}) = \frac{1}{2!} \left(\frac{\partial^2 \mathbf{L}}{\partial \mathbf{P}^2} \right)_{\mathbf{P}=0} \mathbf{P}^2 + \frac{1}{3!} \left(\frac{\partial^3 \mathbf{L}}{\partial \mathbf{P}^3} \right)_{\mathbf{P}=0} \mathbf{P}^3 + \frac{1}{4!} \left(\frac{\partial^4 \mathbf{L}}{\partial \mathbf{P}^4} \right)_{\mathbf{P}=0} \mathbf{P}^4 + \dots \quad (1.2)$$

It is assumed that the coefficients are smooth functions of temperature, pressure, composition, and electromagnetic fields. The first-order term in \mathbf{P} is missing since $\partial \mathbf{L} / \partial \mathbf{P} = \mathbf{0}$; the stable state corresponds to the value of \mathbf{P} that minimizes \mathbf{G} . If we truncate the Taylor series, the last term must be an even power of \mathbf{P} with a positive coefficient, otherwise a global minimum in $\mathbf{L}(\mathbf{P})$ would occur when $|\mathbf{P}| \rightarrow \infty$, whereas we wish to describe how the order parameter rises from zero to a finite value in the ordered phase.

A. Model 1

System That Is Not Symmetric Under Inversion of P

In the case where $L(-P) \neq L(P)$ the odd order terms cannot be excluded. We choose

$$L(P) = \frac{A}{2}P^2 + \frac{B}{3}P^3 + \frac{C}{4}P^4 \quad (1.3)$$

where $C > 0$, $B \neq 0$. It is obvious that $L(P) \rightarrow +\infty$ as $P \rightarrow \pm\infty$. Solving $\partial L / \partial P = 0$, we find three roots at the following P values:

$$P_0 = 0, P_+ = \frac{-B + \sqrt{B^2 - 4AC}}{2C}, P_- = \frac{-B - \sqrt{B^2 - 4AC}}{2C} \quad (1.4)$$

It is convenient to consider three cases (see Fig. 1-2):

1. $B^2 - 4AC < 0$ (which means $A > \frac{B^2}{4C} > 0$). In this case there is only one minimum at $P = 0$ with $L(0) = 0$, $\left. \frac{\partial^2 L}{\partial P^2} \right|_{P=0} = A > 0$, and the system is in the symmetric phase with $P = 0$.

2. $B^2 - 4AC = 0$. Now

$$P_+ = P_- = -\frac{B}{2C} \quad (1.5)$$

which leads to $L(P_{\pm}) = \frac{B^4}{192C^3} > 0$, $\left. \frac{\partial^2 L}{\partial P^2} \right|_{P=P_{\pm}} = \frac{B(B^2 - 4AC)}{8C^2} = 0$.

Thus there is a point of inflection at P_{\pm} . The only minimum is still at $P = 0$.

3. $B^2 - 4AC > 0$. Now P_{\pm} are real numbers. Let us take $B < 0$ ($B > 0$ will give the same result since one can redefine the order parameter $P \rightarrow -P$ and get the same $L(P)$ as with $B < 0$). We have

in this case $P_+ > P_- > 0$ and $\left. \frac{\partial^2 L}{\partial P^2} \right|_{P=P_{\pm}} = \pm P_{\pm} \sqrt{B^2 - 4AC}$.

There is now one more minimum (P_+) and a maximum (P_-). It is possible that the extra minimum will be lower than the one at $P=0$, thus becoming the global minimum. In this case, the system will move into this state through a phase transition and stay in the more ordered phase where the symmetry is broken. The transition occurs when $L(P_+) = L(0) = 0$, and $\partial L / \partial P = 0$. From these two equations we get

$$P_+ = \bar{P} = -\frac{2B}{3C}, \quad A = \frac{2B^2}{9C} > 0 \quad \text{and} \quad \left(\frac{\partial^2 L}{\partial P^2} \right)_{P=\bar{P}} > 0 \quad (1.6)$$

at the transition. So the order parameter changes discontinuously from $P=0$ to $P=\bar{P} = -2B/3C \neq 0$, and the transition point (temperature) is determined by the condition $A = 2B^2/9C$.

Now we calculate the latent heat $L = T_1(S_2 - S_1)$ where T_1 is the transition temperature, S_1 and S_2 are entropies for the two phases at T_1 . The Gibbs free energies are $G_1 = G_0 + L(\bar{P})$ and $G_2 = G_0$ for the phase with $P=0$. Entropy can be obtained from $S_1 = -(\partial G_1 / \partial T)_p = -(\partial G_0 / \partial T)_p - (\partial L(\bar{P}) / \partial T)_p$ and $S_2 = -(\partial G_2 / \partial T)_p = -(\partial G_0 / \partial T)_p$

$$\text{where} \quad \left(\frac{\partial L(\bar{P})}{\partial T} \right)_p = \frac{\partial L}{\partial \bar{P}} \frac{\partial \bar{P}}{\partial T} + \left\{ \frac{1}{2} \frac{\partial A}{\partial T} \bar{P}^2 + \frac{1}{3} \frac{\partial B}{\partial T} \bar{P}^3 + \frac{1}{4} \frac{\partial C}{\partial T} \bar{P}^4 \right\}.$$

The first derivative of $L(P)$ at \bar{P} is zero: $\left. \frac{\partial L}{\partial P} \right|_{P=\bar{P}} = 0$, and $(\partial G_0 / \partial T)_p$

is continuous at the transition. At least one of the coefficients A , B

and C must depend on T , otherwise the transition cannot happen by changing the temperature T .

$$\text{Thus we have } \Delta S = S_2 - S_1 = \frac{1}{2} \frac{\partial A}{\partial T} \bar{P}^2 + \frac{1}{3} \frac{\partial B}{\partial T} \bar{P}^3 + \frac{1}{4} \frac{\partial C}{\partial T} \bar{P}^4 \neq 0.$$

In this model, the order parameter undergoes a discontinuity at the transition, which results in a discontinuity in the entropy S . Thus the transition has a latent heat $L = T_1 \Delta S \neq 0$.

Model 1 can be used to describe many first-order phase transitions. The coefficients A , B and C depend on temperature, pressure, composition, and electromagnetic fields. The transition could be induced by any of these external conditions. In order to describe a temperature induced phase transition, it is a common practice to choose $A = A_0(T - T_0)/T_0$ with $A_0 > 0$ and assume B and C do not depend on temperature T . In this case, the transition condition $A = 2B^2/9C$ yields the transition temperature $T_1 = T_0(1 + 2B^2/9A_0C) > T_0$. (1.7)

Note that in **Model 1** there is a third-order term in the Landau free energy. Whenever there is such a third-order term, the Landau model predicts a first-order transition. In the case of liquid crystals, this situation is realized for the N-I transition. Although there are pretransitional (non-mean field) effects not included in the Landau theory, this transition is indeed first order. However, this Landau prediction turns out to be incorrect for the three-states Potts model in two dimensions. Such failures should not come as a surprise. After all, the Landau theory is a very

simple, phenomenological model for phase transitions. **Model 1** does not consider the spatial dependence of the order parameter. (Note that one can develop generalized Landau models which consider spatial dependence of the order parameter.) It also ignores thermal fluctuations at large length scales. The modern theory of phase transitions is the Renormalization Group Theory, to be discussed in Sec. 1.6.

It is easy to see that if the third-order term were accidentally missing ($\mathbf{B}=\mathbf{0}$), **Model 1** predicts that a second-order transition would occur when the coefficient of the second-order term becomes zero ($\mathbf{A}=\mathbf{0}$). Next we will introduce a model in which second-order transitions can occur as a result of symmetry and there can also exist a tricritical point, where a second-order transition turns into a first-order one.

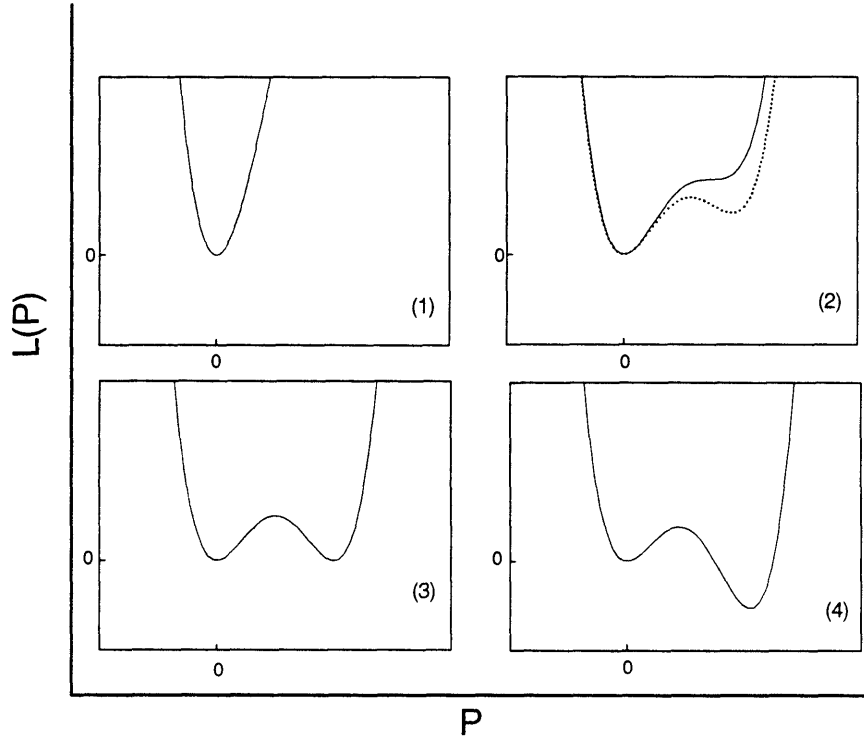


Fig. 1-2. Typical Landau Free Energy curves in **Model 1**. Drawn for $B < 0$; the behavior is the same for $B > 0$ but the second minimum lies at negative P values.

(1) $B^2 - 4AC < 0$: $L(P)$ is minimum at $P = 0$

(2) $B^2 - 4AC = 0$ (solid curve): metastability limit, $P_{\pm} = -B/2C$ for ordered phase where $L(P_{\pm}) > 0$ and $\partial^2 L / \partial P^2|_{P=P_{\pm}} = 0$; $B^2 - 4AC > 0$

(dotted curve): one more minimum at $0 < P_+ < \bar{P} = -2B/3C$ with $L(P_+) > 0$

(3) $B^2 - 4AC > 0$: first-order transition occurs when $L(\bar{P}) = 0$ at $\bar{P} = -2B/3C$

(4) $B^2 - 4AC > 0$: with $L(P_+) < 0$ and $P_+ > \bar{P}$.

B. Model 2

System That Is Symmetric Under Inversion of P

In this case, $L(-P)=L(P)$ and the odd order terms are excluded by symmetry. We keep terms up to sixth order:

$$L(P)=aP^2+bP^4+cP^6 \quad (1.8)$$

where $c>0$, $a>0$, $t=(T-T_0)/T_0$, and T_0 is a constant. Solving $\partial L/\partial P=0$, we get five roots at $P=0$, $P=\pm P_+$ and $P=\pm P_-$ where

$$P_{\pm}^2 = \frac{1}{3c}(-b \pm \sqrt{b^2 - 3act}) \quad (1.9)$$

1. We consider first the case when $b>0$; see Fig. 1-3.

Here P_- is not a real number since $P_-^2 = \frac{1}{3c}(-b - \sqrt{b^2 - 3act}) < 0$

- when $T>T_0$ ($t>0$)

P_+ is not a real number since $P_+^2 = \frac{1}{3c}(-b + \sqrt{b^2 - 3act}) < 0$. So there

is only one real root $P=0$ with $L(0)=0$ and $\left. \frac{\partial^2 L}{\partial P^2} \right|_{P=0} > 0$. The

system is in the symmetric phase.

- when $T=T_0$ ($t=0$)

$P_+ = 0$. It is easy to get $\left. \frac{\partial^2 L}{\partial P^2} \right|_{P=0} = \left. \frac{\partial^3 L}{\partial P^3} \right|_{P=0} = 0$, and $\left. \frac{\partial^4 L}{\partial P^4} \right|_{P=0} > 0$. So the

only minimum of $L(P)$ is at $P=0$.

- when $T<T_0$ ($t<0$)

P_+ is a real number. The second-order derivatives are:

$\left. \frac{\partial^2 L}{\partial \mathbf{P}^2} \right|_{\mathbf{P}=\mathbf{0}} < \mathbf{0}$ and $\left. \frac{\partial^2 L}{\partial \mathbf{P}^2} \right|_{\mathbf{P}=\mathbf{P}_+} > \mathbf{0}$, so we conclude that $L(\mathbf{P})$ has a

maximum at $\mathbf{P}=\mathbf{0}$ and two minima at $\mathbf{P}=\pm\mathbf{P}_+$. The system moves from the symmetrical phase with $\mathbf{P}=\mathbf{0}$ to the more ordered phase with $\mathbf{P}=\mathbf{P}_+$ or $\mathbf{P}=-\mathbf{P}_+$. The symmetry of the system is spontaneously broken. The onset of transition is at $\mathbf{T}=\mathbf{T}_0$, and the order parameter changes continuously since $\mathbf{P}_+(\mathbf{T}=\mathbf{T}_0)=\mathbf{0}$. This continuity leads to a continuous entropy because at the transition temperature \mathbf{T}_0 , we have

$$\Delta S = S(\mathbf{P}=\mathbf{0}) - S(\mathbf{P}=\mathbf{P}_+(\mathbf{T}_0)) = \left[\frac{\partial(\mathbf{a}\mathbf{t})}{\partial \mathbf{T}} \mathbf{P}_+^2 + \frac{\partial \mathbf{b}}{\partial \mathbf{T}} \mathbf{P}_+^4 + \frac{\partial \mathbf{c}}{\partial \mathbf{T}} \mathbf{P}_+^6 \right]_{\mathbf{T}=\mathbf{T}_0} = \mathbf{0},$$

showing that this free energy functional leads to a continuous transition in Landau theory when $\mathbf{b} > \mathbf{0}$. The derivatives of the entropy are singular, and will be discussed later.

2. Now we consider the case when $\mathbf{b} = \mathbf{0}$

Here \mathbf{P}_- is not a physical solution since $\mathbf{P}_-^2 = -\sqrt{-\frac{\mathbf{a}\mathbf{t}}{3\mathbf{c}}}$ cannot yield a real value for \mathbf{P}_- . For \mathbf{P}_+ we have $\mathbf{P}_+^2 = \sqrt{-\frac{\mathbf{a}\mathbf{t}}{3\mathbf{c}}}$.

- when $\mathbf{T} > \mathbf{T}_0$ ($\mathbf{t} > 0$)

\mathbf{P}_+ is not a real number. There is only one root $\mathbf{P}=\mathbf{0}$ with

$L(\mathbf{0}) = \mathbf{0}$, $\left. \frac{\partial^2 L}{\partial \mathbf{P}^2} \right|_{\mathbf{P}=\mathbf{0}} > \mathbf{0}$ which gives a minimum of $L(\mathbf{P})$. The system

is in the symmetric phase.

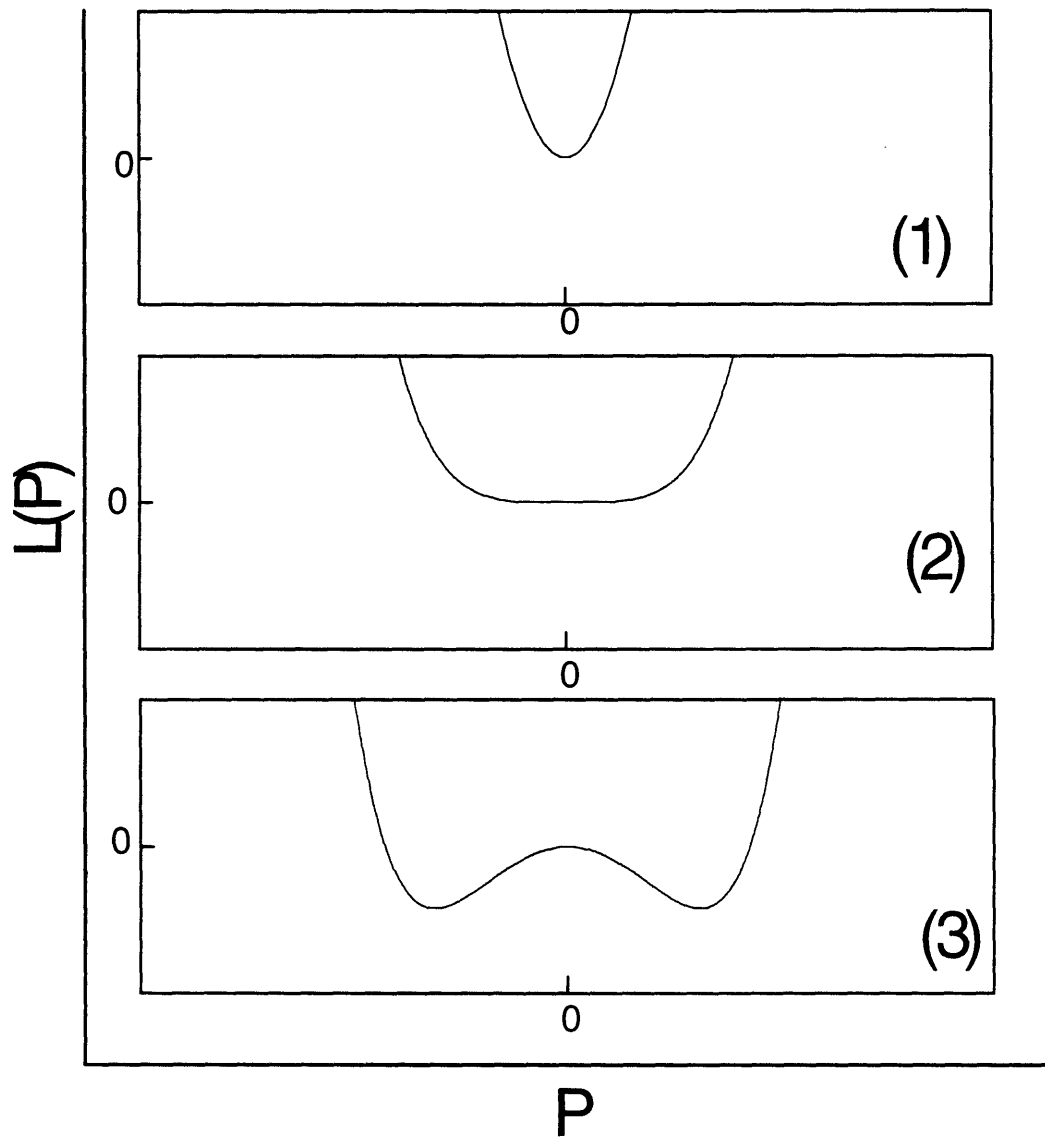


Fig. 1-3. Typical Landau Free Energy curves in Model 2 with $b > 0$. (1) $T > T_0$, $L(P)$ has minimum at $P = 0$ (2) $T = T_0$, onset of transition, $\partial^2 L / \partial P^2|_0 = 0$ (3) $T < T_0$, $L(P)$ has minima at $P = \pm P_+$ with $L(P_+) = L(-P_+) < 0$.

- when $T = T_0$ ($t=0$)

$P_+ = 0$. It is easy to get $\left. \frac{\partial^2 L}{\partial P^2} \right|_{P=0} = \left. \frac{\partial^3 L}{\partial P^3} \right|_{P=0} = 0$, and $\left. \frac{\partial^4 L}{\partial P^4} \right|_{P=0} > 0$. So the

only minimum of $L(P)$ is at $P = 0$.

- when $T < T_0$ ($t < 0$)

P_+ is a real number. From the second-order derivatives

$\left. \frac{\partial^2 L}{\partial P^2} \right|_{P=0} < 0$ and $\left. \frac{\partial^2 L}{\partial P^2} \right|_{P=P_+} > 0$ we conclude that $L(P)$ has a maximum

at $P = 0$ and two minima at $P = \pm P_+$. The system moves from the

symmetrical phase with $P = 0$ to the more ordered phase with

$P = P_+$ or $P = -P_+$. The symmetry of the system is spontaneously

broken. The onset of the transition is at $T = T_0$. The order

parameter changes continuously since $P_+(T = T_0) = 0$. This

continuity leads to a continuous entropy as explained when

previously in the case of $b > 0$. This transition point at $b = 0$ and

$T = T_0$ has a special name : the tricritical point. Setting $b = 0$ in

Eq. (1.9) we get for the order parameter in the ordered phase

$P \propto |t|^{\beta_{tc}}$, where $\beta_{tc} = 1/4$ is the tricritical order parameter

exponent. This β_{tc} can be compared to the usual mean -field

exponent $\beta_{MF} = 1/2$. The usual mean field model is **Model 2** with

vanishing sixth-order term ($c = 0$): $L(P) = aP^2 + bP^4$, where $b > 0$,

$a > 0$. The order parameter in the ordered phase is $P \propto |t|^{\beta_{MF}}$,

where $\beta_{MF} = 1/2$, as follows from $\partial L / \partial P = 2aP + 4bP^3 = 0$.

3. Finally we consider the case when $b < 0$; see Fig. 1-4.

Now recall from Eq. (1.9) that we have $\mathbf{P}_{\pm}^2 = \frac{1}{3c}(-b \pm \sqrt{b^2 - 3act})$.

- when $b^2 - 3act < 0$ or $T > T_k = T_0 \left(1 + \frac{b^2}{3ac}\right)$

\mathbf{P}_{\pm} are not real numbers. The only minimum of $L(\mathbf{P})$ is at $\mathbf{P} = \mathbf{0}$

with $\left. \frac{\partial^2 L}{\partial \mathbf{P}^2} \right|_{\mathbf{P}=\mathbf{0}} > \mathbf{0}$. The system is in the symmetric phase.

- when $T = T_k$, which occurs when $b^2 = 3act$ we find $\mathbf{P}_{\pm}^2 = -\frac{b}{3c}$ and

$\left. \frac{\partial^2 L}{\partial \mathbf{P}^2} \right|_{\mathbf{P}=\mathbf{P}_{\pm}} = \mathbf{0}$. \mathbf{P}_{\pm} are points of inflection with $L(\mathbf{P}_{\pm}) > \mathbf{0}$. The system

is still in the symmetric phase, and T_k is the metastability limit of the ordered phase on heating.

- when $T < T_k$ or $b^2 - 3act > 0$

\mathbf{P}_{\pm} are real numbers. The second derivatives are $\left. \frac{\partial^2 L}{\partial \mathbf{P}^2} \right|_{\mathbf{P}=\pm\mathbf{P}_{\pm}} > \mathbf{0}$ and

$\left. \frac{\partial^2 L}{\partial \mathbf{P}^2} \right|_{\mathbf{P}=\pm\mathbf{P}_{\pm}} < \mathbf{0}$, indicating that two minima occur at $\mathbf{P} = \pm\mathbf{P}_{\pm}$ and two

maxima at $\mathbf{P} = \pm\mathbf{P}_{\pm}$. It is possible that the extra minima at

$\mathbf{P} = \pm\mathbf{P}_{\pm}$ will be lower than the one at $\mathbf{P} = \mathbf{0}$ and become the global

minima. The onset of transition happens when $L(\pm\mathbf{P}_{\pm}) = L(\mathbf{0}) = \mathbf{0}$,

and we also know $\left. \frac{\partial L}{\partial \mathbf{P}} \right|_{\mathbf{P}=\pm\mathbf{P}_{\pm}} = \mathbf{0}$. From these two equations we get

$\mathbf{P}_{\pm}^2 = \bar{\mathbf{P}}^2 = -b/2c$ and the transition temperature is $T_1 = T_0 \left(1 + \frac{b^2}{4ac}\right)$.

This means that $\pm\bar{\mathbf{P}} \neq \mathbf{0}$ at the transition. The system moves from the symmetrical phase with $\mathbf{P} = \mathbf{0}$ to the more ordered phase

with $\mathbf{P} = \bar{\mathbf{P}}$ or $\mathbf{P} = -\bar{\mathbf{P}}$. The order parameter changes discontinuously and so does the entropy $\Delta\mathbf{S}$ and enthalpy $\Delta\mathbf{H}$. If we assume that the coefficients b and c do not depend on temperature T , then

$$\Delta\mathbf{S} = \mathbf{S}(\mathbf{P} = \mathbf{0}) - \mathbf{S}(\mathbf{P} = \mathbf{P}_+(T_1)) = \left[\frac{\partial(\mathbf{a}t)}{\partial T} \bar{\mathbf{P}}^2 + \frac{\partial b}{\partial T} \bar{\mathbf{P}}^4 + \frac{\partial c}{\partial T} \bar{\mathbf{P}}^6 \right]_{T=T_1} = -\frac{\mathbf{a}b}{2cT_0} > \mathbf{0}$$

$$\text{and } \Delta\mathbf{H} = T_1 \Delta\mathbf{S} = -\frac{\mathbf{a}b}{2cT_0} T_1 = -\frac{\mathbf{a}b}{2c} \left(1 + \frac{b^2}{4ac} \right) > \mathbf{0}.$$

These discontinuities correspond to a first-order transition in Landau theory with latent heat $\mathbf{L} = \Delta\mathbf{H}$.

We conclude that **Model 2** describes first-order transitions when $b < 0$ and second-order transitions when $b > 0$. The transition at $b = 0$ is a special tricritical point, where a first-order transition turns into a second-order one. In the case of liquid crystals, the SmA-SmC transition is an example of **Model 2** Landau behavior [see Chapter 3].

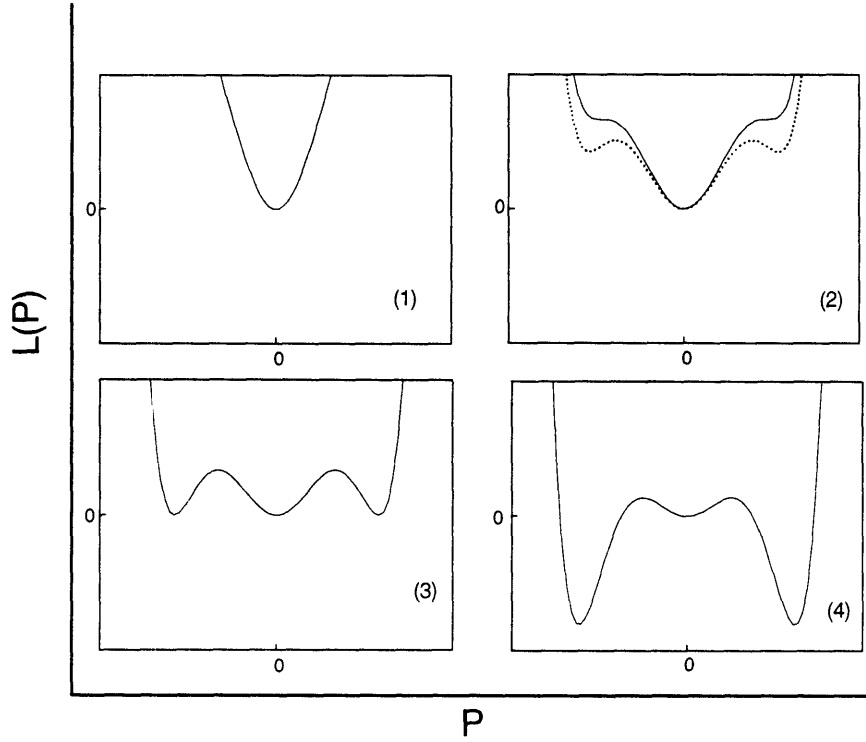


Fig. 1-4. Typical Landau Free Energy curves in Model 2 with $b < 0$. (1) $T > T_k$, $L(P)$ has one minimum at $P = 0$ (2) $T_1 < T \leq T_k$, $L(P)$ has global minimum at $P = 0$; solid curve $T = T_k$ and dotted curve for $T_1 < T < T_k$. (3) $T = T_1$, first-order transition, where $P_+^2 = \bar{P}^2 = -b/2c$ (4) $T < T_1$, $L(P)$ has minima at $P = \pm P_+$ with $P_+^2 > \bar{P}^2$ and $L(P_+) = L(-P_+) < 0$.

C. Some Predictions Of Landau Theory

Landau theory provides simple mechanisms for phase transitions. However, its predictions are quantitatively reliable only for special cases like the SmA-SmC transition in liquid crystals and ferroelectric transitions in KH_2PO_4 type crystals. We will analyze the Landau heat capacity C_p for **Model 2**, where

$$C_p = T \left(\frac{\partial S}{\partial T} \right)_p = -T \left(\frac{\partial^2 G}{\partial T^2} \right)_p \quad (1.10)$$

Consider the case of a second-order or tricritical transition (i.e., $b \geq 0$). The order parameter is

$$P = 0 \quad \text{for } T > T_0 \quad (1.11a)$$

$$P^2 = \frac{1}{3c} \left(\sqrt{b^2 - 3ac \frac{(T - T_0)}{T_0}} - b \right) \quad \text{for } T < T_0 \quad (1.11b)$$

We ignore the possible temperature dependencies of b and c ; thus

$$C = C_p^0 \quad (T > T_0) \quad (1.12a)$$

$$C_p = C_p^0 + \frac{Ta^2}{2T_0^2} \frac{1}{\sqrt{b^2 - 3ac \frac{T - T_0}{T_0}}} \quad (T \leq T_0) \quad (1.12b)$$

where $C_p^0 = -T(\partial^2 G_0 / \partial T^2)_p$ is a smooth function of T . In this case, Landau theory predicts a finite discontinuity in the heat capacity at the transition: $\Delta C_p = C_p - C_p^0 = a^2 / 2bT_0$. When $b = 0$ (the tricritical transition), there is a divergent form for the excess heat capacity $\Delta C_p = C_p - C_p^0$: $\Delta C_p(T) \propto (T_0 - T)^{-0.5}$ below T_0 . In

reality, experiments show that the heat capacity usually diverges like a power law $\Delta C_p \propto |T - T_c|^{-\alpha} + B_c$ both below and above the second-order transition temperature T_c . The exponent α can vary in different materials from a negative value (in which case $\Delta C_p \rightarrow B_c$ at T_c) to positive values as large as 1. There are many other thermodynamic properties that show power law singularities at second-order transitions that cannot be explained quantitatively by the Landau model.

1.6 Renormalization Group Theory

For Phase Transitions

The successful theory for phase transitions involving critical fluctuations is the renormalization group (RG) theory. Instead of dealing with a Landau free energy, one starts with the Ginzburg-Landau-Wilson Hamiltonian, constructed from a coarse-grained order parameter and the symmetry properties of the system. An example of a Ginzburg-Landau-Wilson Hamiltonian is

$$\beta H = \int d^D x \left\{ \frac{K}{2} (\nabla \mathbf{m})^2 + \frac{t}{2} \mathbf{m}^2 + u \mathbf{m}^4 + v \mathbf{m}^6 \right\}, \quad (1.13)$$

where $\beta = 1/k_B T$ and the coupling constants K , t , u and v are functions of the microscopic parameters and the temperature T . The quantity \mathbf{m} is the coarse-grained order parameter, which means atomic-scale fluctuations have been averaged out over certain length scales. This order parameter depends on spatial

position x in dimension D , that is: $\mathbf{m} = \mathbf{m}(x)$. Following the standard procedures of statistical mechanics, one can analyze the partition function Z given by

$$Z = \int d\mathbf{m}(x) \exp(-\beta H). \quad (1.14)$$

This is a functional integral. The relation between free energy F and partition function Z is

$$\beta F = -\ln Z. \quad (1.15)$$

It turns out that a “saddle point approximation” to this Ginzburg-Landau-Wilson model corresponds to the phenomenological Landau theory. In this approximation, one takes the maximum integrand of the functional integral as a crude estimate for the integral, so

$$\beta F \approx \text{Min}(\beta H) = \text{Min} \left\{ \frac{t}{2} \mathbf{m}^2 + u \mathbf{m}^4 + v \mathbf{m}^6 \right\} \Omega \quad (1.16)$$

where Ω is the system volume, and Min stands for minimum. The problem reduces to the minimization of a function of an order parameter \mathbf{m} that is uniform in space ($\nabla \mathbf{m} = \mathbf{0}$), i.e., no spatial fluctuations are allowed. This is exactly the Landau (mean-field) theory.

In most cases, the partition function is very hard to calculate. Instead of a direct calculation of Z , one could analyze the Ginzburg-Landau-Wilson Hamiltonian and get useful scaling laws for thermodynamic properties and the corresponding critical exponents. In 1966, L.P. Kadanoff observed that in the vicinity of a critical point, there are fluctuations at all length

scales and the system is self-similar (scale invariant) at the transition.⁴ He proposed that at a particular length scale a , the system can be characterized by a Hamiltonian $(\beta H)_a$, with coupling constants that depend on the length scale a :

$$(\beta H)_a = \int d^D \mathbf{x} \left\{ \frac{\mathbf{K}_a}{2} (\nabla \mathbf{m})^2 + \frac{t_a}{2} \mathbf{m}^2 + u_a \mathbf{m}^4 + v_a \mathbf{m}^6 \right\} \quad (1.17)$$

Later, K.G. Wilson⁵ invented systematic procedures to calculate these coupling constants by RG transformations in three steps:

(i) coarse grain the order parameter over a certain length ba

(ii) rescale the space by the same factor b : $\mathbf{x}' = \frac{\mathbf{x}}{b}$

(iii) renormalize the order parameter $\mathbf{m}' = \frac{\mathbf{m}}{\zeta}$

Mathematically, RG transformation is a nonlinear transformation \mathbf{R}_b for the coupling constants $\kappa = (\mathbf{K}, \mathbf{t}, \mathbf{u}, \mathbf{v})$. It is possible to calculate (at least approximately) the recursion relation $\kappa' = \mathbf{R}_b \kappa$. We will see that these transformations \mathbf{R}_b form a semi-group. Consider two successive transformations, with $b=b_1$ and $b=b_2$. These two successive transformations are equivalent to a combined scale change $b_1 b_2$. That is, $\kappa'' = \mathbf{R}_{b_1 b_2} \kappa = \mathbf{R}_{b_1} (\mathbf{R}_{b_2} \kappa) = \mathbf{R}_{b_1} \mathbf{R}_{b_2} \kappa$.

$$\text{Thus } \mathbf{R}_{b_1 b_2} = \mathbf{R}_{b_1} \mathbf{R}_{b_2}. \quad (1.18)$$

The correlation length describes the spatial extent of fluctuations in a physical quantity about the average of that

quantity. For example, the correlation function for the order parameter \mathbf{m} behaves like

$$\langle (\mathbf{m}(\mathbf{r}) - \langle \mathbf{m} \rangle)(\mathbf{m}(\mathbf{0}) - \langle \mathbf{m} \rangle) \rangle \propto \frac{1}{r^{d-2+\eta}} \exp(-r/\xi) \text{ at large scales of } \mathbf{r},$$

where the symbol $\langle \rangle$ denotes thermal average, d is the dimension of space, η is a small positive number, and ξ is called the correlation length. It is found that the correlation length ξ diverges at a second-order transition. Under RG transformation \mathbf{R}_b , the correlation length transforms as $\xi(\kappa') = \frac{\xi(\kappa)}{b}$. If the RG transformation \mathbf{R}_b has a fixed point κ^* , so that $\mathbf{R}_b \kappa^* = \kappa^*$, then at this fixed point $\xi(\kappa^*) = \frac{\xi(\kappa^*)}{b}$. This implies that $\xi(\kappa^*)$ can only be zero or infinity. This important observation leads to the identification of the critical transition points: they are the fixed points of the RG transformation \mathbf{R}_b with $\xi = \infty$.

Close to the fixed point of \mathbf{R}_b , we can linearize the transformation. Let the system be close to κ^* :

$$\kappa = \kappa^* + \delta\kappa \tag{1.19}$$

After RG transformation the system is described by

$$\kappa' = \mathbf{R}_b \kappa = \mathbf{R}_b \kappa^* + \mathbf{R}_b \delta\kappa = \kappa^* + \mathbf{R}_b \delta\kappa \tag{1.20}$$

κ' should also close to κ^* , so we have

$$\kappa' \approx \kappa^* + \delta\kappa' = \kappa^* + \mathbf{M}^{(b)} \delta\kappa. \tag{1.21}$$

Where the matrix $\mathbf{M}_{nm}^{(b)} = \left. \frac{\partial \kappa'_n}{\partial \kappa_m} \right|_{\kappa=\kappa^*}$ is the linearized \mathbf{R}_b at the fixed

point κ^* . If matrix $\mathbf{M}^{(b)}$ has an eigenvector $e^{(\sigma)}$ with eigenvalue

$\lambda^{(\sigma)}$, then by the semi-group property Eq. (1.18), we have

$$\mathbf{M}^{(b_1)}\mathbf{M}^{(b_2)} = \mathbf{M}^{(b_1 b_2)} \quad (1.22)$$

$$\lambda_{b_1}^{(\sigma)}\lambda_{b_2}^{(\sigma)} = \lambda_{b_1 b_2}^{(\sigma)} \quad (1.23)$$

The solution is

$$\lambda_b^{(\sigma)} = \mathbf{b}^{y_\sigma} \quad (1.24)$$

with exponent y_σ independent of \mathbf{b} .

Now we can see how the system coupling constants change under RG close to the fixed point. Expanding $\delta\kappa$ with eigenvectors

$$\delta\kappa = \sum_{\sigma} c_{\sigma} \mathbf{e}^{(\sigma)} \quad (1.25)$$

$$\text{Then } \delta\kappa' = \mathbf{M}^{(b)}\delta\kappa = \sum_{\sigma} c_{\sigma} \mathbf{M}^{(b)} \mathbf{e}^{(\sigma)} = \sum_{\sigma} c_{\sigma} \lambda_b^{(\sigma)} \mathbf{e}^{(\sigma)} = \sum_{\sigma} c_{\sigma} \mathbf{b}^{y_{\sigma}} \mathbf{e}^{(\sigma)} \quad (1.26)$$

There are three kinds of eigenvector $\mathbf{e}^{(\sigma)}$ under RG:

(1) *relevant*: $y_{\sigma} > 0$, the component grows as

renormalization occurs.

(2) *irrelevant*: $y_{\sigma} < 0$, the component decreases as

renormalization occurs.

(3) *marginal*: $y_{\sigma} = 0$, the component does not change as

renormalization occurs.

Let us consider the case of two relevant coupling constants, say temperature T and magnetic field h , with the transition point at $T=T_c$ and $h=0$. Let $\mathbf{t}=(T-T_c)/T_c$. Under RG transformation, the free energy density is

$$\mathbf{f}(\mathbf{t}, \mathbf{h}) = \frac{\mathbf{f}(\mathbf{t}', \mathbf{h}')}{\mathbf{b}^d} \quad (1.27)$$

The linearized RG usually takes the form:

$$\begin{pmatrix} \mathbf{t}' \\ \mathbf{h}' \end{pmatrix} = \begin{pmatrix} \mathbf{b}^{y_t} & \mathbf{0} \\ \mathbf{0} & \mathbf{b}^{y_h} \end{pmatrix} \begin{pmatrix} \mathbf{t} \\ \mathbf{h} \end{pmatrix} \quad (1.28)$$

so the eigenvector is $\begin{pmatrix} \mathbf{t} \\ \mathbf{h} \end{pmatrix}$. Then the free energy density is

$$\mathbf{f}(\mathbf{t}, \mathbf{h}) = \frac{\mathbf{f}(\mathbf{t}', \mathbf{h}')}{\mathbf{b}^d} = \frac{\mathbf{f}(\mathbf{b}^{y_t} \mathbf{t}, \mathbf{b}^{y_h} \mathbf{h})}{\mathbf{b}^d} \propto |\mathbf{t}|^{2-\alpha} \mathbf{f}(\mathbf{h} |\mathbf{t}|^{-\Delta}) \quad (1.29)$$

where

$$2-\alpha = \frac{\mathbf{d}}{y_t} \quad \Delta = \frac{y_h}{y_t} \quad (1.30)$$

So we get for the heat capacity

$$\mathbf{C} \propto -\frac{\partial^2 \mathbf{f}}{\partial \mathbf{t}^2} \propto |\mathbf{t}|^{-\alpha} \quad (1.31)$$

As for the correlation length ξ when $h=0$, we have

$$\xi(\mathbf{t}) = \mathbf{b} \xi(\mathbf{t}') = \mathbf{b} \xi(\mathbf{b}^{y_t} \mathbf{t}) \propto |\mathbf{t}|^{-\nu} \quad \nu = \frac{1}{y_t} \quad (1.32)$$

K.G. Wilson's RG procedure provides practical methods to calculate the exponents y_t and y_h , at least approximately. The resulting theoretical values of critical exponents agree very well with experimental values. There are many other implementations of RG theory that have been very successful. Among these are the real space RG and Monte Carlo RG theories.⁶⁻⁸

Reference

1. Kerson Huang, "Quarks, leptons & gauge fields", 2nd ed., World Scientific, Singapore, River Edge, NJ (1992).
2. P.G. de Gennes and J. Prost, "The physics of liquid crystals", 2nd ed., Oxford University Press, New York (1993).
3. D. Landau and E. M. Lifshitz, "Statistical physics", 3d rev. ed. by E. M. Lifshitz and L. P. Pitaevskii, Pergamon Press, New York (1980).
4. L.P. Kadanoff, *Physics* **2**, 263 (1966).
5. K.G. Wilson, *Phys. Rev.* **B4**, 3174, 3184 (1971).
6. C. Domb and M.S. Green, "Phase transitions and critical phenomena", Vol. 1-15, Academic Press, New York (1972-).
7. Shang-keng Ma, "Modern theory of critical phenomena", W. A. Benjamin, Advanced Book Program, Reading, Mass. (1976).
8. Giorgio Parisi, "Statistical field theory", Addison-Wesley, Redwood City, Calif. (1988).

Chapter 2

High-Resolution Calorimetry

2.1 A Simple Model For Thermal Analysis

The simplest model for thermal analysis is the so-called zero-dimensional model shown schematically in Fig. 2-1. It assumes that the internal relaxation time of the system of interest (sample + cell) is very small compared to the time scale of experimental data acquisition and that the heat leak to the thermal bath can be represented by a single parameter, the thermal resistance R between the system and the bath. An external nonmechanical power P is put into the system which is at temperature T , and this system can exchange heat with a bath at temperature T_b .

The basis for thermal analysis is the first law of thermodynamics: $\Delta U = Q + W$, which means

**change in system energy U = heat flow into system Q +
work done on system W .**

In differential form this becomes $dU = dQ + dW$. The system enthalpy H is given by $H \equiv U + pV$, with p and V being the system pressure and volume. Thus one has

$$dH = dU + pdV + Vdp = dQ + Vdp + dW_e, \quad (2.1)$$

where dW_e is the differential nonmechanical (electrical in the case of the calorimeters to be described here) work done on the system.

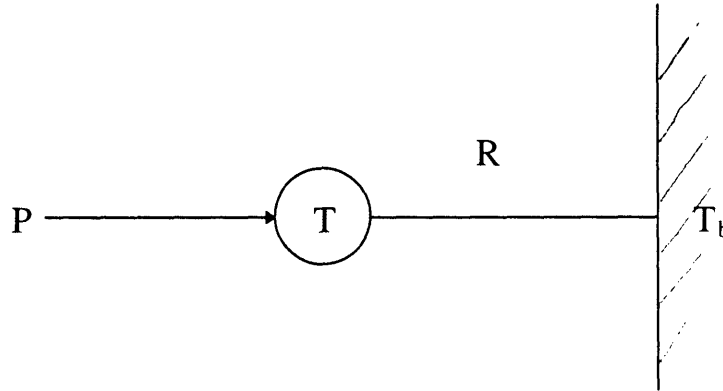


Fig. 2-1. Schematic diagram for zero-dimensional model of thermal analysis.

The heat flow between the system and the bath is given by Newton's law:

$$-\frac{dQ}{dt} = \frac{T - T_b}{R} \quad (2.2)$$

where R depends on geometric factors and the thermal conductivity of the link between the system and the bath.

For a process at constant pressure, one has

$$dW_e = dH - dQ \quad (2.3)$$

When the system does not lie within the two-phase coexistence region at a first-order transition, we have $dH = (\partial H / \partial T)_p dT = C_p^{sys} dT$,

where $C_p^{sys} = C_p + C_p(\text{cell})$ is the system(sample + cell) heat capacity. However, if the system is inside a two-phase coexistence region, then $dH = (\partial H/\partial T)_p dT + dL = C_p^{sys} dT + dL$, where L is the latent heat associated with the first-order phase transition. Considering the time dependence, we have for the input power

$$P = \frac{dW_e}{dt} = \frac{dH}{dt} - \frac{dQ}{dt} \quad (2.4)$$

and the enthalpy is

$$H(t) = \int \left(P - \frac{T - T_b}{R} \right) dt = H(0) + \int_0^t \left(P - \frac{T - T_b}{R} \right) dt \quad (2.5)$$

where $H(0)$ is an arbitrary constant representing the enthalpy at a temperature T_0 corresponding to $t=0$.

Eq. (2.4) can be written in the following way:

$$P = C_p^{sys} \frac{dT}{dt} + \frac{T - T_b}{R} + \frac{dL}{dt} \quad (2.6)$$

The purpose of thermal analysis is to measure the enthalpy H , the latent heat L , and the heat capacity C_p^{sys} . Equation (2.5) can be used to get the enthalpy $H(t)$ as a function of time t by numerical integration. This requires one to measure as functions of time t the power P , thermal resistance R , sample temperature T , and bath temperature T_b . This $H(t)$ can be converted to a function of temperature $H(T)$ since one can monitor the sample temperature $T(t)$. From Eqs. (2.5) and (2.6) we get the derivative of the enthalpy dH/dT in the following forms:

$$\frac{dH}{dT} = C_p^{\text{sys}} \quad (\text{outside a two-phase coexistence region})$$

$$\frac{dH}{dT} = C_p^{\text{sys}} + \frac{dL}{dT} \quad (\text{inside a two-phase coexistence region})$$

A. Process Without Latent Heat

Outside a two-phase coexistence region, the heat capacity C_p^{sys} can be obtained directly from Eq. (2.6) with $L=0$:

$$C_p^{\text{sys}} = \left(P - \frac{T - T_b}{R} \right) / (dT/dt) \quad (2.7)$$

For a second-order transition there is no latent heat, so Eq. (2.7) can be used to get the C_p^{sys} . This approach requires one to perform numerical differentiation dT/dt . We will explain in this chapter that the best implementations of this method are adiabatic scanning calorimetry [see Sec. 2.2] and non-adiabatic scanning calorimetry (linear-power mode in relaxation calorimetry) [see Sec. 2.4], where the system temperature $T(t)$ varies almost linearly with time t .

Another efficient method is ac calorimetry which does not make use of Eq. (2.7), and avoids measuring the thermal resistance R [see Sec. 2.3]. Note that an ac calorimeter cannot measure latent heats, but can provide useful qualitative information about two-phase coexistence.

B. Process With Latent Heat

Inside a two-phase coexistence region C_p^{sys} values cannot be obtained by using Eq. (2.7), but one can choose to get the enthalpy from Eq. (2.5). Note that inside a two-phase coexistence region we have $C_p^{\text{sys}} = C_p(\text{cell}) + C_p(\text{coex})$, where $C_p(\text{coex})$ is the heat capacity of the two coexisting phases that would be observed in the absence of phase conversion, i.e., $C_p(\text{coex}) = X_\alpha C_p(\alpha) + X_\beta C_p(\beta)$ (X_i is the mass fraction of phase i). In general, $C_p(\text{coex})$ cannot be measured experimentally except in the rare case when the phase conversion rate is very slow (sluggish). [see Sec. 2.3B]. The principal interest in the thermodynamics of a first-order transition is not $C_p(\text{coex})$ but the latent heat L , which can be obtained from integrating Eq.(2.6):

$$L = \int_{t_1}^{t_2} \left(P - \frac{T - T_b}{R} \right) dt - \int_{T_1}^{T_2} C_p^{\text{sys}} dT, \quad (2.8)$$

where the two-phase coexistence is between temperatures (times) T_1 (t_1) and T_2 (t_2). In order to calculate the latent heat L , one needs to choose $C_p(\text{coex})$ values (see discussions below) and determine the coexistence region, i.e., values of T_1 (t_1) and T_2 (t_2). In thermal analysis it is well known that the enthalpy H is a smoother function of temperature than its derivative dH/dT . That is, it is easier to spot an anomaly in dH/dT , which exhibits a peak for most phase transitions, than in $H(T)$, which usually only has a change in curvature or a kink. Here we introduce the idea of an

effective heat capacity C_{eff} which is the derivative of the enthalpy to help identifying two-phase coexistence:

$$C_{\text{eff}} \equiv \frac{dH}{dT} = \frac{\left(P - \frac{T - T_b}{R} \right)}{dT/dt} \quad (2.9)$$

Comparing this to Eq. (2.7), we see that this C_{eff} is the same as the system heat capacity C_p^{sys} when the system is outside any two-phase coexistence region. When the system is inside a two-phase coexistence region, $C_{\text{eff}} = C_p^{\text{sys}} + dL/dT$. Note that $dL = \bar{L}dm$ where \bar{L} is the latent heat per unit mass of low-enthalpy phase converted into high-enthalpy phase. dL is non-zero for the conversion of one phase into another at a first-order transition and zero otherwise. The quantity $C_{\text{eff}} = C_p^{\text{sys}} + dL/dT > C_p^{\text{sys}}$ in a two-phase region usually stands out as being larger than a smooth extension of the pre-transitional C_p wings (see Fig. 2-2). More importantly, C_{eff} exhibits hysteresis for a first-order transition, which makes it useful in identifying very weak first-order transitions. One can use Eq. (2.9) to calculate C_{eff} by measuring P , T , R , T_b , and perform numerical differentiation dT/dt . With this effective heat capacity C_{eff} , Eq. (2.8) for the latent heat can be rewritten as

$$L = \int_{T_1}^{T_2} \left[C_{\text{eff}} - (C_p(\text{cell}) + C_p(\text{coex})) \right] dT \quad (2.10)$$

where $C_p(\text{coex})$ is the heat capacity of the two phases $\alpha + \beta$ that coexist over the temperature range from T_1 to T_2 . Recall that $C_p(\text{coex}) = X_\alpha C_p(\alpha) + X_\beta C_p(\beta)$. Since the two-phase coexistence region

$C_p(\text{coex}) = X_\alpha C_p(\alpha) + X_\beta C_p(\beta)$. Since the two-phase coexistence region is usually small (~ 100 mK), a common practice is to take $C_p(\alpha)$ and $C_p(\beta)$ to be independent of T over the range T_1 to T_2 : $C_p(\alpha) = C_p(T_1)$ for the one-phase α system and $C_p(\beta) = C_p(T_2)$ for the system in the β phase. There are two simple approximations for the temperature dependence of X_α and X_β : (1) $X_\alpha = 1$ from T_1 to $\bar{T} = (T_1 + T_2)/2$ and $X_\alpha = 0$ from \bar{T} to T_2 . (2) X_α decreases linearly with T from 1 at T_1 to 0 at T_2 . In either case, the latent heat L corresponds to the shaded area in Fig 2-2 (b3 or b4).

One has two alternative equations for calculating latent heat L : Eq. (2.8) involves only numerical integration, but one needs to identify precisely the two-phase coexistence region, which is best served by examining C_{eff} ; Eq. (2.10) involves not only numerical integration but also numerical differentiation dT/dt [see Eq. (2.9)] in order to get C_{eff} .

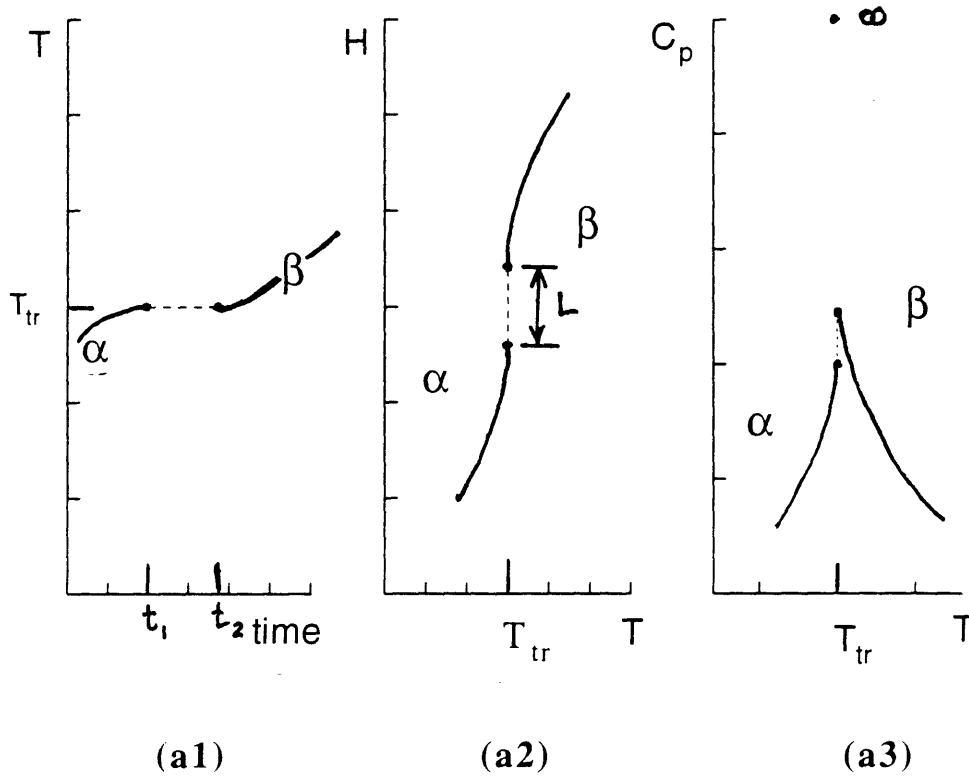
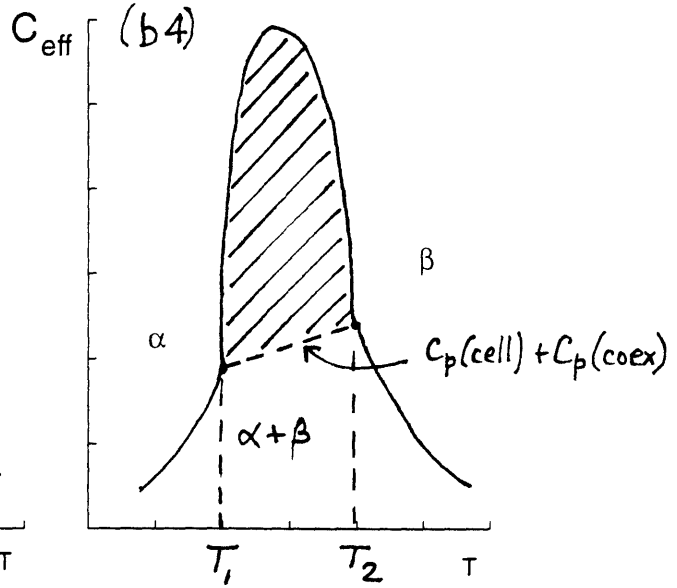
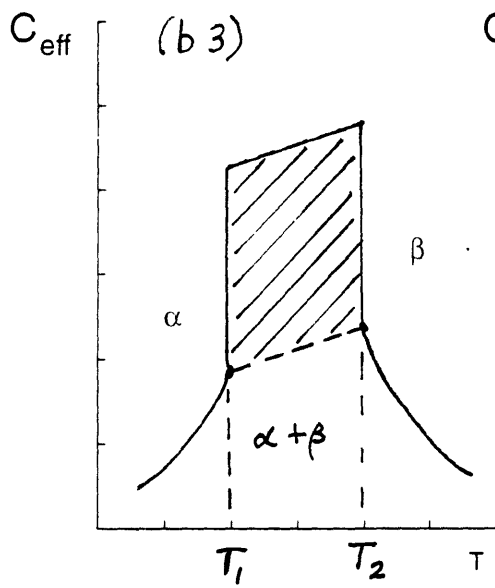
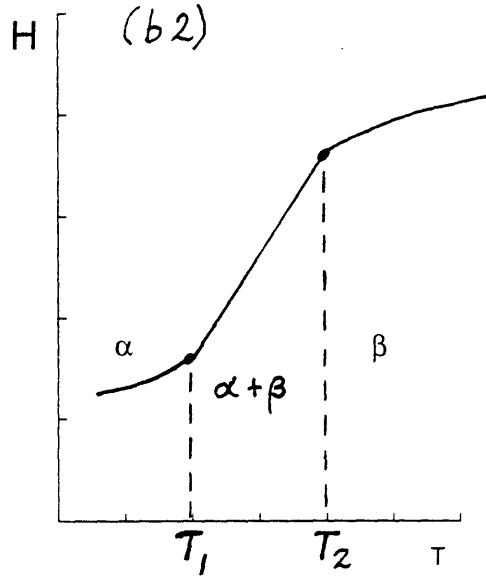
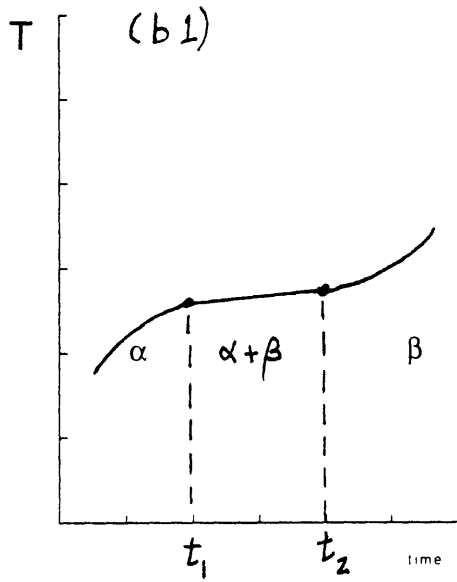


Fig. 2-2. Time dependence of the sample temperature T and the dependence of enthalpy H and heat capacity C_p on temperature. Drawn schematically for a sample near a weakly first-order transition. This type of transition has a small latent heat L and pretransitional C_p wings both above and below the transition temperature T_{tr} . (a) Ideal behavior: phase α and phase β coexist only at T_{tr} and the heating curve $T(t)$ exhibits a true hold;



(b) Real behavior: the sample exhibits a finite coexistence range between T_1 and T_2

(typically 100 mK wide). In this case, for a constant power input there is usually a linear ramp in T between t_1 and t_2 and a corresponding linear ramp in H between T_1 and T_2 . The latent heat L is given by

$$L = H(T_2) - H(T_1) - \int_{T_1}^{T_2} C_p^{\text{sys}} dT$$

the shaded area in (b3) and (b4). The sketch in (b3) corresponds to the limiting case $dm/dT = \text{constant}$ and quasi-static measurements; the sketch in (b4) is for more realistic conditions observed in slow nonadiabatic (relaxation) scanning runs.

2.2 Theory of Adiabatic Calorimetry

at Constant Pressure

If one can keep the heat leak very small: $\frac{T-T_b}{R} \rightarrow 0$, then the calorimeter is called an adiabatic calorimeter (there is no heat loss to the bath).

First consider the situation without latent heat effects (which means the system is outside any first-order coexistence region). The heat capacity is then given by Eq. (2.7) with $\frac{T-T_b}{R} \rightarrow 0$:

$$C_p^{\text{sys}} = \frac{P}{dT/dt} = \frac{dW_e}{dT} \quad (2.11a)$$

In the traditional step heating method, one puts in a finite electrical “heat” pulse W_e and observes a temperature rise ΔT . The value of C_p^{sys} is then taken to be $C_p = W_e/\Delta T$. However, much greater resolution can be achieved in the adiabatic scanning mode where P is held constant ($P=P_0=\text{constant}$) and one monitors the sample temperature T as a function of time. Then numerical differentiation of T with respect to t gives the value of C_p^{sys} as

$$C_p^{\text{sys}} = P_0/\dot{T} \quad (2.11b)$$

where $\dot{T} \equiv dT/dt$. In this mode, the system temperature is scanning almost linearly: $T(t) = T(0) + (P_0/C_p^{\text{sys}})t$ would hold if C_p^{sys} were a constant. Thus one measurement can cover a wide temperature

range in a long run carried out at a low enough rate \dot{T} to assure thermodynamic equilibrium. Typical scan rates are $\dot{T} \approx 100\text{--}200$ mK/h away from transitions and $\dot{T} \approx 10\text{--}20$ mK/h near transitions. The key to good performance is careful maintenance of adiabatic conditions and frequent high-quality temperature measurements. This method was developed and used extensively for studying liquid crystals by Thoen.¹

Now consider the situation with latent heat effects (the system temperature lies inside a two-phase coexistence region). In an ideal first-order transition, two phases will coexist at a constant transition temperature while one phase is converting into the other. In real experiments, one can use very slow scanning rates to avoid superheating or supercooling, and the sample temperature stays almost constant during the phase conversion. So with an adiabatic scanning calorimeter, one identifies a first-order transition by observing a “plateau” in the sample temperature $T = T(t)$ between time t_1 and t_2 where the corresponding temperatures T_1 and T_2 are very close to each other; see

Fig. 2-2(b-1). From Eqs. (2.8) we have

$$L = \int_{t_1}^{t_2} P_0 dt - \int_{T_1}^{T_2} C_p^{\text{sys}} dT = H(T_2) - H(T_1) - \int_{T_1}^{T_2} C_p^{\text{sys}} dT \quad (2.12)$$

where $C_p^{\text{sys}} = C_p(\text{cell}) + C_p(\text{coex})$. Refer to Sec. 2.1B for discussions about how to choose the $C_p(\text{coex})$ values.

Strictly speaking, an adiabatic calorimeter is designed not to lose any heat, so it usually operates in heating mode. Sometimes

people use the machine in cooling mode by monitoring the heat leak quantitatively. In this thesis, we will call it nonadiabatic calorimetry since the heat leak is finite. One can make both heating and cooling runs in nonadiabatic calorimetry and compare the data in order to find thermal hysteresis. This procedure will provide important information about first-order phase transitions. Next we will discuss two types of nonadiabatic calorimetry: ac calorimetry and relaxation calorimetry.

2.3 Theory of AC Calorimetry

at Constant Pressure

A. Process Without Latent Heat

When the thermal resistance R is not negligible but $L=0$, Eq. (2.6) gives

$$C_p^{\text{sys}} \frac{dT}{dt} + \frac{T - T_b}{R} = P \quad (2.13)$$

If we take C_p^{sys} and R as constants over a small time (temperature) interval, then Eq. (2.13) is integrable. For ac calorimetry, one uses a sinusoidal input power $P = P_0 \cos(\omega t) + P_0$. If one keeps the bath temperature T_b constant during a measurement and the sample is initially in equilibrium with the bath ($T=T_b$), then after switching on the sinusoidal power at $t=0$, the system temperature is

$$\mathbf{T}(t) = \mathbf{T}_b + \mathbf{P}_0 \mathbf{R} \left(1 + \frac{\cos(\omega t) + \omega \tau_{\text{ext}} \sin(\omega t)}{1 + (\omega \tau_{\text{ext}})^2} - \left[1 + \frac{1}{1 + (\omega \tau_{\text{ext}})^2} \right] \exp(-t/\tau_{\text{ext}}) \right) \quad (2.14)$$

where $\tau_{\text{ext}} = \mathbf{R} \mathbf{C}_p^{\text{sys}}$ is the “external” time constant for heat flow from the system to the bath. Thus, in the steady state (after a time long enough so the exponential term is negligible) the system temperature has an ac component and a dc component:

$\mathbf{T}(t) = \mathbf{T}_{\text{dc}} + \mathbf{T}_{\text{ac}}(t)$, where

$$\mathbf{T}_{\text{dc}} = \mathbf{T}_b + \mathbf{P}_0 \mathbf{R} \quad (2.15)$$

and

$$\mathbf{T}_{\text{ac}}(t) = \frac{\mathbf{P}_0 \mathbf{R}}{1 + (\omega \tau_{\text{ext}})^2} (\cos(\omega t) + \omega \tau_{\text{ext}} \sin(\omega t)) = \Delta \mathbf{T}_{\text{ac}} \sin(\omega t + \varphi) \quad (2.16a)$$

where

$$\Delta \mathbf{T}_{\text{ac}} = \frac{\mathbf{P}_0}{\mathbf{C}_p^{\text{sys}}} \frac{1}{\sqrt{\omega^2 + \frac{1}{\tau_{\text{ext}}^2}}} \quad (2.16b)$$

$$\tan \varphi = \frac{1}{\omega \tau_{\text{ext}}} = \frac{1}{\omega \mathbf{R} \mathbf{C}_p^{\text{sys}}} \quad (2.16c)$$

Eliminating τ_{ext} from the above equations, one has

$$\mathbf{C}_p^{\text{sys}} = \frac{\mathbf{P}_0}{\omega \Delta \mathbf{T}_{\text{ac}}} \cos \varphi \quad (2.17)$$

Note that one can write $\mathbf{T}_{\text{ac}}(t) = \Delta \mathbf{T}_{\text{ac}} \sin(\omega t + \varphi) = \Delta \mathbf{T}_{\text{ac}} \cos(\omega t + \varphi - \frac{\pi}{2})$ and compare it to the input power $\mathbf{P} = \mathbf{P}_0 \cos(\omega t) + \mathbf{P}_0$. There is a phase shift between the temperature and the power of $\Delta \Phi = \varphi - \frac{\pi}{2}$. In our group here at MIT, we call φ the phase shift. Note that $\varphi \approx 0$

when $\omega\tau_{\text{ext}}$ is large, which corresponds to our normal operating conditions.

Therefore, in this technique one measures the sample temperature $T(t)$ to get the amplitude ΔT_{ac} and the phase shift ϕ . Then C_p^{sys} can be calculated by using Eq. (2.17). Note that one does not need to measure the thermal resistance R explicitly since Eq. (2.17) depends on R only via the phase shift ϕ , which is a measurable quantity. It is obvious that $\phi = 0$ when $R \rightarrow \infty$. If the system satisfies the condition $\omega\tau_{\text{ext}} \gg 1$, then $\tan\phi = 1/\omega\tau_{\text{ext}} \ll 1$ and $\cos\phi \approx 1$. In this case Eq.(2.17) reduces to

$$C_p^{\text{sys}} \approx \frac{P_0}{\omega\Delta T_{\text{ac}}} \quad (2.17a)$$

and one does not even need to measure the phase shift ϕ . If the value of ϕ is small but not negligible (i.e., $\cos\phi \neq 1$) and is unknown due to complications with instrumental effects as discussed in Sec. 2.5D, one can approximate Eq. (2.17) by

$$(C_p^{\text{sys}})^2 \approx (P_0/\omega\Delta T_{\text{ac}})^2 - \frac{1}{\omega^2 R}, \quad (2.17b)$$

where R can be estimated from the dc temperature offset $T_{\text{dc}} - T_b = P_0 R$.

For a particular calorimeter design and experimental system, the time constant $\tau_{\text{ext}} = RC_p^{\text{sys}}$ is almost a constant (varies only due to the temperature dependencies of C_p^{sys} and R). In order to be able to use Eq. (2.17a), one would like to choose the operating frequency ω to satisfy $\omega \gg 1/\tau_{\text{ext}}$. However, there is an upper limit

for ω : it must be low enough so that $\omega \ll 1/\tau_{\text{int}}$, where τ_{int} is the internal time constant characterizing the thermal diffusion time scale inside the sample²⁻³. Therefore, in order to use Eq. (2.17a), the operating frequency of an ac calorimeter is limited to the range $1/\tau_{\text{ext}} \ll \omega \ll 1/\tau_{\text{int}}$, where τ_{ext} and τ_{int} depend on the calorimeter and cell design. The condition $\omega \ll 1/\tau_{\text{int}}$ is the more important since it is necessary in order to guarantee that there are no temperature gradients inside the sample when it is close to a transition. This basic ac method was invented in the 1960s by Kraftmaker² and by Sullivan and Seidel,³ and it has been widely used for studying liquid crystals by Johnson,⁴ Huang,⁵ and Garland.⁶ This even includes C_p measurements at high pressures.⁶

However, it is possible to go beyond these classical ac calorimeter designs. With a good experimental setup, one can determine the phase shift ϕ accurately and use Eq. (2.17) to determine the heat capacity values even when $\omega \gg 1/\tau_{\text{ext}}$ is not satisfied. Later in Sec. 2.3B and Chapter 5 we will see that the phase shift can be even more sensitive to phase transitions (especially first-order ones) than the heat capacity. So the operating frequency of an ac calorimeter can be extended to quite low frequencies, which is desirable for studying phase transitions. The heat capacity is a static property, so it should be obtained in the zero frequency limit of ac calorimetry. However, practical experimental conditions will pose a lower limit to the operating

frequency of an ac calorimeter. In order to explain this point, let us rewrite Eq. (2.6) as

$$C_p^{sys} \frac{dT}{dt} + \frac{T}{R} = P - \frac{dL}{dt} + \frac{T_b}{R} \quad (2.18)$$

It is interesting to note that the three terms on the right-hand side of Eq. (2.18) have equal footings. By this we mean the three terms are equivalent in determining a solution for T . For example, if the bath temperature T_b has an ac component $T_b = T_0 + T_0 \cos(\Omega t)$ due to the bath regulator, this gives on the right hand side of Eq. (2.18) a term $\frac{T_0}{R} \cos(\Omega t) + \frac{T_0}{R}$. Such a term will result in a temperature oscillation in the sample temperature at frequency Ω . This is directly analogous to the response of the system to an electrical power input $P = P'_0 \cos(\Omega t) + P'_0$. Thus when an ac calorimeter is operated at very low frequencies so that $\omega \approx \Omega$, one will encounter the problem that the bath temperature oscillations contribute noise to the data. This has been verified in our experiments.

One could carry out the ac mode operation at a particular sample temperature $T = T_b + P_0 R$ by holding the bath temperature T_b constant, as discussed above. But more efficient operations can be achieved by slowly scanning the bath temperature: $T_b = T_b(0) + \dot{T}_b t$, where $t=0$ represents the time when the heater on the sample is switched on. In this scanning ac mode, the sample temperature is given by

$$T(t) = T_{dc}(t) + T_{ac}(t) + T_{exp}(t), \text{ where}$$

$$T_{dc}(t) = T_b(0) + \dot{T}_b(t - \tau_{ext}) + P_0 R,$$

$$\mathbf{T}_{ac}(t) = \Delta\mathbf{T}_{ac} \sin(\omega t + \varphi), \quad (2.16a)$$

as before, and

$$\mathbf{T}_{exp}(t) = \left(\dot{\mathbf{T}}\tau_{ext} - \mathbf{P}_0\mathbf{R} \left[1 + \frac{1}{1 + (\omega\tau_{ext})^2} \right] \right) \exp(-t/\tau_{ext}).$$

In the steady state (after a time long enough so the exponential term is negligible) the system temperature has an ac component and a dc component: $\mathbf{T}(t) = \mathbf{T}_{dc}(t) + \mathbf{T}_{ac}(t)$, where we now have

$$\mathbf{T}_{dc}(t) = \mathbf{T}_b(0) + \dot{\mathbf{T}}_b(t - \tau_{ext}) + \mathbf{P}_0\mathbf{R} \quad (2.19)$$

B. Process With Latent Heat

In this case there are two coexisting phases which can interconvert via a first-order transition. If the latent heat is large enough, one should observe anomalous variations in the sample temperature. When latent heat is released, as in crystallization, the sample temperature is anomalously high. When latent heat is absorbed, as in melting, the sample temperature is anomalously low. These anomalous behaviors for the sample temperature can be used to identify first-order transitions. Here we distinguish two limiting cases for behavior in the two-phase coexistence region. The interconversion $\alpha \leftrightarrow \beta$ between the low-enthalpy phase α and the high-enthalpy phase β can be rapid or slow when the temperature is within the coexistence region.

Case One

Some first-order transitions are very “sluggish”, which means the conversion from one phase to another takes a long time. In our ac mode experiment, one data point usually requires six periods of temperature oscillation with a period of 32 seconds (i.e., 192 s = 3.2 min). If during this measurement time for an ac calorimeter data point, the release of latent heat is so slow that dL/dt is a smooth function of time, say a linear function $dL/dt = C + Dt$, then the latent heat effect is equivalent to a varying bath temperature [see Eq. (2.18)]. In this case, only T_{dc} changes as a result of two-phase coexistence. On a heating run, the T_{dc} value observed in the coexistence region will be smaller than that given by Eq.(2.19) and on a cooling run larger. In this limiting case, $\alpha \leftrightarrow \beta$ interconversion is not following the T_{ac} oscillations and there is no anomalous behavior for the phase shift ϕ . The analysis to obtain C_p is the same as if there were no latent heat:

$$C_p^{sys} = \frac{P_0}{\omega \Delta T_{ac}} \cos \phi .$$

Note that this heat capacity represents an average value for two coexisting phases α and β : $C_p^{sys} = X_\alpha C_p(\alpha) + X_\beta C_p(\beta) + C_p(\text{cell})$ where X_α is the mass fraction of the sample in the α phase and $X_\beta = 1 - X_\alpha$. This is the rare case when one can measure the $C_p(\text{coex}) = X_\alpha C_p(\alpha) + X_\beta C_p(\beta)$ [see Sec.2.1B], and the phase shift ϕ does not have anomalous values [see **case three**]. In Chapter 4 we

will encounter such a case involving nucleation and growth phenomenon for supercooled antiferroelectric liquid crystals.

Case Two

If the phase conversion ($\alpha \leftrightarrow \beta$) rate is very fast, the phase conversion would follow the sample temperature $T(t)$ oscillation in phase. In the ac mode, the sample temperature oscillation (sine wave) would not be distorted. In this case, one could obtain the effective heat capacity $C_{\text{eff}} = C_p^{\text{sys}} + \bar{L}(dm/dT)$ in the ac mode by an equation very similar to Eq. (2.17): $C_{\text{eff}} = \frac{P_0}{\omega \Delta T_{\text{ac}}} \cos \varphi$. To prove this, let us write $dL/dt = (dL/dT)(dT/dt)$, then Eq. (2.6) can be written in the form

$$C_{\text{eff}} \frac{dT}{dt} + \frac{T - T_b}{R} = P \quad (2.20)$$

where $C_{\text{eff}} = C_p^{\text{sys}} + dL/dT$ is the effective heat capacity as defined in Eq. (2.9). Note that Eq. (2.20) would be identical to Eq. (2.13) if one makes the mapping $C_{\text{eff}} \leftrightarrow C_p^{\text{sys}}$. So if the phase conversion rate were ideally fast and the sample temperature oscillation (sine wave) is not distorted, one gets $C_{\text{eff}} = \frac{P_0}{\omega \Delta T_{\text{ac}}} \cos \varphi$ from Eq. (2.20) [see the analysis of Eq. (2.17) in Sec. 2.3A].

This is the very rare case when one could measure C_{eff} in the ac mode. If this case were to occur, the phase shift data would not have anomalous behavior like that discussed below in **case three**, and the values of $C_{\text{eff}} = C_p^{\text{sys}} + \bar{L}(dm/dT)$ would be anomalously higher

than the C_p wings outside the two-phase coexistence region. In the past, some researchers (including our group) had found a few situations close to this ideal **case two**. We must stress however that one should measure the effective heat capacity C_{eff} in the linear power mode to be discussed in Sec. 2.4. The effective heat capacity C_{eff} is very useful in detecting first-order transitions and calculating the latent heats [see Sec.2.1B].

Case Two

Very often, the phase conversion rate is not low enough to satisfy **case one**, or high enough for **case two**. In this event dL/dt has a Fourier component at frequency ω that will act like a power at this frequency and its higher harmonics will also contribute. So the system temperature $T(t)$ will no longer exhibit a simple sinusoidal modulation but will be distorted by the latent heat. If the distortion is not too large, one could process the data as if there were no latent heat effects. Then one would get anomalous variations in “ ϕ ” and artificially large values for the “heat capacity”, as verified in our experiments. These “heat capacity” values have no physical meaning; they are larger than the C_p^{sys} values obtained in **case one** and smaller than the C_{eff} values obtained in **case two**. However, when there is no other means to detect first-order transitions in an ac calorimeter (for example, when the latent heat is too small to have an observable effect on T_{dc}), these anomalous variations in “ ϕ ” and artificially large values for the “heat capacity” are useful qualitative indications of

two-phase coexistence.

The anomalous behavior of ϕ at a transition where there is a two-phase coexistence region of finite width is an especially valuable qualitative indication of first-order character. Let us first sketch the behavior of $\tan\phi$ for a second-order transition where there is no two-phase coexistence but $C_p^{\text{sys}} = C_p(\text{cell}) + C_p(\text{sample})$, where $C_p(\text{cell})$ is a smooth function of T and $C_p(\text{sample})$ has a singular contribution (a peak). The thermal resistance R is also a smooth function of T ; thus according to Eq. (2.16c) $\tan\phi$ will exhibit a dip at a second-order transition, as shown in Fig. 2-3(a). When domains of two distinct phases coexist in a sample at a first-order transition, the internal heat transfer becomes complicated (see Chapter 5). The empirical result is a dramatic peak in $\tan\phi$, as shown in Fig. 2-3(b) and 2-3(c). This well-established qualitative feature occurs not only at strongly first-order transitions (see also Fig. 3-5 in Chapter 3) but also at weakly first-order ones like N-I transitions where there is appreciable pretransitional C_p behavior as well as a non-zero latent heat.⁷⁻⁹

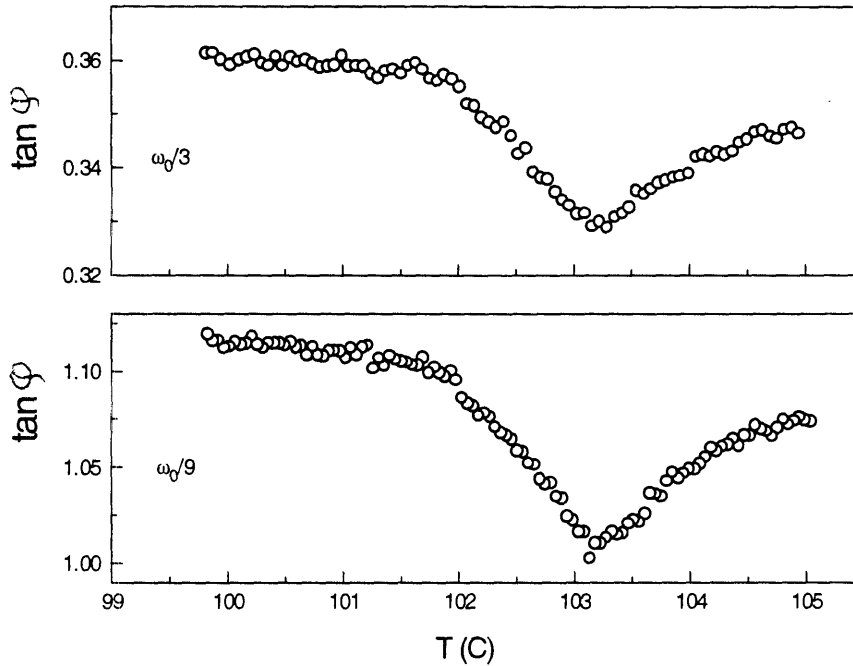


Fig. 2-3. (a) Typical $\tan \phi$ behavior near a second-order transition or a rounded “supercritical” maximum in the heat capacity. $\tan \phi$ shows a dip when C_p^{sys} exhibits a peak since $\tan \phi = 1/\omega R C_p^{\text{sys}}$. Note also that $\tan \phi$ is larger at all T for the lower frequency data, as expected. Data shown are from 9FBTFOM [see Chapter 5], where C_p^{sys} exhibits a finite maximum. For a second-order transition, C_p^{sys} is divergent and $\tan \phi$ exhibits a sharp cusp-like dip.

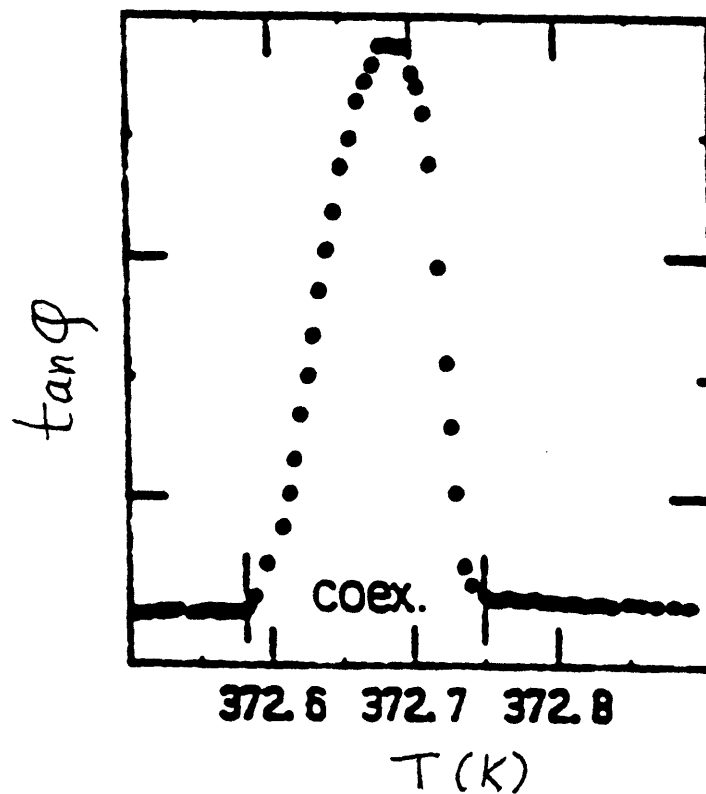


Fig. 2-3. (b) $\tan \phi$ behavior near a strongly first-order transition. The anomalous peaks indicate regions of two-phase coexistence. Data is for the $\text{Sm}\tilde{\text{C}}-\text{SmC}_2$ transition in mixtures of $\text{DB}_8\text{ONO}_2 + \text{DB}_{10}\text{ONO}_2$ (Ref.8); Fig. 3-5 provides another example similar to that shown here. In both cases the operating frequency was $\omega_0 = 0.196$.

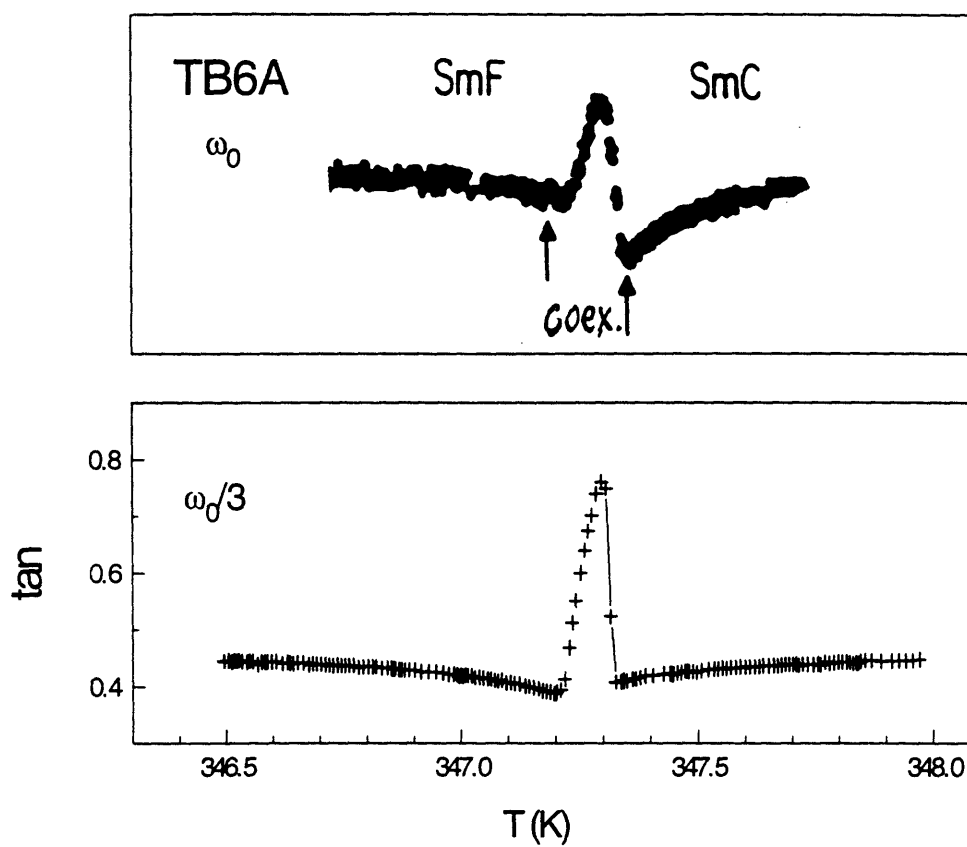


Fig. 2-3. (c) $\tan \phi$ behavior near a weakly first-order transition. Data at the top are for the SmC-SmF transition in TB6A.⁹ The data at the bottom are for the SmC*-SmI* transition in a mixture of 8SI and 8OSI. The operating frequency was $\omega_0 = 0.196$ or $\omega_0/3$.

In principle, latent heat can be measured by an ac calorimeter, but we will show that this is not efficient. The latent heat L is given by Eq. (2.8):

$$L = \int_{t_1}^{t_2} \left(P - \frac{T - T_b}{R} \right) dt - \int_{T_1}^{T_2} C_p^{sys} dT$$

Both the sample and bath temperatures can be (indeed are) carefully monitored as functions of time. If one can measure the thermal resistance R (to be described in the next section), then the latent heat is given by Eq.(2.8).

Obviously, it is not practical to work in the ac mode if one wants to measure quantitative latent heat values. From Eq. (2.8) we see that in order to measure latent heat, one needs to identify the two-phase coexistence region (i.e., locate T_1 and T_2). Even if this is done very well using the $\tan\phi$ behavior, there is the problem that the ac mode operation does not usually scan continuously from below T_1 (at time t_1) to above T_2 (at time t_2). Even if it did, both P and T are oscillating and it would be difficult to determine an accurate value for the difference $[P - (T - T_b)/R]$ as a function of time and to perform the numerical integration of these oscillating data using Eq. (2.8). If one wishes to use Eq. (2.10), then values are needed for the effective heat capacity C_{eff} . However, the apparent heat capacity data obtained in the coexistence region for **case three** cannot be used to do any quantitative analysis. One could attempt to use Eq. (2.9)

$$C_{eff} \equiv dH/dT = \left(P - \frac{T - T_b}{R} \right) / (dT/dt), \text{ but both } P \text{ and } T \text{ are oscillating in}$$

the ac mode. Thus it is difficult to carry out accurate numerical calculations to obtain C_{eff} .

In the next section we discuss a relaxation calorimeter, where the input power can be either a step function or a linear function of time. In the linear power mode, the system temperature changes almost linearly, similar to the case of adiabatic scanning calorimetry. Thus it is convenient to use a relaxation calorimeter in the linear power mode to measure latent heats.

2.4 Theory of Relaxation Calorimeter

at Constant pressure

In Sec. 2.3 we have discussed ac calorimetry, which has been used successfully to study the heat capacities of many materials. The essence of ac calorimetry is to detect the sample temperature response at a particular frequency ω . Thus it is robust against noise at frequencies other than ω . One can hold the bath temperature at a constant value, use a small heater power so ΔT_{ac} is small, and take as many sample temperature oscillation data as one wants. Therefore high-resolution C_p values can be obtained. Very slow linear scan or constant scanning rates for the bath temperature can also be used in ac calorimetry, which is very useful in studying phase transitions. However, it is not practical to use an ac calorimeter to measure latent heat values. We will see in this section that relaxation calorimetry can be used for this task.

Instead of putting a sinusoidal power into the system, one can switch on a constant power P_0 . In this case the system temperature will relax exponentially to a value that is higher than the bath temperature. If one then switches the power off, the system temperature will relax exponentially back to the bath temperature. In the standard operation of a relaxation calorimeter, one keeps the bath temperature T_b at a constant value. In reality, the bath temperature must be regulated with a feedback controller,

but the fluctuations in T_b are very small, typically less than 0.1 mK during our measurements.

A. Process Without Latent Heat

In this case, we start from Eq. (2.6) in the form of Eq. (2.13)

$$\frac{dT}{dt} + \frac{(T - T_b)}{RC_p^{sys}} = \frac{P}{C_p^{sys}}$$

Assume that the bath temperature T_b is constant.

1. **If the power is a step function**, say in a heating run

$$P = 0 \quad \text{for } t < 0 \quad (2.21a)$$

$$P = P_0 \quad \text{for } t \geq 0 \quad (2.21b)$$

Assuming R and C_p to be approximately constants, then

$$T(t) = T_b + P_0 R \{1 - \exp(-t/\tau_{ext})\} \quad \text{for } t \geq 0 \quad (2.22)$$

where $\tau_{ext} = RC_p^{sys}$. So the system temperature relaxes exponentially to a constant value

$$T(\infty) = T_b + P_0 R \quad (2.23)$$

In a cooling run, a constant power P_0 has been applied to the heater and the system has equilibrated to a constant temperature $T(\infty) = T_b + P_0 R$. Then the power is turned off:

$$P = P_0 \quad \text{for } t < 0 \quad (2.24a)$$

$$P = 0 \quad \text{for } t \geq 0 \quad (2.24b)$$

The system temperature will relax exponentially to the bath temperature:

$$T(t) = T_b + P_0 R \exp(-t/\tau_{ext}) \quad (2.25)$$

One has two choices for determining the heat capacity. One method is to fit the sample temperature with Eq. (2.22) or (2.25), get R and τ_{ext} , and then use

$$C_p^{\text{sys}} = \frac{\tau_{\text{ext}}}{R} \quad (2.26)$$

This method was developed in the 1970s and used for liquid crystals as early as 1974.¹⁰ Note that Eq. (2.26) is only applicable if C_p^{sys} does not change significantly over the temperature range of the relaxation. Recently, Ema et al.¹¹ have improved the implementation of the step-power relaxation method. In order to deal with the cases where C_p^{sys} may vary significantly over the temperature range of the relaxation (and cases where a first-order transition occurs during the relaxation, see Sec. 2.4C), they introduced a time-dependent heat capacity $C_p(t)$ concept. This approach is based on the direct use of Eq. (2.7):

$$C_p^{\text{sys}}(t) = \frac{P - \frac{T - T_b}{R}}{dT/dt} \quad (2.7)$$

This second method has not been widely used but is very attractive for the linear-power mode of relaxation calorimetry developed by Dr. Haruhiko Yao and the author (described in paragraph 2 below). In this case one needs to measure the thermal resistance R , and we will discuss this shortly. Equation (2.7) works for all choices of power P . But in the case of a step function for the power, we see that the derivatives

$$\frac{dT}{dt} = \pm \frac{P_0 R}{\tau_{\text{ext}}} \exp(-t/\tau_{\text{ext}}) \quad (2.27)$$

decay exponentially to zero, which makes numerical calculations with Eq. (2.7) unstable at long times. The linear power mode was introduced to solve this problem.

2. **If the power P is a linear function of time**, say in the heating mode $\dot{P} = dP/dt = \text{const}$ and

$$P = 0 \quad \text{for } t < 0 \quad (2.28a)$$

$$P = \dot{P}t \quad \text{for } 0 < t \leq t_1 \text{ (}\dot{P} \text{ positive)} \quad (2.28b)$$

$$P = P_0 \quad \text{for } t > t_1, \text{ where } P_0 \equiv \dot{P}t_1 \quad (2.28c)$$

Assuming R and C_p^{sys} to be constants, the solution of Eq.(2.6) with $L=0$ for T is

$$T = T_b + \dot{P}R(t - \tau_{\text{ext}}) + \tau_{\text{ext}}R\dot{P}\exp(-t/\tau_{\text{ext}}) \quad \text{for } 0 < t \leq t_1 \quad (2.29)$$

In the cooling mode the power is

$$P = P_0 \quad \text{for } t < 0 \quad (2.30a)$$

$$P = P_0 - |\dot{P}|t \quad \text{for } 0 < t \leq t_1 = P_0/|\dot{P}| \text{ (}\dot{P} \text{ negative)} \quad (2.30b)$$

$$P = 0 \quad \text{for } t > t_1 \quad (2.30c)$$

Again, assuming R and C_p^{sys} to be constants, the solution of Eq.(2.16) with $L=0$ for T is

$$T = T_b + P_0R - |\dot{P}|R(t - \tau_{\text{ext}}) - \tau_{\text{ext}}R|\dot{P}|\exp(-t/\tau_{\text{ext}}) \quad \text{for } 0 < t \leq t_1. \quad (2.31)$$

So the system temperature relaxes exponentially to a “long-time” (but $t < t_1$) linear function of time: $T = T_b + \dot{P}R(t - \tau_{\text{ext}})$ in the heating mode and $T = T_b + P_0R - |\dot{P}|R(t - \tau_{\text{ext}})$ in the cooling mode. In this linear power mode, one can scan the system temperature, which varies almost linearly except for a brief period just after $t=0$, through a wide range of temperature with a convenient scanning rate. The

value of C_p^{sys} is calculated from Eq.(2.7) where P is the power at a certain time t' corresponding to sample temperature T and dT/dt is determined by numerical differentiation of $T(t)$ data over a time interval centered at t' .

B. Measurement of R When There Is No Latent Heat

In order to use the linear power mode, one needs to measure the thermal resistance R . One observes from Eq. (2.6) that if $dT/dt = 0$ and $L=0$, then $R = (T - T_b)/P$. So in order to measure R , one can control the system at a constant temperature well away from any two-phase coexistence region. In practice, we keep the bath at constant temperature T_b , and input a small constant dc power P_1 . After a transient period, the system temperature will reach a constant value T_1 . When we change the power to a slightly different value P_2 (usually set to be zero by switching off the power), the system will reach another constant temperature T_2 after some time. From the relations $P_1 R(T_1) = T_1 - T_b$, $P_2 R(T_2) = T_2 - T_b$ and $R(T_1) \approx R(T_2)$, we have

$$R = \frac{T_2 - T_1}{P_2 - P_1} \quad (2.32)$$

Note that if there are latent heat effects, Eq. (2.32) cannot be used to obtain the value of the thermal resistance R . One should measure R outside any two-phase coexistence region and interpolate the R values inside such regions.

C. Process With Latent Heat

Parallel to the discussion in Sec 2.1, we introduce the effective heat capacity as in Eq. (2.9). One has even in a two-phase region

$$C_{\text{eff}} \equiv \frac{dH}{dT} = \frac{\left(P - \frac{T - T_b}{R} \right)}{dT/dt} \quad (2.9)$$

This effective heat capacity is identical to the system heat capacity C_p^{sys} outside a two-phase coexistence region. One identifies a first-order transition by observing anomalous behavior in C_{eff} . The two-phase coexistence region usually has hysteresis.

The latent heat is given by Eqs. (2.10) and (2.8):

$$L = \int_{T_1}^{T_2} [C_{\text{eff}} - C_p^{\text{sys}}] dT = \int_{t_1}^{t_2} \left(P - \frac{T - T_b}{R} \right) dt - \int_{T_1}^{T_2} [C_p(\text{cell}) + C_p(\text{coex})] dT$$

where two-phase coexistence is between temperatures (times) T_1 (t_1) and T_2 (t_2), and $C_p(\text{coex})$ is the heat capacity of the two coexisting phases that would be observed in the absence of phase conversion, i.e., $C_p(\text{coex}) = X_\alpha C_p(\alpha) + X_\beta C_p(\beta)$ as discussed in Sec. 2.1. The latent heat L corresponds to the shaded area in Fig. 2-2 (b4). It is best to carry out the measurement of C_{eff} in the linear power mode, which is very similar to scanning adiabatic calorimetry except heat leak is finite here rather than zero; see Eq. (2.12). Indeed, our linear-power relaxation method could best be called nonadiabatic scanning calorimetry.

2.5 Design And Operation of An

AC Calorimeter

The zero-dimensional model of thermal analysis described in the preceding sections is surprisingly simple. It has been applied to high-resolution ac calorimetric studies of liquid crystals in the pioneering works of Johnson,⁴ Huang,⁵ and Garland,⁶ and later extended by Ema¹¹ to relaxation calorimeters. These ingenious designs are superior in many ways to commercial calorimeters like DSC (differential scanning calorimeter) and DTA (differential thermal analysis). Such machines have high sensitivity for detecting small enthalpy changes, but their absolute accuracy is poor, the scanning rates (usually several degrees per minute) are too fast to permit thermodynamic equilibrium near a phase transition, and temperature resolution is very low. Compared to classical ac calorimetry,³ the MIT ac calorimeter is more versatile. It can operate over a range of low frequencies, which makes it useful in studying a wide variety of bulk samples, including solids, liquids, liquid crystals, and even aerogels. Design and operation of this calorimeter (called calorimeter A) was described in great detail by Dr. K. Stine in his Ph.D. thesis.¹² We will briefly describe it in this section with emphasis on recent improvements made by Dr. Haruhiko Yao and the author.

Figure 2-4 gives a block diagram of Calorimeter A, the standard ac calorimeter used for several years in our laboratory.

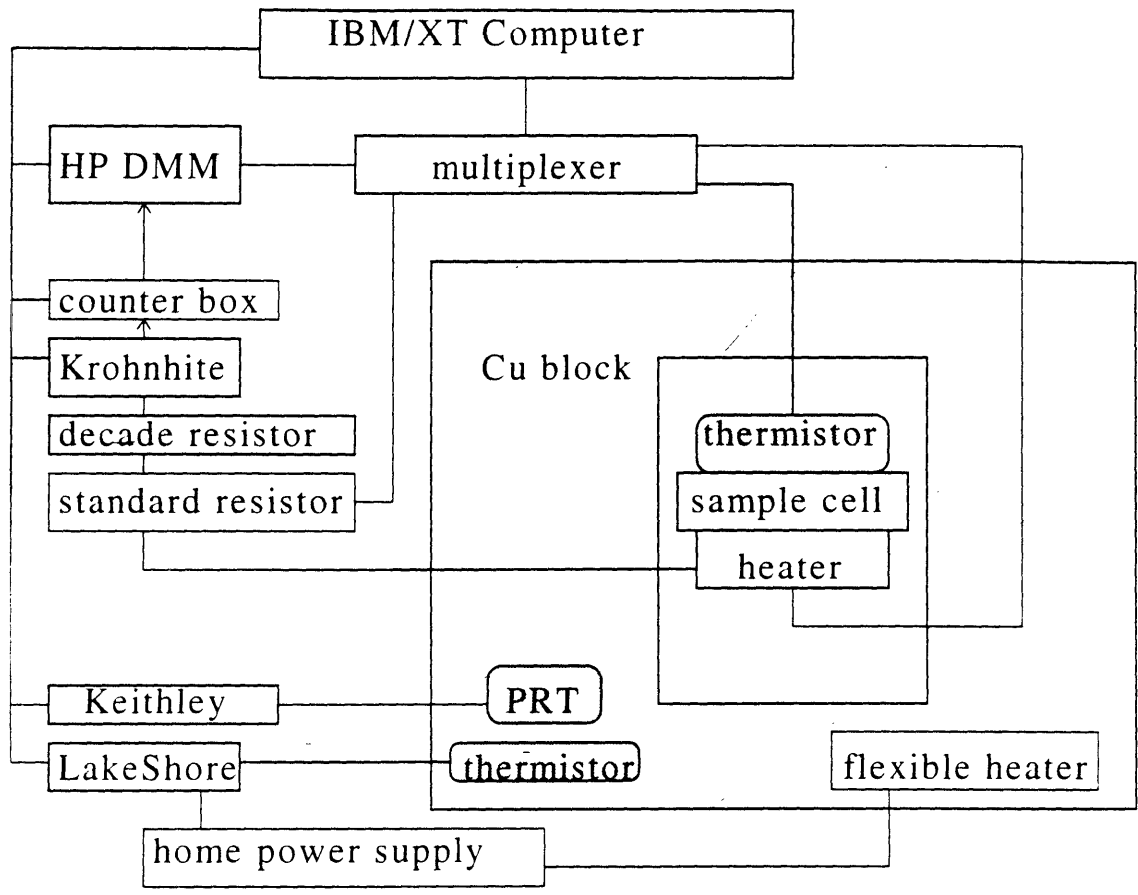


Fig. 2-4. Block diagram of Calorimeter A (modified version of the design described by K. Stine¹²).

In this design, a sample+cell of heat capacity C_p^{sys} is loosely coupled to a heat bath at temperature T_b . For an oscillatory power input $P = P_0 \cos(\omega t) + P_0$, the sample temperature is given by $T(t) = T_{dc} + \Delta T_{ac} \sin(\omega t + \phi)$. For a bulk sample (typically 20-100 mg) at 1 atm, the sample thickness and operating frequency ω can be chosen so that the simple expression $C_p^{sys} = P_0 / \omega \Delta T_{ac}$ is an excellent approximation.

A. Sample Cell

The design, construction, and filling of the sample cell used at MIT is described in detail by Keith Stine¹² and is summarized below. This cell is made of silver and is shown schematically in Fig.2-5. The only modification of Stine's procedure is the dilution of the GE varnish.

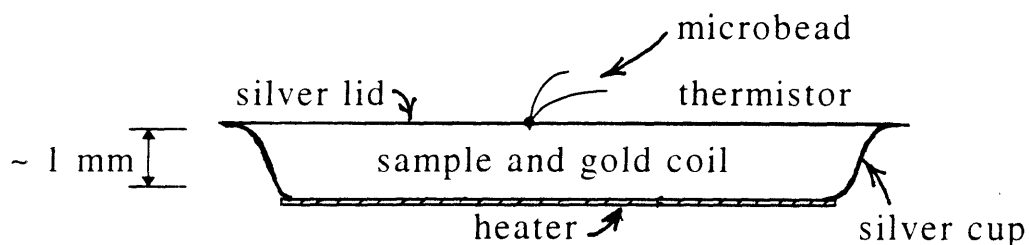


Fig. 2-5 Schematic view of sample cell.

A strain gauge, which serves as the heater, is attached to the bottom of the shallow silver cup using diluted GE 7031 varnish. The diluting solvent is a 50:50 (by volume) mixture of toluene and ethanol. The strain gauge is either model 120LG13 from

Omega Engineering or model FAE-25-12 S13 EL from BLH Electronics, with a resistance of 120 ohms. When the sample is a liquid or liquid crystal, a helical coil of fine gold wire is placed in the silver cup to increase the effective thermal conductivity of the sample. After loading the cell with the sample, a silver foil lid is cold-welded to the silver cup using indium or tin. The temperature sensor is a microbead thermistor from Victory Engineering, which is attached to the center of the silver lid with the diluted GE varnish.

A slight modification of the Stine cell design is used at the Tokyo Institute of Technology, where gold is used in place of silver. As a result, it is possible to directly cold-weld the lid to the cup without the use of indium or tin. The main advantage of a gold cell is that it is chemically stable. This is a desirable improvement since it also improves the thermal conductivity of the cell body. However, the cost is appreciably greater.

B. Temperature Control

Before recent improvements, temperature control was achieved by regulating the temperature of an oil bath (Lauda KS20D), and the sample holder was inside a massive copper block immersed in the oil. The purpose of the copper block was to damp out the short-term temperature fluctuations. This style of temperature control was beset by problems with intermediate-term temperature fluctuations (time scale 1-10 min) of about ± 1 mK,

which is not desirable for very-high resolution calorimetry. For details of this old method see Stine's thesis.¹²

Dr. H. Yao and the author have made major modifications to the temperature control. Instead of using an oil bath to control the bath temperature and a copper block to damp the temperature fluctuations, we now control the temperature of the massive copper block directly. See Fig. 2-6.

The sample holder is mounted with six bolts in the massive copper block. A gas-tight seal is achieved with an O-ring set in a circular groove around the top surface of the copper block. A Kapton insulated flexible heater from Omega Engineering is glued on the outer surface of the copper block. Heating power is supplied to this heater by a home-made power supply. The composite assembly of sample holder and copper block is suspended from a wooden plate on top of the oil bath (Lauda KS-20D temperature controller) but is not immersed in the oil. The copper block is surrounded by a large open-top copper can, which is immersed in the oil bath to prevent oil from coming into direct contact with the copper block. The Lauda oil bath temperature is controlled by its feedback system and a stability of ± 0.1 K can be achieved. To control the "thermal bath" temperature, a thermistor is attached to the copper block. This thermistor serves as the sensor for a LakeShore DRC81-C temperature controller, which outputs a control voltage to the home-made power supply, which in turn outputs control power to the Kapton insulated flexible

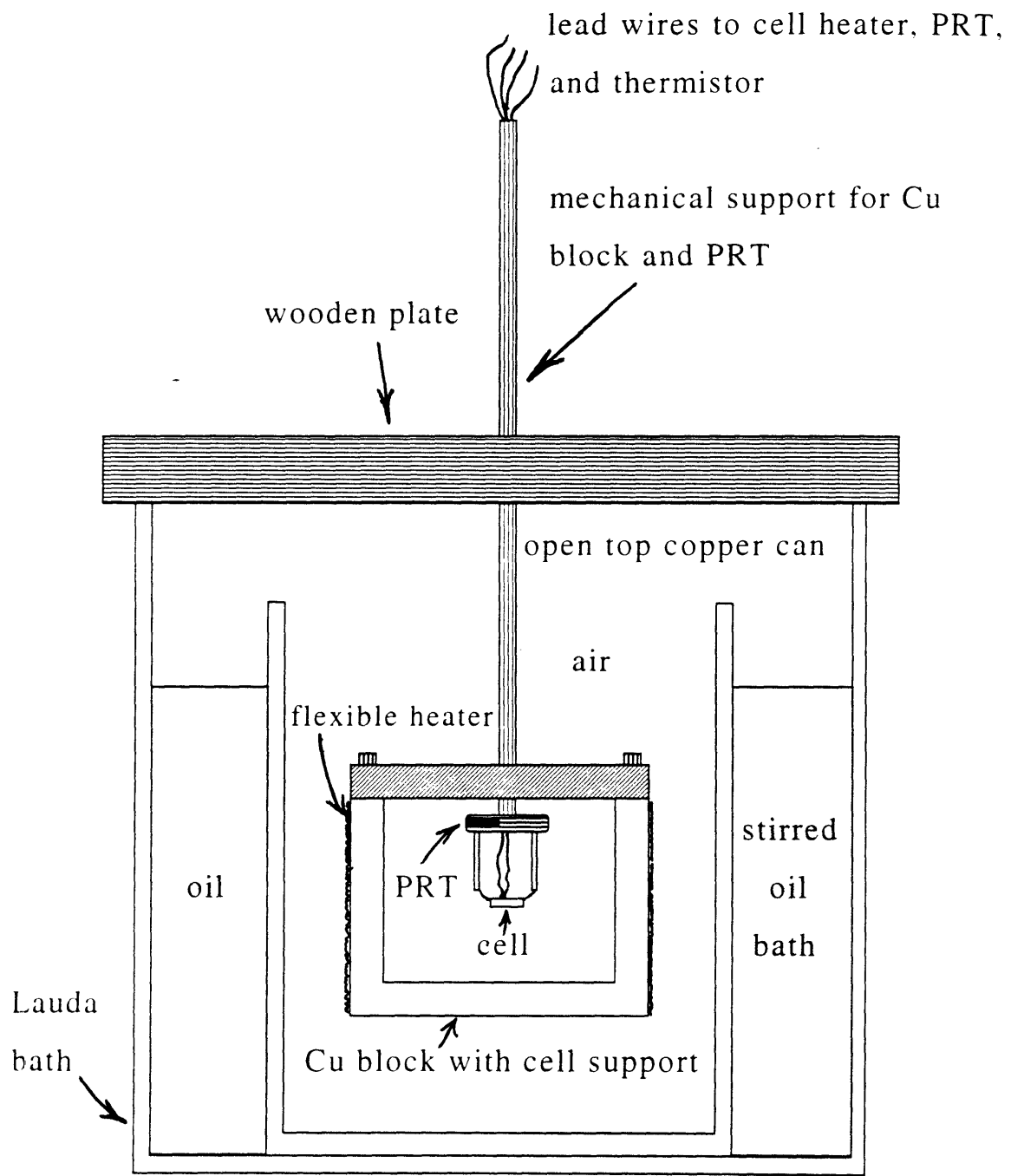


Fig. 2-6. Temperature control method for Calorimeter A. The circuitry for the Lauda bath is not shown here.

heater on the copper block. This feedback procedure can achieve a stability of ± 1 mK for the temperature of the copper block over a period of 30 minutes. The scanning of the bath temperature is accomplished using a home-made programmable voltage offset generator as described by Stine.¹² This allows one to choose scanning rates over the range 1 mK/h to 3 K/h.

C. Electronic Circuitry

The design and basic electronic circuitry of calorimeter A are the same as those described by Stine,¹² but a number of improvements have been made. A brief summary is given below with indications of the elements that have been changed.

The electrical power dissipated in the strain-gauge heater is provided by a Krohnkite 1920 arbitrary function generator. The output of the Krohnkite is applied to a circuit made of the strain-gauge heater and a General Radio $1M\Omega$ decade resistor in series with the heater. One changes the heater power by selecting an appropriate value of the decade resistor. A standard resistor with resistance R_{std} is also in series with the strain gauge and is used for determining the heater current I . The automated measurements of resistances and voltages are made possible by a home-made multiplexer interfaced to the digital I/O board inside an IBM/XT computer. The multiplexer is instructed by the computer to select one of the inputs to a HP 34401A multimeter interfaced to the computer through a Tecmar IEEE-488 board. The readings of the multimeter are triggered by a TTL (transistor-transistor logic)

pulse originating from the Krohnkite. In arbitrary function mode, the Krohnkite outputs a TTL pulse for every point in the waveform. This TTL signal passes through a counting circuit designed in 1988 by Dr. K. Ema; this circuit changes the period of the original TTL into a specified value, say 0.5 second. This controlled TTL triggers the reading of the thermistor resistance that measures the system temperature $T(t)$. At each zero crossing of the voltage signal, the Krohnkite outputs a separate TTL pulse through the ARB-Z output on the back panel. This TTL signal is used to synchronize the measurements (to trigger the meter so it starts reading). After measurement of one C_p data point (several periods of temperature oscillation), the counting circuit is reset by the computer through the DIO board, and the data taking is re-synchronized by the ARB-Z output.

The resistance of the thermistor attached to the sample cell is read directly by the HP multimeter with the triggering method described above. The thermal bath temperature T_b is measured by reading the resistance of a Platinum Resistance Thermometer (PRT) attached to the sample holder. The PRT is model 146MA1000F from Rosemount (its resistance is about 1000 ohms at 0°C), which is calibrated against the IPTS-1968 standard. A Keithley 192 multimeter is dedicated to measuring the PRT resistance. Note that we program the Keithley so it reads the PRT resistance continuously during the measurement of a data point. In the resistance mode of the Keithley multimeter, a current is sent

through the PRT and this measurement current will heat up the PRT. By dedicating the Keithley to continuous PRT readings we avoid transient self-heating effects. (This procedure also avoids transient self-heating effects of the thermistor used to monitor the sample temperature, since the HP can be dedicated to the thermistor.) The self-heating effects of the Keithley measurement current makes a constant correction to the PRT temperature: $T_{\text{PRT}} = T_b + \Delta T$, where T_b is the bath temperature and $\Delta T < 10$ mK is a constant during the experiment. We will ignore this constant correction and let $T_{\text{PRT}} = T_b$ when we calibrate the sample thermistor. This new method of monitoring the bath temperature is an improvement over the one described by Stine.¹²

D. Data Acquisition

Data acquisition is achieved with software written in C under VENIX on the IBM/XT computer. At the beginning of a data point measurement, the computer resets the counting circuit to the state where it will not produce TTL pulses until it detects a TTL pulse from the ARB-Z output of the Krohnkite. The reset pulse is provided by the DIO (digital I/O) board inside the computer. The computer reads the output from the counting circuit to the DIO board. When the first TTL pulse is received, it commands the HP meter to begin readings of thermistor resistance. Each reading is triggered by detecting the high to low transitions of the TTL train coming into the DIO board.

The user needs to choose the magnitude and frequency of the ac heater power. A sinusoidal voltage signal is produced by the Krohnkite generator in its arbitrary function mode, and the voltage amplitude is set to its maximum value (15V). Since the voltage from the Krohnkite is $V = V_0 \cos(\omega t/2)$, the power $P = P_0 + P_0 \cos(\omega t)$ has an ac component with frequency ω and a dc component. In reality, the Krohnkite generator gives a voltage wave that has a very small dc component: $V = V_0 \cos(\omega t/2) + \delta V$, so the power is actually

$$P \approx P_0 + P_0 \cos(\omega t + \phi_p) + P_1 \cos(\omega t/2 + \phi_1) \quad (2.33)$$

and there will be a “beat” with frequency $\omega/2$ in the observed temperature oscillation. The phase shift ϕ_p is due to instrumental resolution (for example, finite integration time of the digital multimeter).

Before a heat capacity measurement begins, the thermal bath is equilibrated to a desired starting temperature measured by reading the resistance of the PRT. Then the heater power is measured. The multiplexer selects the proper channels for the HP multimeter. This multimeter reads the voltage drop across the strain gauge and then that across the standard resistor. These data are stored in the computer. The product $P = IV_H = V_H V_{std} / R_{std}$ is calculated and fitted with (2.31) to obtain P_0 and ϕ_p . If one chooses to operate the ac mode at frequency ω (for temperature oscillation), then the voltage frequency of the Krohnkite should be set to $\omega/2$ so as to get a power at frequency ω . The power measurement should be made at this frequency (ω) in order to get

the phase shift φ_p at this particular frequency. This φ_p will be used later to calculate the phase shift φ .

After measuring the bath temperature, the sample temperature $T(t)$ is monitored by recording the resistance of the microbead thermistor attached to the sample cell. The thermistor resistance R_{th} can be converted into temperature using the empirical formula

$$\frac{1}{T} = a_0 + a_1 \ln\left(\frac{R_{th}}{R_0}\right) + a_2 \left[\ln\left(\frac{R_{th}}{R_0}\right) \right]^2 \quad (2.34)$$

where T is in kelvin, a_0 , a_1 , a_2 and R_0 are positive constants (R_0 is set to 10 k Ω in our experiments). The form used in Eq. (2.34) is a good representation over a range of about 20 K. At the end of several periods of sample thermistor readings, the PRT (bath) temperature is determined again. During a series of measurements, the bath temperature is programmed to change linearly with time. Thus the bath temperature corresponding to a data point can be interpolated from the two PRT readings, and the thermistor is calibrated according to Eq (2.34) after the entire experimental run is finished.

Since the amplitude of the temperature oscillation ΔT_{ac} is small, the raw data $R_{th}(t)$ are fitted to

$$R_{th}(t) = (A + Bt) - \Delta R_{ac} \sin(\omega t + \varphi_R) - \Delta R' \sin(\omega t/2 + \varphi') \quad (2.35)$$

and the values A , B , ΔR_{ac} , and φ_R (also $\Delta R'$ and φ') are stored for later data processing. For a given data point, the measurement of this resistance starts at time t_i and continues for several periods

of sample temperature oscillations ending at time t_f . In order to calibrate the thermistor, we take the average value of the thermistor resistance $\bar{R}_{th} = A + Bt_{mid}$ over this time interval, where $t_{mid} = (t_i + t_f)/2$. We need the temperature value corresponding to this \bar{R}_{th} . The sample temperature in steady state is $T(t) = T_{dc} + T_{ac}$, where $T_{ac}(t) = \Delta T_{ac} \sin(\omega t + \phi_R)$ and $T_{dc} = T_b + P_0 R$ [Eq. (2.15)] or $T_{dc} = T_b(0) + \dot{T}_b(t - \tau_{ext}) + P_0 R$ [Eq. (2.19)]. Thus the average sample temperature during the measurement is $\bar{T} = \langle T(t) \rangle = \langle T_b \rangle + P_0 R - \dot{T}_b \tau_{ext}$. The bath temperature T_b is monitored by the PRT, so $\langle T_b \rangle = T_{PRT}(t = t_{mid})$ can be interpolated from the two PRT readings. The thermal resistance R can be estimated by Eq. (2.32), and τ_{ext} is given by $\tau_{ext} = RC_p^{sys}$. Thus the corrections to $\langle T_b \rangle$ can be evaluated. Typical values are $P_0 R \approx 50$ mK for $P_0 \approx 0.3$ mW and $\dot{T}_b \tau_{ext} \approx 1$ mK when $\dot{T}_b \approx 100$ mK/h. Finally, the calibration is made with Eq. (2.34) and \bar{R}_{th} , \bar{T} values from every data point in the experimental run (often 1000 points) over typically 10 K.

The ac component of the sample temperature is $T_{ac}(t) = \Delta T_{ac} \sin(\omega t + \phi_R)$, where we can use the approximation $\Delta T_{ac} \approx \left| \frac{dT}{dR} \right| \Delta R_{ac}$ and the phase shift ϕ appearing in Eq. (2.17) is given by $\phi = \phi_R - \phi_p$. The sensitivity dT/dR can be obtained from (2.34) after the coefficients are determined by the calibration, and it is negative. The heat capacity is calculated from $C_p^{sys} = \frac{P_0}{\omega \Delta T_{ac}} \cos \phi$.

Since the heat capacity depends in effect on ΔR_{ac} , $|dT/dR|$, and ϕ , the calibration with Eq. (2.34) is most important in allowing one to determine an accurate thermistor sensitivity $|dT/dR|$. Any errors in the evaluation of P_0R only influence the absolute temperature of the average sample temperature \bar{T} and have almost no effect on $|dT/dR|$ and thus no effects on C_p^{sys} .

Using faster computers with larger memory, one could record all the thermistor readings in the memory for later data processing. This would be valuable because one could then search for distortions of the sinusoidal oscillation by latent heat effects. If such a distortion is found, one cannot interpret the results of the usual fitting procedure as the true heat capacity C_p^{sys} and the true phase shift ϕ . However, these artificial values may serve as indications of two-phase coexistence as discussed in Sec.2.3.

It should be noted that we have extended the operating frequency to lower values than the standard frequency ω_0 used in this lab for many years. This is because improvements in temperature control and data acquisition allow us to obtain quantitative information about the phase shift. So it is not necessary to operate only at the standard frequency $\omega_0 = \frac{2\pi}{32\text{sec}} = 0.19635$, which gives a phase shift $\phi = 0.1 - 0.2$ (thus $\cos\phi = 0.98 - 0.995 \approx 1$) for our design. We have achieved operation at frequencies as low as $\omega_0/9$ (period=288 sec=4.8 min). As discussed in Sec. 2.3A, the lower limit of the operating frequency

is set by the quality of the bath temperature control. It takes about 30 min to finish one data point measurement at $\omega_0/9$ operation (if six periods of $T(t)$ data are taken), during which time the bath temperature will fluctuate by about ± 1 mK for calorimeter A.

2.6 Design and Operation of Relaxation Calorimeter

During the past few years, the research group of Prof. K. Ema at the Tokyo Institute of Technology has developed a complex calorimeter design¹¹ that allows operation in an ac mode or in a relaxation mode. The latter mode makes it possible to measure latent heats at first-order transitions, which is an attractive augmentation of the heat capacity capabilities of ac calorimetry.

Based on refinements of the designs used previously at MIT and TIT, Dr. Haruhiko Yao and the author have constructed a new complex calorimeter which operates in both ac mode and relaxation mode. The design of this instrument, called Calorimeter B, is described in subsections A-D and its operation is described in subsections E and F.

A. Sample Cell

The cell used with Calorimeter B can be designed to be identical to that used with calorimeter A and already described in Sec. 2.5A and Stine's thesis.¹² This makes it possible to

move a sample from one calorimeter to the other with complete freedom.

However, Dr. H. Yao has modified the method of cell mounting. Instead of using enamel-insulated AWG 28 copper wire to support the cell,¹² (note that heater leads also serve to support the cell, but are not strong enough), one can use nickel chrome wire with a diameter of about 2 μm to suspend the cell. This procedure can reduce the heat capacity contribution to C_p^{sys} from the wire and increase the thermal resistance due to the wire. The thermal resistance due to these wires can be estimated from $R_{\text{wire}} \sim L/\kappa A$, where κ is the thermal conductivity of the wire, L is the length (~ 1 cm), and A is the cross-section ($\sim 10^{-8}$ cm^2). The result is $R_{\text{wire}} \sim 10^6$ K/W, which is much larger than the typical values of the effective thermal resistance $R \sim 150$ - 200 K/W measured in our experiments without vacuum. (With vacuum the thermal resistance increases by about 20%.) Thus the effective thermal resistance is determined by the heater leads, the radiation loss and the conduction via the air.

B. Temperature Control

Unlike the situation with the old calorimeter used from 1988 to 1993 and described by Stine,¹² where a stirred oil bath was used for controlling the sample temperature, or the revised design for calorimeter A described in Sec. 2.5 B, no oil bath is used for calorimeter B. The temperature control is achieved with a copper block surrounded by a heated copper can and

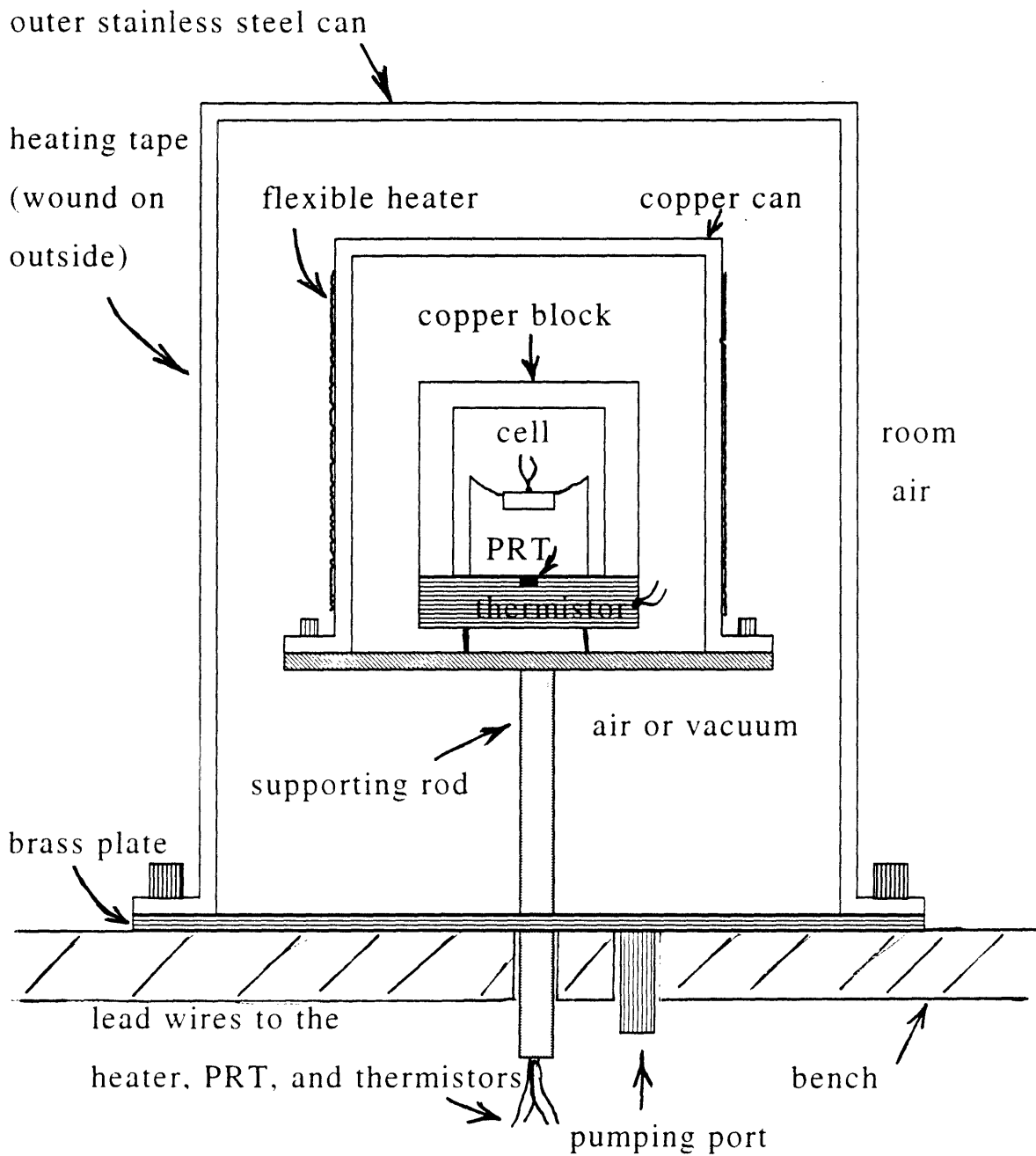


Fig. 2-7. Mechanical/thermal design of Calorimeter B.

outer stainless-steel can. A schematic diagram of the inner parts of this assembly is given in Fig. 2-7.

The massive hollow cylindrical copper block is 50 mm in diameter and 50 mm in height. It has an inner space of 34 mm in diameter and 30 mm in height, in which the sample cell is mounted by suspending the cell from thin copper wires and the electrical leads of the strain gauge. This block is surrounded by a heated copper can that is secured with six bolts. A gas-tight seal is achieved with an O-ring set in a circular groove around the bottom surface of the copper can. This seal allows one to control the pressure of the gas inside the copper can and the inner copper block by pumping with a Welsh Duo-Seal vacuum pump. The lowest pressure that can be achieved is ~ 0.05 torr. This procedure will increase the thermal resistance between the sample cell and the thermal bath and can also improve the sample temperature stability. A Kapton insulated flexible heater from Omega Engineering is glued on the outer surface of the copper can. Heating power is supplied to this heater by a Kepco power supply. The assembly of thermal bath (copper block) and the heated copper can is enclosed by a large stainless-steel can, which is mounted by six bolts to the brass base plate and is sealed by an O-ring.

To control the thermal bath temperature, a thermistor is attached to the copper block. The thermistor and a home-made programmable six-decade precision resistor comprise two arms

of an ac (10 Hz) Wheatstone bridge, which is in balance when the thermistor and the programmable resistor have the same electrical resistance. This bridge, which is denoted as bridge 1, is shown schematically in Fig. 2-8.

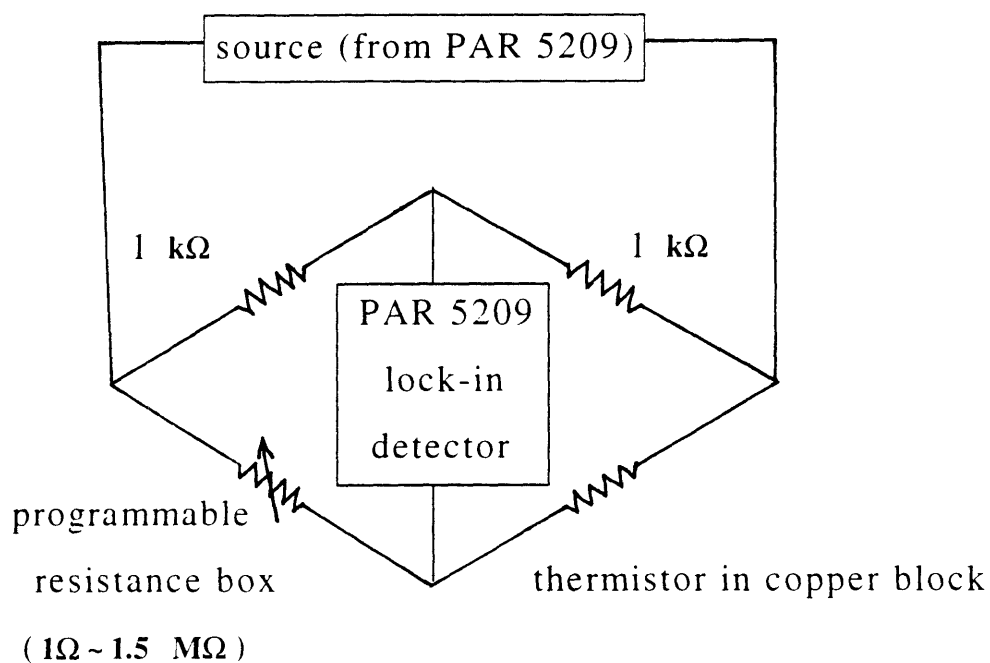


Fig. 2-8. Bridge 1' diagram. Used to sense/control the temperature of the copper block.

The bridge imbalance signal is fed into a PAR 5209 lock-in amplifier. The amplified imbalance signal is input to a PID feedback controller, which outputs a control voltage to the Kepco power supply, which in turn outputs control power to the Kapton insulated flexible heater on the copper can. This

feedback procedure can achieve a stability of ± 0.1 mK for the temperature of the copper block over a period of 24 hours. The outer stainless-steel can is in contact with the room environment, but its temperature is controlled by a LakeShore DRC81-C temperature controller. A thermistor attached to the surface of the stainless steel can serves as the temperature sensor for the LakeShore controller, and heating is achieved with a heating tape wrapped around the surface of the can.

C. Electronic Circuitry

The source of power for the strain-gauge heater (a Krohnkite 1920 arbitrary function generator) and the method of measuring this input heater power are almost the same as those described for calorimeter A in Sec. 2.5C except that the standard resistor is omitted and the decade resistor is used to calibrate the heater power. The generation of TTL trigger pulses is also accomplished in the same fashion as described previously. However, several items of equipment have been upgraded for calorimeter B and the measurement of the thermistor and PRT resistance are carried out in a different manner.

The automated measurements of resistances and voltages are made possible by a home-made 6-channel multiplexer interfaced to a National Instrument DIO-96 digital I/O board inside a Dell 486SX/25 computer. The multiplexer is instructed by the computer to select one of the inputs to a HP 34401A

multimeter interfaced to the computer through a National Instrument GPIB-PCII board.

The thermistor attached on the sample cell and a home-made programmable six-decade precision resistor comprise two arms of an ac Wheatstone bridge, which balances when the two resistances are equal. This bridge, which is denoted as bridge 0, is shown schematically in Fig. 2-9.

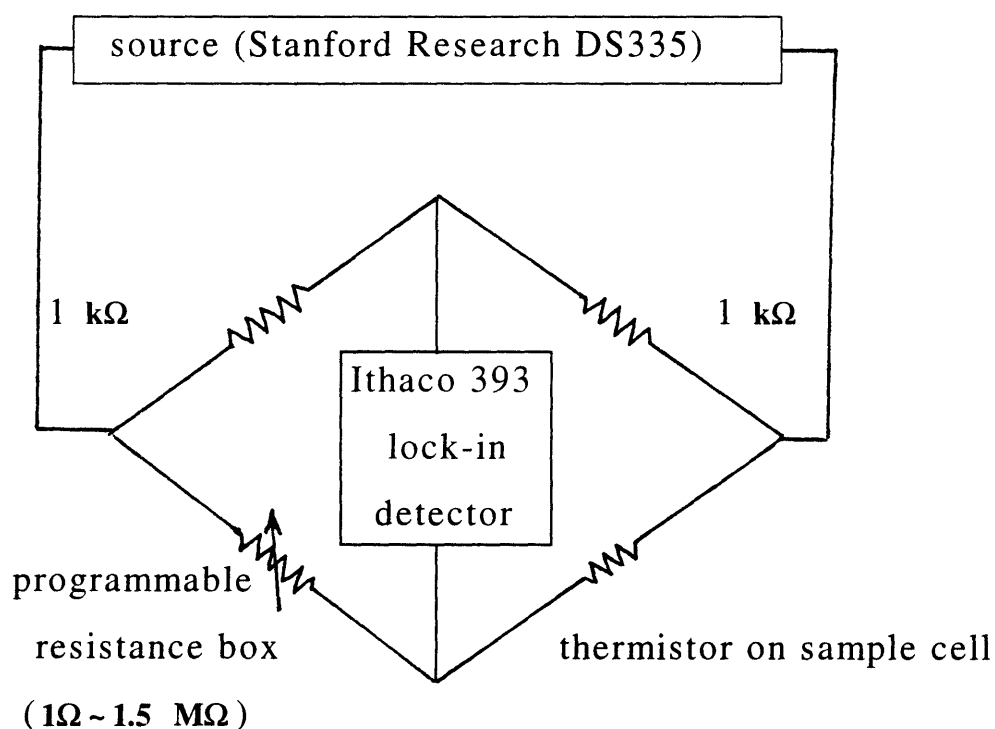


Fig. 2-9 Bridge 0 diagram. Used to detect $R_{th}(t)$ of thermistor (nominal $R_{th}=0.2\sim 5$ MΩ at room temperature).

The bridge is driven by a Stanford Research DS 335 function generator at 24 Hz. The imbalance signal is sent to an Ithaco model 393 lock-in amplifier and read by the HP multimeter with the triggering method described in Sec. 2.5C, and the variations in thermistor resistance can be calculated.

Note that we do not measure the thermistor resistance directly. This is because we wish to determine as accurately as possible small variations of the thermistor resistance $\Delta R(t)$. The HP meter has only $6\frac{1}{2}$ digits resolution, and the resistance is in the range of 50 k Ω to 1 M Ω . Thus round-off errors will represent significant “noise” relative to $\Delta R(t)$ if we read the resistance directly. The ac bridge method used here gives greater resolution in $\Delta R(t)$ than the direct reading of the resistance because one can choose the decade resistor to cancel out the average thermistor resistance \bar{R}_t and essentially get more digits for the resistance change $\Delta R(t)$ that causes the bridge imbalance signal.

The thermal bath temperature T_b is measured by reading the voltage drop across a Platinum Resistance Thermometer (PRT) attached to the copper block. The PRT is model 146MA1000F from Rosemount, which is calibrated against the IPTS-1968 standard. The PRT resistance is not measured directly with the resistance mode of the multimeter since the

meter would send a current through the PRT during the measurement. This current would heat up the PRT. Instead, a small constant current (from a home-made source) is sent through the PRT and a standard resistor in series with it, and the voltage drops across both are measured. This avoids transient self-heating effects in the PRT and allows an accurate determination of bath temperature. To avoid thermal emf effects, two measurements are made with reversed currents, and the value of the PRT resistance is taken to be the average of these two readings.

D. Computer Control

Data acquisition is achieved with software written in Turbo C++ under DOS on the 486SX/25 Dell computer. A schematic block diagram of calorimeter B is shown in Fig. 2-10. The essential features of its operation are summarized below.

1. To get the bath temperature, one can measure the PRT resistance as described in the previous section.
2. To control the bath temperature scan rate, one can program the computer to vary the decade resistance in bridge 1.
3. To get the sample cell temperature, one can measure the imbalance signal of bridge 0 by reading the Ithaco lock-in through the HP meter. The resistance of the thermistor is calculated by measuring the driving voltage on the bridge and the imbalance signal.

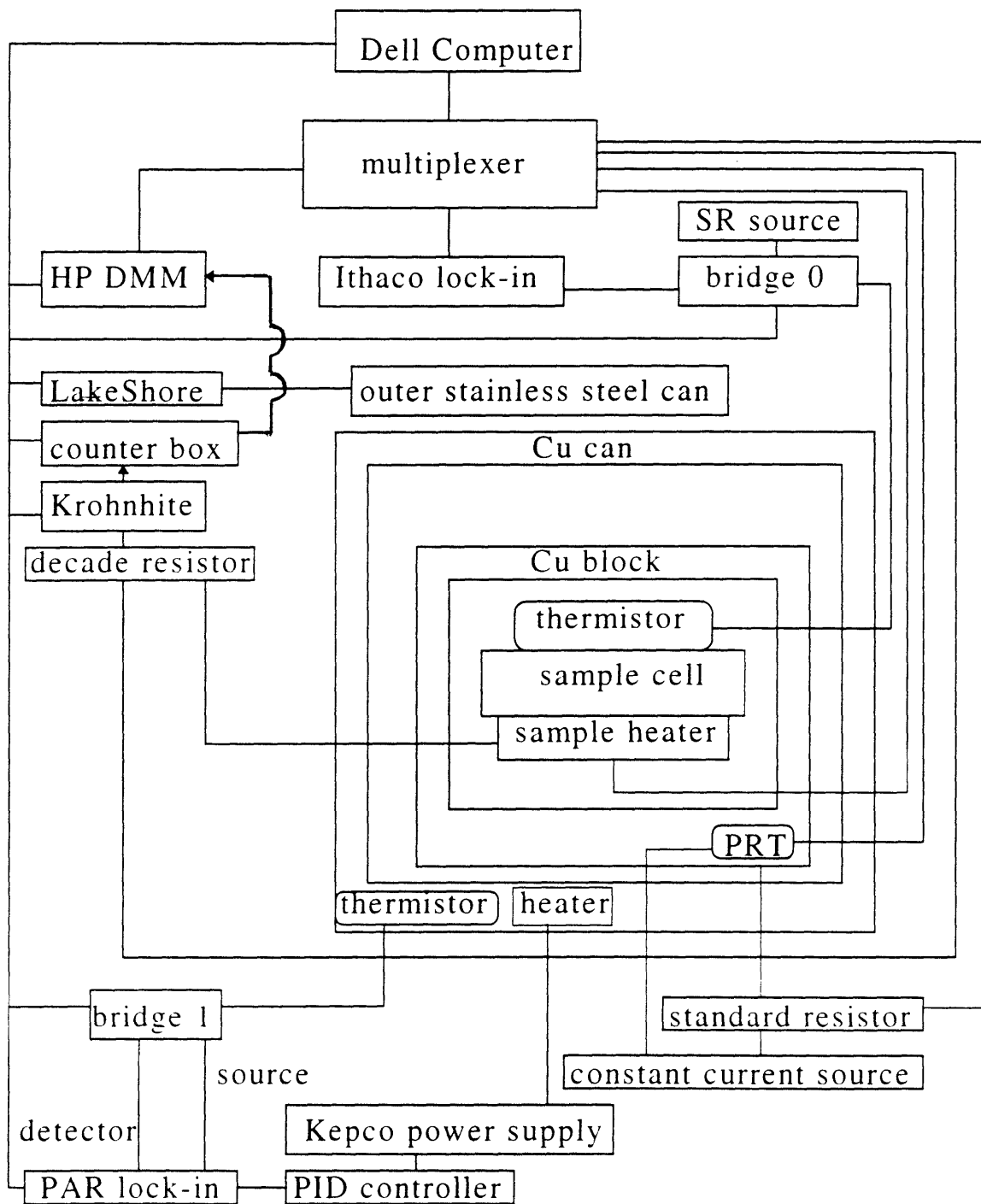


Fig. 2-10. Block diagram of Calorimeter B

4. At the beginning of a data point measurement, the computer resets the counting circuit to the state where it will not produce TTL pulses until it detects a TTL pulse from the ARB-Z output of the Krohnkite. The reset pulse is provided by the DIO board inside the computer. The computer reads the output from the counting circuit to the DIO board. When a TTL pulse is received, it commands the HP meter to read bridge 0. Each reading (say every 0.5 s) is triggered by detecting the high to low transitions of the TTL train coming into the DIO board.

E. AC mode of operation

For the ac mode, calorimeter B operates in exactly the same way as calorimeter A. The user needs to set the amplitude and frequency of the ac heater power, measures this heater power, determines the bath temperature T_b , and monitors the variation $T(t)$ in the sample temperature. See Sec. 2.5D for details. The final result is the determination of ΔT_{ac} and the phase shift ϕ , which allow C_p^{sys} to be calculated with Eq. (2.17): $C_p^{sys} = (P_0/\omega\Delta T_{ac})\cos\phi$.

F. Relaxation Mode of Operation

1. Heating Runs

First, the bath and sample are equilibrated at the desired starting temperature with the heater power set at zero. The bath temperature is measured with the PRT, and then the thermistor temperature $T(t)$ is monitored while the heater power is turned

on either as a step function or a linear function of time. In the case of the linear power mode, the heating power variation is

$$\begin{aligned} P &= 0 && \text{for } t = 0 \\ P &= \dot{P}_1 t && \text{for } 0 < t < t_1 \\ P &= \dot{P}_1 t_1 = P_0 && \text{for } t \geq t_1 \end{aligned}$$

where \dot{P}_1 is a constant and t_1 is about 500 seconds. Then one waits for about 500 seconds more so that the sample reaches a constant final temperature $T(\infty) = T_b + P_0 R > T_b$ as measured by the thermistor. After that, the power is ramped linearly down to zero at the rate $-\dot{P}_1$. The thermistor resistance values collected during the heating and cooling cycle are stored in the computer. Heat capacity values are obtained with Eq. (2.7)

$$C_p^{sys}(T) = \frac{P - \frac{T - T_b}{R}}{dT/dt},$$

where the thermal resistance R has been

obtained from Eq.(2.32) using T_b and $T(\infty)$ as T_1 and T_2 . The entire process is repeated with the bath temperature raised to a higher value. Note that we record all the thermistor readings in the computer memory and process the data after the entire experiment.

2. Cooling Runs

A constant power P_0 is applied to the sample heater, and one waits for bath and sample equilibration. Then the initial sample temperature $T_b + P_0 R$ and the bath temperature T_b are

measured. The sample temperature $T(t)$ is monitored while the heater power is decreased linearly to zero at the rate $-\dot{P}_1$:

$$P = P_0 \quad \text{for } t \leq 0$$

$$P = P_0 - |\dot{P}_1|t \quad \text{for } 0 < t < t_1$$

$$P = 0 \quad \text{for } t \geq t_1 = P_0/|\dot{P}_1|$$

After a further period of about 500 seconds, the sample should reach bath temperature. Then the power is increased linearly to P_0 at the rate \dot{P}_1 . After recording the data for this cooling and heating cycle, the heat capacity values are again obtained with Eq. (2.7). The entire process is repeated with the bath temperature changed to a lower value.

References

1. J. Thoen, E. Bloemen, and W. Van Dael, *J. Chem. Phys.* 68, 735 (1978).
2. Y.A. Kraftmaker, *Zh. Prikl. Mech. & Tekh. Fiz.* 5, 176 (1962).
3. P. F. Sullivan and G. Seidel, *Phys. Rev.* 173, 679 (1968).
4. C.A. Schantz and D.L. Johnson, *Phys. Rev. A* 17, 1504 (1978).
5. J. M. Viner, D. Lamey, C.C. Huang, R. Pindak, and J.W. Goodby, *Phys. Rev. A* 28, 2433 (1983).
6. G.B. Kasting, K.J. Lushington, and C.W. Garland, *Phys. Rev. B* 22, 321 (1980); C. W. Garland, *Thermochim. Acta* 88, 127 (1985) and references cited therein.
7. K.J. Lushington, G.B. Kasting, and C.W. Garland, *J. Phys. Lett. (Paris)*, 41, L419 (1980).
8. K. Ema, G. Nounesis, C. W. Garland, and R. Shashidhar, *Phys. Rev. A* 39, 2599 (1989).
9. K.J. Stine and C.W. Garland, *Mol. Cryst. Liq. Cryst.* 188, 91 (1990).
10. R. Bachmann, F.J. DiSalvo, Jr., T.H. Geballe, R.L. Greene, R.E. Howard, C.N. King, H.C. Kirsch, K.N. Lee, R.E. Schwall, H.-U. Thomas and R.B. Zubeck, *Rev. Sci. Instrum.* 43, 205 (1972); D. Djurek, J. Baturic-Rubcic, and K. Franulovic, *Phys. Rev. Lett.* 33, 1126 (1974).

- 11.K. Ema, T. Uematsu, A. Sugata and H. Yao, Jpn. J. Appl. Phys. 32, 1846 (1993); H. Yao, H. Nagano, Y. Kawase, and K. Ema, Biochim. Biophys. Acta 1212, 73 (1994).
- 12.K. Stine, Ph.D. Thesis in Chemistry (MIT), (1988).

Chapter 3

Phase Transitions In Ferroelectric Liquid Crystals

3.1 Ordering In Smectic-C

and Smectic-C* Phases

The simplest model for SmA and SmC phases are orientationally ordered fluids with one-dimensional mass density waves. The direction of the density wave, i.e., the normal to the smectic layers, is along (in SmA) or tilted (in SmC) with respect to the unique orientation axis \bar{n} called the director. It was de Gennes¹ who first suggested in 1973 that SmA—SmC transitions should be in the universality class of superfluid helium (3D-XY model). The SmC order parameter ψ has two components:

$$\psi = \theta \exp(i\phi), \quad (3.1)$$

where θ is the tilt angle of the director relative to the mass density wave direction and ϕ is the azimuthal angle. In the SmC phase, θ is non-zero and constant in space if one can ignore

thermal fluctuations, which is justified by the experimentally observed mean-field behavior. The azimuthal angle ϕ differs in different domains that usually have random spatial orientation.

Non-chiral liquid crystals (where the molecule and its mirror image are the same) can exhibit a SmC phase, whereas chiral liquid crystals (the molecule has an optically active center and is different from its mirror image) form a new phase called smectic-C* (SmC*). This phase is very similar to SmC, but the azimuthal angle ϕ has a regular helicoidal variation along the mass density wave direction (see Sec. 1.3).

3.2 Landau Model for SmA—SmC

and SmA—SmC* Transitions

A. SmA—SmC Transition

All SmA—SmC transitions in non-polar systems are found empirically to be second order. It has been well established² that these SmA to SmC transitions are described by the so-called extended Landau model, which is discussed in Chapter 1 of this thesis as **Model 2**. This Landau behavior is explained by the Ginzburg criterion, which predicts that the critical fluctuation region is too small to observe experimentally³ for SmA—SmC transitions.

For **Model 2**, we have from Sec. 1.5B

$$L(P) = aP^2 + bP^4 + cP^6 \quad (3.2)$$

$$G = G_0 + \text{minimum of } L(P), \quad (3.3)$$

where G_0 is a temperature-dependent but slowly varying “background” free energy that describes the behavior in the absence of SmC tilting, $P = |\psi| = \theta$, and

$$t = (T - T_0)/T_0 \quad (3.4)$$

is the reduced temperature. The parameters $a > 0$, b , $c > 0$ and T_0 are constants independent of temperature T . This simple model is appropriate since there is symmetry with respect to θ [$G(\theta) = G(-\theta)$] and the free energy is independent of the azimuthal angle ϕ (at least for achiral, nonpolar compounds).⁴

The essential features of this model are summarized below.

When $b > 0$, a second-order transition occurs at T_0 . The heat capacity at constant pressure p is given by

$$C_p = C_p^0 \quad \text{for } T > T_0 \quad (3.5a)$$

$$C_p = C_p^0 + A \frac{T}{T_0} \sqrt{\frac{T_k - T_0}{T_k - T}} \quad \text{for } T < T_0 \quad (3.5b)$$

where C_p^0 is the heat capacity of the SmA phase given by $C_p^0 = -T(\partial^2 G_0 / \partial T^2)_p$, and this quantity is usually a smooth (linear) function of T and p .

- $A = \left| \frac{a^2}{2bT_0} \right|$ is the heat capacity jump at T_0 .

- T_k is the metastability limit given by

$$T_k = T_0 + \frac{b^2 T_0}{3ac} \quad (3.6)$$

When $b < 0$, a first-order transition occurs at $T_1 > T_0$. The heat capacity has the same form as before:

$$C_p = C_p^0 \quad \text{for } T > T_1 \quad (3.7a)$$

$$C_p = C_p^0 + A \frac{T}{T_0} \sqrt{\frac{T_k - T_0}{T_k - T}} = C_p^0 + 2A \frac{T}{T_0} \sqrt{\frac{T_k - T_1}{T_k - T}} \quad \text{for } T < T_1 \quad (3.7b)$$

$$\text{where } T_1 = T_0 + \frac{b^2 T_0}{4ac} = T_k - \frac{b^2 T_0}{12ac} \quad (3.8)$$

In this case, the jump in C_p at T_1 is $2A$.

When $b = 0$, the transition is tricritical and occurs at $T_k = T_0 = T_1$:

$$C_p = C_p^0 \quad \text{for } T > T_k \quad (3.9a)$$

$$C_p = C_p^0 + \sqrt{\frac{a^3}{12cT_0}} \left(\frac{T}{T_0} \right) \frac{1}{\sqrt{T_k - T}} \quad \text{for } T < T_k \quad (3.9b)$$

Thus Landau theory predicts that C_p diverges with the tricritical exponent $\alpha = 0.5$ on approaching T_k from below. Note that the quantity T/T_0 in Eqs. (3.5b), (3.7b), and (3.9b) can in practice be set to equal to unity since it varies only from 0.97 to 1.0 when T varies from $T_0 - 10\text{K}$ to T_0 .

From Eq. (1.9) it follows that the tilt angle θ is given by

$$\theta = \sqrt{-\frac{b}{3c} + \sqrt{\left(\frac{b}{3c}\right)^2 - \frac{at}{3c}}} \quad (3.10)$$

below the transition. In the region where $\left(\frac{b}{3c}\right)^2 \ll \frac{at}{3c}$, i.e., b is

close to zero (system is close to the tricritical point), the tilt angle scales like a power law: $\theta \propto (-t)^{\beta_{tc}}$ with the tricritical exponent $\beta_{tc} = 1/4$. In the other limit where $\left(\frac{b}{3c}\right)^2 \gg \frac{at}{3c}$, i.e., b is large (system is far away from the tricritical point), the tilt angle scales with another power law: $\theta \propto (-t)^{\beta_{MF}}$ with mean field exponent $\beta_{MF} = 1/2$. When $b < 0$, there is a discontinuous jump in θ from zero to $-b/2c$ at the first-order transition temperature T_1 . Experimentally, one has a finite temperature resolution, so it is very hard to distinguish $\theta(T)$ behavior for small $b > 0$, $b = 0$, and small $b < 0$.

A useful dimensionless quantity to characterize the sharpness of the ΔC_p peak and thus indicate how close the system is to the tricritical point is

$$t_0 \equiv b^2/ac \quad (3.11)$$

It is clear that $t_0 = 0$ at the tricritical point where $b = 0$, and t_0 has been found to be a small number for many samples. From Eqs. (3.6) and (3.8), the following relations hold:

$$T_k = T_0(1 + t_0/3) \quad T_1 = T_0(1 + t_0/4)$$

For a second-order transition, t_0 is given by

$$t_0 = \frac{3(T_k - T_0)}{T_0} \quad (3.12)$$

From Eq. (3.5b), heat capacity can be written as

$$\Delta C_p = C_p - C_p^0 = A(1+t) \frac{1}{\sqrt{1-3\frac{t}{t_0}}} \approx A \left(1-3\frac{t}{t_0}\right)^{-1/2} \quad \text{for } T < T_0$$

It follows that

$$\Delta C_p(t=0) = A, \quad \Delta C_p(t=-t_0) = (1-t_0) \frac{A}{2} \approx \frac{A}{2}$$

So for a second-order transition, t_0 is the full width at half maximum for ΔC_p in reduced temperature units.

For a first-order transition, t_0 is given by

$$t_0 = \frac{12(T_k - T_1)}{T_0} \approx \frac{12(T_k - T_1)}{T_1} \quad (3.13)$$

From Eq. (3.7b), the heat capacity jump at the transition is

$$\Delta C_p(t_1) = A(1+t_1) \frac{1}{\sqrt{1-3\frac{t_1}{t_0}}} = \left(1 + \frac{t_0}{4}\right) 2A \approx 2A,$$

where $t_1 = \frac{T_1 - T_0}{T_0} = \frac{t_0}{4}$. It is still true that

$$\Delta C_p(t=0) = A, \quad \Delta C_p(t=-t_0) = (1-t_0) \frac{A}{2} \approx \frac{A}{2};$$

thus the heat capacity drops to a quarter of its maximum value when $t = -t_0$. This point occurs when $T - T_1 = -5t_0 T_0/4 \approx -5t_0 T_1/4$.

Almost all previous experimental data on SmA–SmC transitions have been analyzed using the Landau model described above. It is interesting to note that although all nonpolar SmA–SmC transitions have been found to be second order, **Model 2** predicts crossover from second-order to first-order behavior as the coefficient of the fourth order term b changes from positive to negative via a tricritical point at $b=0$. Since the parameter

$t_0 = b^2/ac$ has been found to be very small in several experiments on achiral compounds, it is possible that such nonpolar SmA—SmC transitions are naturally close to some tricritical points (like the NAC point⁵).

B. SmA—SmC* Transition

Since the structure of smectic-C* is very similar to that of smectic-C except for the helical modulation of the tilt direction (and the energy associated with unwinding the helix is very small^{4,6}), one would expect the same Landau theory to be applicable to smectic-A—smectic-C* transitions at least for low chirality.⁴

Experimentally, first-order SmA—SmC* transitions have been observed as well as second order. Thus it is possible to study tricritical behavior in appropriate mixtures. In the first such system that was studied,⁷ a puzzling behavior was observed near the SmA—SmC* tricritical point. In that experiment, the specific heat peak was rounded and there was an excess $C_p > C_p^0$ for temperatures above the transition, as shown in Fig. 3-1. At the time it was suggested that thermal fluctuations might be the reason for this non-Landau behavior near the tricritical point. Another possibility is the coupling between the spontaneous polarization P and the tilt θ that is present in more general mean-field models.⁴ Since P is a secondary order parameter with a different temperature dependence than θ , this will affect C_p . Indeed such

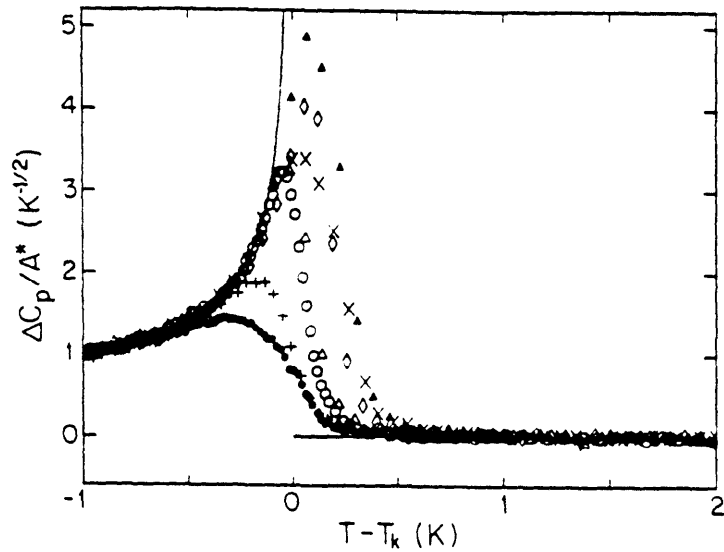


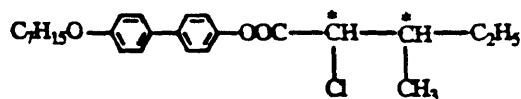
Fig. 3-1. Excess heat capacity ΔC_p (SmA-SmC^{*}) for mixtures of 2f+3f. $A^* \equiv \sqrt{a^3/12cT_0}$; see Eqs. (3.9) and (3.14). The solid line represents the theoretical Landau curve $(T_k - T)^{-1/2}$, which represents the data very well for $-10\text{K} \leq T - T_k \leq -0.5\text{K}$. This detailed view showing deviations from the Landau model is taken from Ref. 7. Note that the data are rounded in the transition region for the range of $|T - T_k| \leq 200\sim 500$ mK.

effects on C_p will be largest when the spontaneous polarization is large and strongly coupled to θ , which is the case for the system studied in Ref. 7. The present work was undertaken to resolve the situation and establish SmA—Sm C^* behavior in mixtures of weak chirality and small spontaneous polarization.

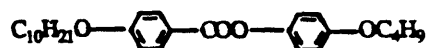
3.3 Experiment

A systematic series of heat capacity measurements have been carried out on mixtures of chiral C7 (methylchlopentanoyloxy heptyloxybiphenyl) and non-chiral 10O4 (butyloxyphenyl decyloxybenzoate):

C7 (MW = 416.99)



10O4 (MW = 426.59)



These materials were synthesized by Bahr and Heppke⁸ at the Technical University of Berlin. They have shown⁹ that the SmA to Sm C^* transition crosses over from first order in C7 to second order in mixtures via a tricritical point at $X \approx 10.5$, where X is the mole percent of 10O4. The highest spontaneous polarization in the Sm C^* phase is 290 nC/cm² for C7 and 100 nC/cm² for the tricritical mixture.⁹ A partial phase diagram is shown in Fig 3-2.

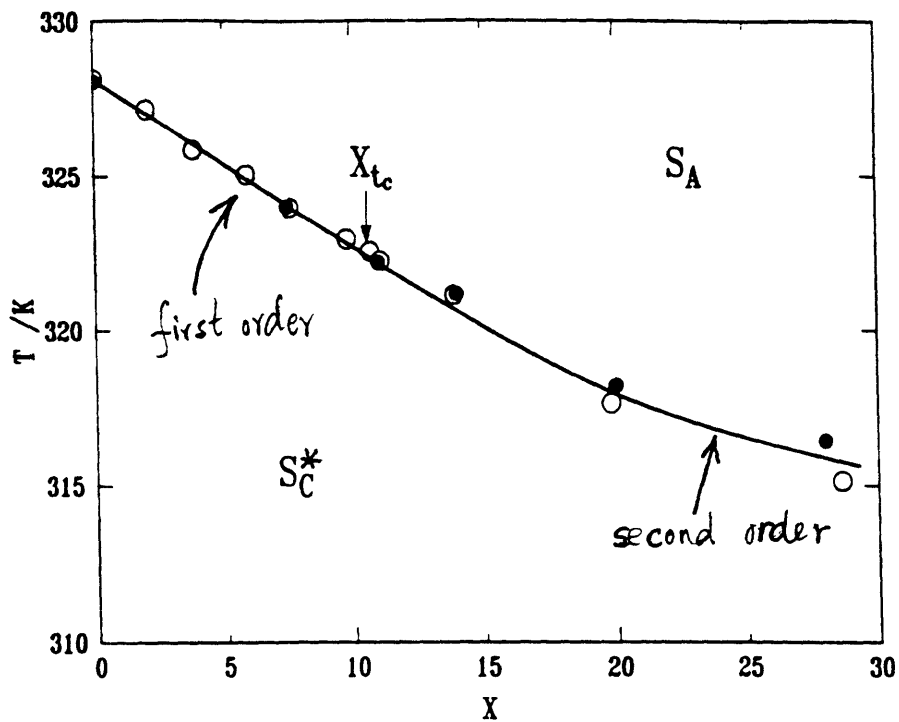


Fig. 3-2. Partial phase diagram for $C7+\overline{10O4}$ mixtures with transition temperatures determined microscopically (\circ) and calorimetric transition temperatures (\bullet). X is the mole per cent $10O4$. The tricritical point is indicated at $X_{tc}=10.6$.

The calorimeter used to study the $C7+\overline{10O4}$ system was calorimeter A (without the recent improvements by Dr. H. Yao and the author). Pure $C7$ (the L enantiomer) and five $C7+\overline{10O4}$

mixtures with composition $X=7.5, 11.1, 14.0, 19.7,$ and 28.0 were investigated. The stability of these samples was good; the drift in transition temperatures observed during successive heating and cooling runs was in the range of -10 to -40 mK per day. Furthermore, the calorimetric transition temperatures are in good agreement with those determined optically. It is necessary to stress that an ac calorimeter measures heat capacity values but not the enthalpy. Thus any latent heat at a first-order transition is not measurable with calorimeter A.

As mentioned previously, the trivial temperature dependence of the term T/T_0 in C_p can be neglected and equations (3.5b), (3.7b), and (3.9b) can be rewritten in the convenient form

$$\Delta C_p = C_p - C_p^0 = A^*(T_k - T)^{-1/2} \quad \text{for } T < T_{\text{trans}} \quad (3.14)$$

where $A^* = \sqrt{a^3/12cT_0}$. The “background” heat capacity C_p^0 can be well represented by $C_p^0 = B + E(T - T_0)$, where B and E are constants.

In ac calorimetry, one identifies phase transitions by observing singularities in heat capacity data. Although the Landau model predicts a discontinuous jump in heat capacity at phase transitions, our experimental C_p data, like all SmA-SmC data,¹⁰ have a sharp peak at the transition. The peak is very asymmetric (see Fig. 3-3): the high-temperature side is a steep, almost vertical ramp covering about 100 mK, while the low-temperature side decays smoothly and extends to about 10 K below the peak. These features allow us to use the Landau model to describe the data if we omit the data points in region of the near-vertical ramp.

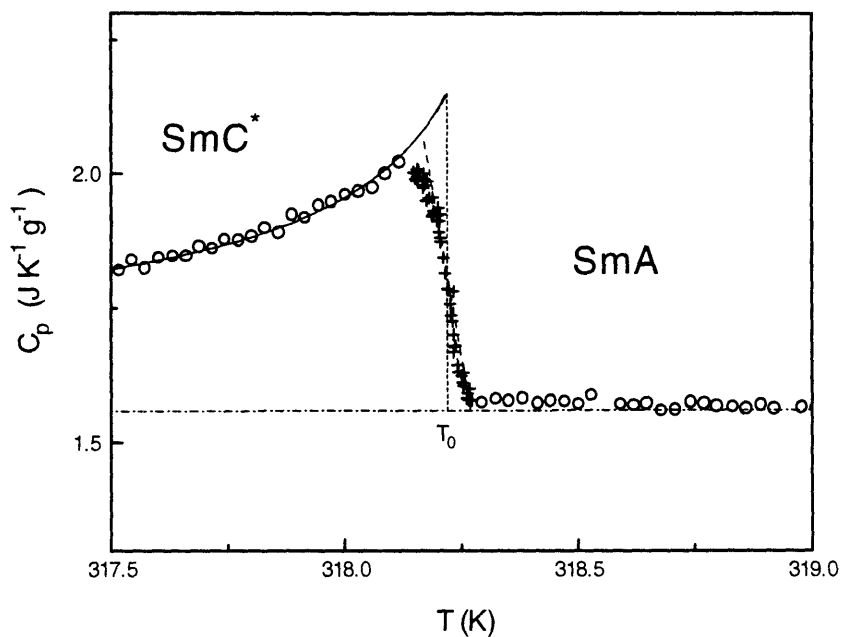


Fig. 3-3. Detailed view of C_p data near the second-order transition for the $C7+\overline{10O4}$ mixture with $X=19.6$. The vertical dashed line indicates our choice of T_0 , and the horizontal dash-dot line representing C_p^0 was obtained from fitting with Eq. (3.14) C_p data in the SmA phase over a range of several degrees. Data omitted from the fit are represented by '+' signs. Note the steep linear ramp (long dashes) over ~ 83 mK, i.e., $|T-T_0| \leq 42$ mK, which is typical of the behavior observed in nonpolar SmA-SmC data.¹⁰

A. Second-Order Transitions

For second-order transitions, we choose T_0 to be the midpoint of the very steep, near-linear C_p variation at the transition. This choice has been used previously by our group¹⁰ and by Huang¹¹ for SmA-SmC transitions. An example is shown in Fig. 3-3. Note that Eq. (3.14) does not depend on T_0 explicitly, therefore fitting ΔC_p data is not sensitive to the choice of T_0 . The only constraint for the choice of T_0 is $T_0 < T_k$. It turns out that our fitting parameter T_k is always larger than the T_0 value obtained by the above method. Although the “true” transition temperature may well be in the region of the rounded peak below the dashed line, our choice of mean-field transition temperature T_0 is reasonable, because the mean-field transition temperature T_0 should be higher than the “true” transition temperature if fluctuation effects (which Landau theory ignores) play any role. The fits of our experimental data with Eq.(3.14) are excellent. Examples are given in Fig. 3-3 over a limited temperature range and in Fig. 3-4, which shows data for the near tricritical mixture. In the fitting, we omitted data points in the region of the near-vertical ramp around T_0 . In Fig 3-4, the fit with equation (3.14) to the C_p data for X=11.1 is shown over a 10K temperature range. In this sample, it is not possible to distinguish whether the transition occurs at T_k or just below T_k , but in any case the system is very close to tricritical.

No anomalous increase in phase shift or any other feature associated with a first-order transition was observed for the X=11.1 sample.

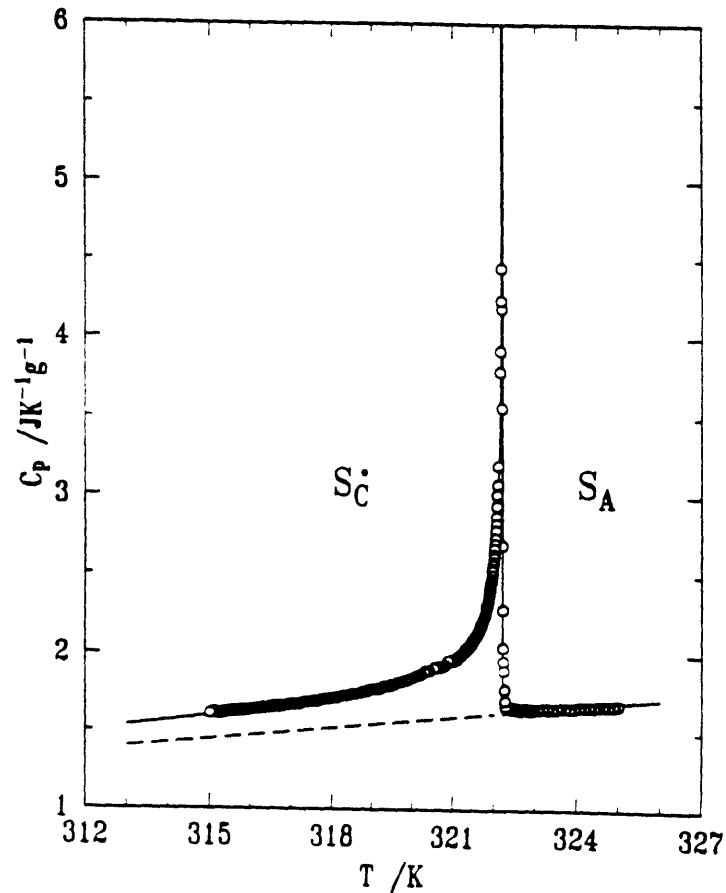


Fig. 3-4. Specific heat capacity in a near tricritical $C7+\overline{10O4}$ mixture with $X=11.1$. The solid curve represents a Landau fit with Eq. (3.14), and the dashed line represents the background heat capacity $C_p^0(T)$. This is the best example known of C_p data near a mean-field Landau tricritical point.

B. First-Order Transitions

Recall that we have some qualitative methods to characterize a first-order transition in ac calorimetry. If the latent heat is large enough (like most melting transitions), one could observe its effects on the sample temperature. In the ac mode, the thermal bath temperature T_b is scanned linearly with time. Recall (Sec. 2.3A) that the average sample temperature is $\bar{T} = T_b + P_0 R - \dot{T}_b \tau_{\text{ext}}$ outside a first-order transition region, but it will deviate from this value if there is two-phase coexistence. The sinusoidal sample temperature oscillation $\Delta T_{\text{ac}}(t)$ can also be distorted by two-phase coexistence, if the rate of phase conversion is fast enough compared to the ac period. (In our experiment, the period of temperature oscillation is 32 seconds, and one data point requires measurement over 6 periods of such oscillations.) However, if the phase conversion and latent heat release is slow enough, its effects show up as an effective bath temperature as explained in Chapter 2. When the system releases latent heat (on a cooling run, like in crystallization), the average sample temperature will be anomalously higher than the expected value \bar{T} ; if the system absorbs latent heat (on a heating run, like in melting), the average sample temperature will be anomalously lower than the expected value \bar{T} . When a first-order latent heat is very small, its effects may not show up in the sample temperature (our machine has finite resolution). But we can use another useful qualitative indication of two-phase coexistence that occurs at a first-order

transition. Data taken in a two-phase coexistence region exhibit anomalously high C_p values and an abrupt increase in the phase shift ϕ between the oscillating heat input and the sample temperature, as described in Sec. 2.3B. All of these techniques have been applied to our data analysis

These characteristics of first-order phase coexistence were clearly observed for $X=0$ and $X=7.5$, and the widths of the coexistence ranges were 150 mK and 120 mK respectively. The C_p and phase shift data for pure C7 is shown in Fig. 3-5. One can clearly see the four anomalously large C_p values and the abrupt increase of the phase shift in the two-phase coexistence region. For first-order transitions, the T_1 value was taken to be the midpoint of the two-phase coexistence range; note that Eq. (3.14) does not depend on T_1 explicitly, therefore the fitting is not sensitive to the choice of T_1 . In fitting the data, we omitted any anomalous points taken in the coexistence region for the two samples with $X=0$ and $X=7.5$. The values of the fitting parameters A^* , B , E , T_k are listed in Table 3-1, together with the T_1 and T_0 values which are the transition temperatures, and t_0 and A ($\Delta C_p(\mathbf{max})$) values given by $A = \Delta C_p(\mathbf{max}) = A^*(T_k - T_0)^{-1/2}$ for a second-order transition and $A^*(T_k - T_1)^{1/2}$ for a first-order transition.

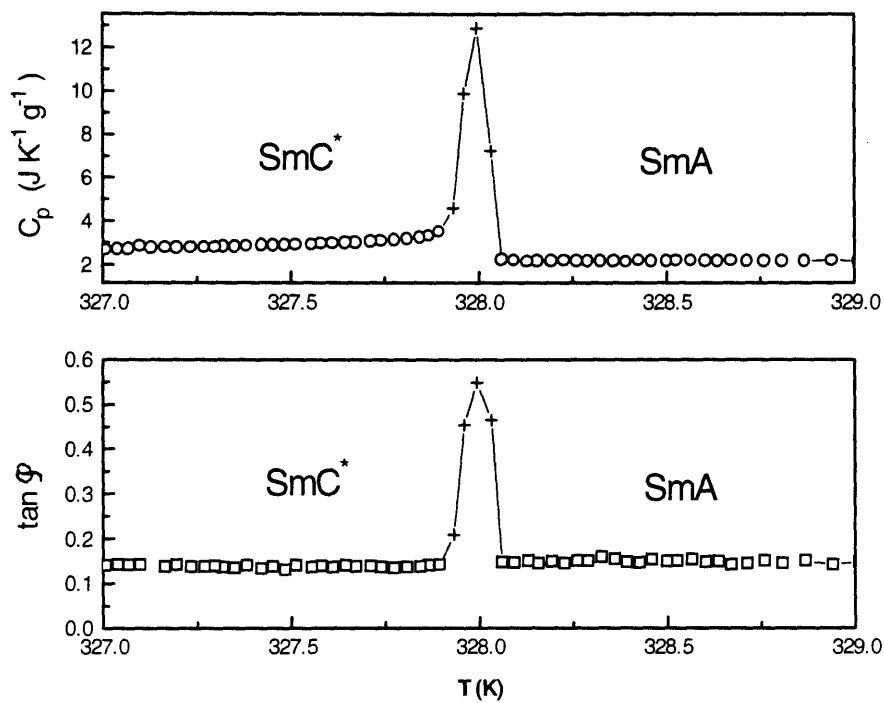


Fig. 3-5. C_p and phase shift data for pure C7 close to the SmA-SmC* transition. The anomalous points (denoted by '+' signs) are in the two-phase coexistence region. This is a classic example of ac calorimetry data for a system undergoing a first-order transition.

Table 3-1. Least-squares values of the Landau parameters in equations (3.5)-(3.9) and (3.14) obtained on fitting SmA-SmC* heat capacity data for C7+ $\overline{10O4}$ mixtures. X is the mole percent $\overline{10O4}$. The background quantity $C_p^0(T)$ is given by $B+E(T-T_0)$. The units are $\text{JK}^{-1}\text{g}^{-1}$ for A and B, $\text{JK}^{-2}\text{g}^{-1}$ for E, $\text{JK}^{-1/2}\text{g}^{-1}$ for A^* , and K for T_k and T_0 (T_1). The quantity $t_0 \equiv b^2/ac$ is dimensionless. For first-order transitions when $X \leq 10$, T_1 values are given in place of T_0 .

X	$T_0(T_1)$	T_k	A	A^*	B	$10^3 E$	χ^2	$10^4 t_0$
0	(328.064)	328.141	0.94	0.52	1.26	16.0	1.19	28.2
7.5	(323.986)	323.991	3.37	0.48	1.20	17.7	1.24	1.9
11.1	322.198	322.200	9.37	0.42	1.62	24.1	0.93	0.2
14.0	321.185	321.213	2.21	0.37	1.51	12.0	1.04	2.6
19.7	318.221	318.400	0.60	0.25	1.56	1.8	0.88	16.9
28.0	316.439	316.787	0.30	0.18	1.45	7.5	0.91	33.0

C. Scaling Plots

A scaling plot of $\Delta C_p/A^*$ versus $T-T_k$ is given in Fig. 3-6 for three of the six samples. The solid line represents the theoretical Landau value: $(T_k - T)^{-1/2}$ below the transition and zero above. The data for the other three samples also agree very well with the Landau curve.

3.4 Discussion

In Chapter 1 we mentioned that the modern theory of phase transitions is the renormalization group (RG) theory. The lowest order approximation to the RG theory is the Landau (mean field) theory of phase transitions. Experimentally, if a certain macroscopic property of a system exhibits a very asymmetric singularity at the phase transition like the C_p data presented in this chapter, one could argue that the critical fluctuation effects are small in the experimentally accessible region. In this case, the fluctuation effects only dominates in an experimentally inaccessible small region very close to the transition. In our ac calorimeter, the C_p data were obtained by applying an ac power to the sample and measuring its sinusoidal temperature response.

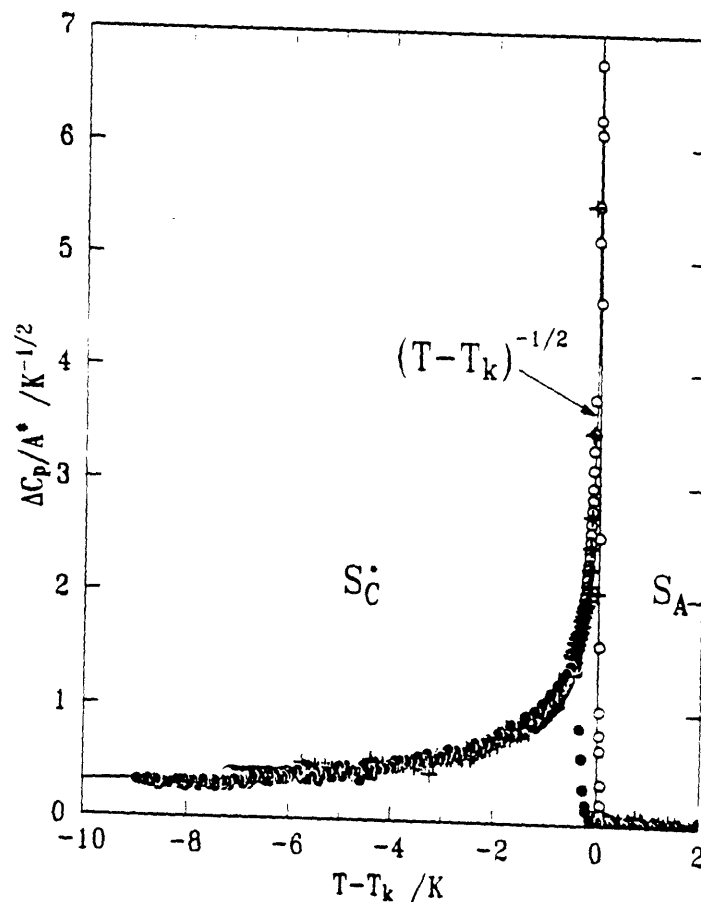


Fig. 3-6. Landau scaling plots of the excess heat capacity ΔC_p associated with the SmA-SmC* transition in three C7+ $\overline{10O4}$ mixtures: X=0 (+), 11.1 (o), and 28.0 (●). The A* and T_k values are given in Table 3-1.

Since our machine has a finite temperature resolution, we have set the amplitude for the sample temperature oscillation to be about 5 mK. Thus, we cannot resolve any data within the region of $T_c \pm 5$ mK, where T_c is the transition temperature. Furthermore, sample impurity could smear out the transition and the data around T_c could be rounded. It is very common that mixtures show more rounding than pure compounds. Our C_p data for the SmA–SmC* transition exhibit a narrow (about 100 mK), almost vertical ramp above the transition. This ramp could possibly be due to fluctuation effects, but it is not a good practice to fit the data in such a narrow region to get any functional form, considering the temperature resolution and the rounding effects. In contrast to SmA–SmC and SmA–SmC* data, the C_p data for smectic-A to nematic transitions clearly show fluctuation effects (excess C_p wings on both sides of the transition) in a region as large as ± 5 K.¹² In this case, the Landau model is not applicable and RG theory must be used to fit the data.

The results given in Sec.3.3 unambiguously demonstrate the Landau behavior of ΔC_p near a SmA—SmC* transition. Indeed, C7+10O4 mixtures provide a classic example of such behavior. We plot b/\sqrt{ac} against X in Fig. 3-7; the linear fit gives for the tricritical composition $X_{tc}=10.6\pm 0.4$, which agrees well with electro-optic experiments by Bahr and Heppke.⁹ In their work, tilt angle and polarization measurements were made on the C7+10.O.4

system. They identify a first-order transition by observing a discontinuous jump in the tilt angle or the polarization and associated hysteresis effects. They compared their results with the predictions of the Landau theory, since no critical fluctuation effects were observed. Their experimental data also agree reasonably well with the Landau model but do not show the mean-field tricritical behavior as clearly as the present C_p data.

We can also explain the peculiar features observed previously by Boerio-Goates et al.⁷ as due to inhomogeneities in those samples. During the work on C7 and $\overline{1004}$ mixtures, I accidentally prepared an inhomogeneous sample due to inadequate mixing. The initial specific heat data showed a smeared and rounded peak at the transition. After thermal “annealing” in the isotropic phase (where diffusion is rapid), the SmA—SmC* transition peak sharpened and Landau behavior was recovered. If there are regions of different composition in a particular mixture sample, the transition temperature will be different for each region. A simple model¹³ is to assume a Gaussian distribution of transition temperatures T_0 about an average value \overline{T}_0 :

$$\Delta C_p = \int_T^{\infty} A^* (T_k - T)^{-1/2} g(T_0) dT_0 \quad (3.15)$$

$$\text{where } g(T_0) = \frac{1}{\sqrt{2\pi}\sigma} \exp\left(-\frac{(T - \overline{T}_0)^2}{2\sigma^2}\right) \quad (3.16)$$

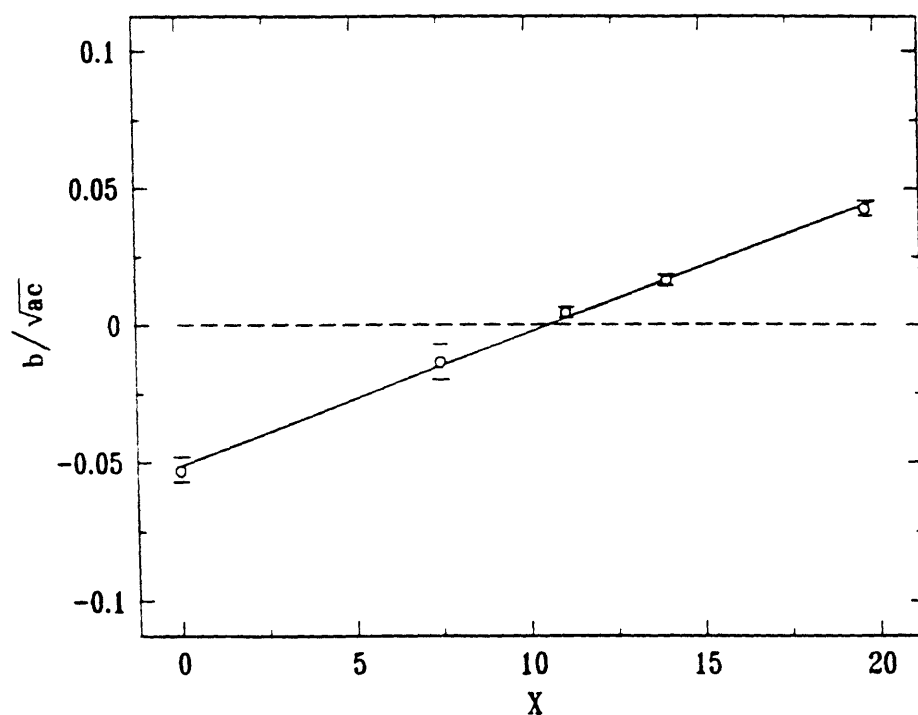


Fig. 3-7. Variation with composition near X_{tc} of the Landau coefficient ratio b/\sqrt{ac} derived from C_p fits. The error bars are 95 per cent confidence limits based on the least squares uncertainty in T_k and our estimated uncertainty in choosing T_0 and T_1 . The assumed linear dependence of b/\sqrt{ac} on X yields $X_{tc} = 10.6 \pm 0.4$.

Since $t_0 = b^2/ac$ depends on the concentration X , and the concentration has a distribution that results in the distribution of T_0 , we can expand t_0 around \bar{T}_0 :

$$t_0 = t_0(\bar{T}_0) + \left. \frac{\partial t_0}{\partial T_0} \right|_{T_0 = \bar{T}_0} (T_0 - \bar{T}_0) + \dots$$

Since the Gaussian distribution (3.16) is strongly peaked around \bar{T}_0 and the small number t_0 is a smooth function of X (and thus T_0), we can keep just the first term in this expansion, which has been justified by numerical calculations. Thus we have carried out the integration in Eq. (3.15) using

$$\Delta C_p \approx A^* \int_T^{\infty} (T_0 + \frac{t_0(\bar{T}_0)}{3} T_0 - T)^{-1/2} g(T_0) dT_0 \quad (3.17)$$

where changes in A^* have been ignored. For a second-order transition,

$$\frac{t_0(\bar{T}_0)}{3} = \frac{T_k(\bar{T}_0) - \bar{T}_0}{\bar{T}_0} = \frac{\bar{T}_k - \bar{T}_0}{\bar{T}_0} \quad (3.18)$$

We have taken A^* and \bar{T}_0 values from Ref. 7 and have used \bar{T}_k and σ as adjustable parameters. An example of the fitting is shown in Fig.3-8, where we have $\bar{T}_k = 393.96\text{K}$, $A^* = 0.1226$, $\bar{T}_k - \bar{T}_0 = 0.17\text{K}$ and $\sigma = 0.17\text{K}$. We conclude that except for this heterogeneity broadening, the results of Ref.7 are fully compatible with our present experimental results.

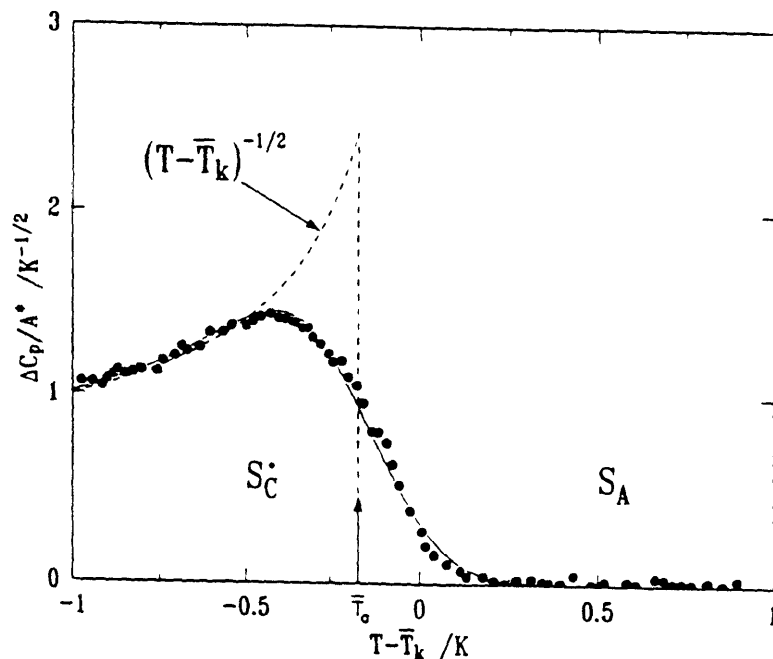


Fig. 3-8. Smearing effects of sample inhomogeneities in a $2f+3f$ sample [experimental data taken from Ref. 7]. The dashed lines represent the behavior in a homogeneous sample. The solid curve is obtained by simulation with Eq. (3.17).

So far all SmA-SmC and SmA-SmC* transitions have been found to be Landau mean-field like. However, a recent experiment by Prof. C. C. Huang's group seems to show fluctuation effects in C_p data for the SmA to SmC* transition of a newly synthesized liquid crystal.¹⁴ The high-temperature side of the C_p peak is above the background over a temperature range of about 1 K. It would

be interesting to find new materials that exhibit a wider temperature range of critical fluctuations at SmA-SmC* transitions. If this were possible, it would allow one to determine the critical exponent α for the heat capacity of this transition.

Even in the context of mean-field SmA to SmC* behavior, there are interesting predictions of unusual temperature dependencies for C_p , θ , and P in cases where strong coupling ($P\theta$ and $P^2\theta^2$ terms in the free energy) occurs.⁴ Such untraditional Landau results have been seen in $P(T)$ and $\theta(T)$ data⁴ but not yet in $C_p(T)$. A final subtlety of SmA to SmC* transitions is the issue of the Ginzburg criterion. Elastic constant measurements and sound attenuation data¹⁵ show critical fluctuation effects over a range of $0 < T - T_c < 10$ K for the SmA-SmC* transition in the liquid crystal TBBA, while the C_p measurements¹⁶ on the same compound show no sign of fluctuations (in agreement with the results reported in this chapter). It is proposed¹⁵ that the Ginzburg criterion is different for different physical properties. The calculations show that the critical fluctuation region for C_p is much smaller than that for elastic constants.

References

1. P.G. de Gennes, *Mol. Cryst. Liq. Cryst.* **21**, 49 (1973).
2. R.J. Birgeneau, C.W. Garland, A.R. Kortan and J.D. Litster, M. Meichle, B.M. Ocko, C. Rosenblatt, L.J. Yu, J. Goodby, *Phys. Rev. A* **27**, 1251 (1983).
3. C. R. Safinya, M. Kaplan, J. Als-Nielsen, R.J. Birgeneau, D. Davidov, J. D. Litster, D. L. Johnson, and M. Neubert, *Phys. Rev. B* **21**, 4149 (1980).
4. T. Carlsson, B. Zeks, C. Filipic, A. Levstik, and R. Blinc, *Mol. Cryst. Liq. Cryst.* **163**, 11 (1988).
5. C.W. Garland and M.E. Huster, *Phys. Rev. A* **35**, 2365 (1987).
6. S.Chandrasekhar, "Liquid Crystals", 2nd ed, Cambridge University Press, Cambridge, 1992.
7. J. Boerio-Goates, C.W. Garland, R. Shashidhar, *Phys. Rev. A* **41**, 3192 (1990).
8. Ch. Bahr and G. Heppke, *Molec. Cryst. Liq. Cryst. Lett.* **4**, 31 (1986).
9. Ch. Bahr, G. Heppke, *Physica A* **174**, 139 (1991).
10. M. Meichle and C.W. Garland, *Phys. Rev. A* **27**, 2624 (1983).
11. C.C. Huang and J.M. Viner, *Phys. Rev. A*, **25**, 3385 (1982).
12. C.W. Garland, G. Nounesis, and K. Stine, *Phys. Rev. A* **39**, 4919 (1989); G. Nounesis, C.W. Garland, and R. Shashidhar, *Phys. Rev. A* **43**, 1849 (1991).
13. K. J. Lushington and C.W. Garland, *J. Chem. Phys.* **72**, 5752 (1980).

14. C.C. Huang, private communication.
15. D. Collin, J.L. Gallani and P. Martinoty, *Phys. Rev. Lett.* 61, 102 (1988).
16. P. Das, K. Ema and C.W. Garland, *Liquid Cryst.* 4, 205 (1989).

Chapter 4

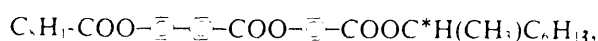
Antiferroelectric Liquid Crystals

4.1 Structures and Transitions

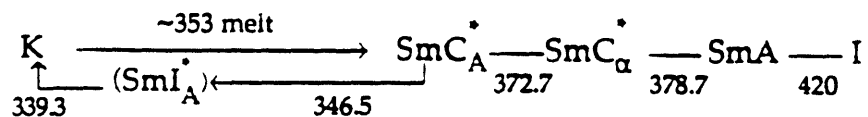
Chirality can induce various kinds of helical twist into the structure of liquid crystals [see Chapters 1, 3 and 5]. The N^* and SmC^* phases are the simplest examples of such effects. Chirality also makes it possible for SmC^* to be ferroelectric, thus the SmC^* phase has interesting electro-optical properties that have wide technical applications. Inspired by the importance of ferroelectric liquid crystals, organic chemists have since 1988 synthesized new chiral liquid crystals that exhibit antiferroelectricity in tilted smectic phase denoted as SmC_A^* .¹ Recall that in the ferroelectric SmC^* phase the polarizations of successive smectic layers form a helical structure, as shown in Fig. 1-1(f). This helical twist can be unwound by a small electrical field, resulting a macroscopic polarization (the polarizations in all layers are parallel to each other) and the molecules all tilting in the same direction. However, in an antiferroelectric SmC_A^* phase, there is a

The work described in this chapter involves the M.I.T. part of a collaboration with K. Ema and H. Yao of the Tokyo Institute of Technology which was carried out before Dr. Yao came to M.I.T. for a postdoctoral/sabbatical visit. We jointly explored the thermal behavior of antiferroelectric liquid crystals. The compound studied at T.I.T. was MHPOBC [4-(1-methylheptyloxycarbonyl)phenyl-4'-octyloxybiphenyl-4-carboxylate], and the compound studied at M.I.T. was MHPOCBC (its octylcarbonylbiphenyl analog). A joint publication describing results on both compounds is given in Appendix A. MHPOCBC has the simpler phase sequence since SmC_α^* and SmC_A^* are the only SmC^* phases, whereas MHPOBC exhibits four SmC^* phases— SmC_α^* , SmC_A^* , SmC^* , and SmC_γ^* .

The antiferroelectric liquid crystal MHPOCBC has the structural formula



where * indicates the chiral center, and its molecular weight is 587 g. The following sequence of phase transitions and transition temperatures (in kelvin) have been reported:³



An overview of the C_p behavior observed with an ac calorimeter (calorimeter A before recent improvements) is shown in Fig. 4-2 for MHPOCBC over the 340-385 K range. The data below 355 K were obtained on cooling at a scan rate of $-1 \text{ K/h} = -17 \text{ mK/min}$. The location of the $\text{SmC}_\alpha^* - \text{SmC}_A^*$ transition temperature (as observed by DSC) and the melting point on heating are marked by arrows in this figure. Note also the very sharp spike observed at 346 K, which represents a region of very rapid freezing as described in Sec. 4.3.

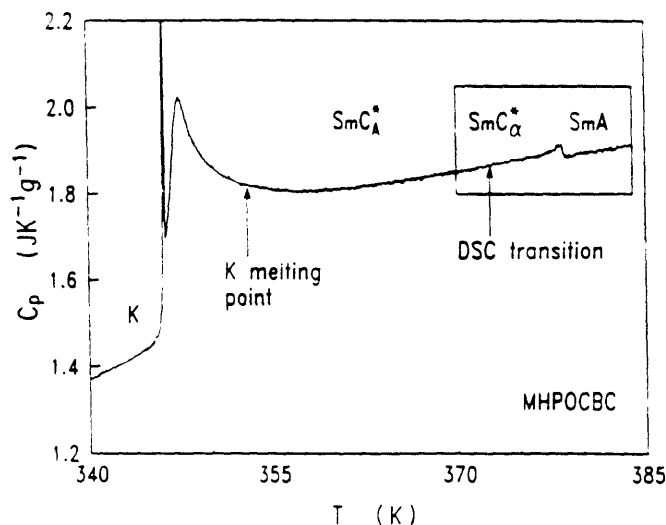


Fig. 4-2. Heat capacity of MHPOCBC. The sharp spike at 346 K represents artificial C_p values with associated anomalous phase shifts ϕ in a region of rapid freezing. A detailed view of the $\text{SmA} - \text{SmC}_\alpha^*$ region enclosed in the box is shown in Fig. 4-3.

4.2 $\text{SmA}-\text{SmC}_\alpha^*-\text{SmC}_A^*$ Transitions

A detailed view of C_p variation in the $\text{SmA}-\text{SmC}_\alpha^*-\text{SmC}_A^*$ region is shown in Fig. 4-3. The MHPOCBC sample was quite stable, and the $\text{SmA}-\text{SmC}_\alpha^*-\text{SmC}_A^*$ transition temperature drift rate was only about -20 mK/d. None of the ac calorimeter runs—heating or cooling—showed any thermal anomaly at the $\text{SmC}_\alpha^*-\text{SmC}_A^*$ transition. This is not surprising in view of the results on the closely related compound MHPOBC. Relaxation calorimetry on MHPOBC material by Prof. K. Ema's group [see Appendix A] revealed that the Smectic- C^* restructuring transitions are all first order with narrow coexistence ranges, small hysteresis (0~0.22K), and very small latent heats (9~16 J/mole). Furthermore, the integrated $\text{SmA}-\text{SmC}^*$ enthalpy for MHPOCBC (0.11 J/g= 65 J/mole) is much smaller than that for MHPOBC (0.66 J/g= 370 J/mole). Thus one might expect the $\text{SmC}_\alpha^*-\text{SmC}_A^*$ latent heat to be very small, and this is confirmed by a DSC value of ~0.02 J/g= ~12 J/mole.

The $\text{SmA}-\text{SmC}_\alpha^*$ transition in MHPOCBC is clearly mean field in character, as evidenced by the absence of excess heat capacity above the transition temperature. These C_p data are well represented by the Landau model [see Chapter 3], in which the heat capacity is expressed by Eqs. (3.5a,b):

$$C_p = C_p^0 \quad \text{for } T > T_0 \quad (4.1a)$$

$$C_p = C_p^0 + A \frac{T}{T_0} \sqrt{\frac{T_k - T_0}{T_k - T}} \quad \text{for } T < T_0 \quad (4.1b)$$

where $C_p^0 = B + E(T - T_0)$ is the regular background heat-capacity variation expected in the absence of a transition. Fits with Eq. (4.1) are in good agreement with the experimental data as shown in Fig. 4-3.

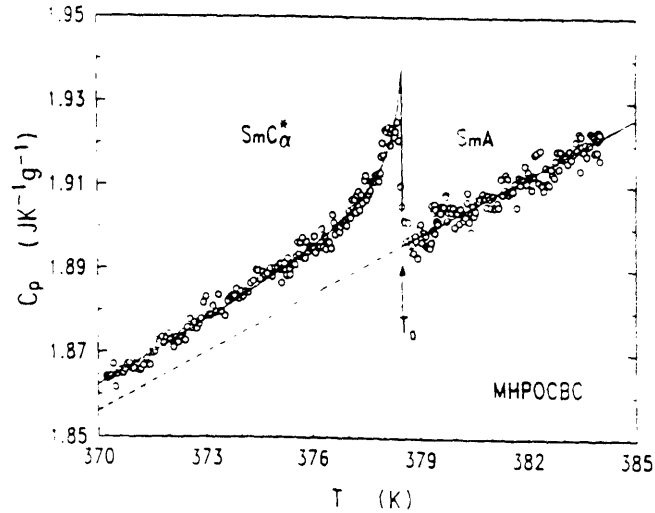


Fig. 4-3. Detail of C_p variation near the $SmA - SmC_\alpha^*$ transition in MHPOCBC, measured in the ac mode. This run was obtained on heating, but equivalent results were also observed on cooling. The solid line represents a Landau model fit with Eq.(4.1) and the dashed line shows the variation of $C_p^0(T)$ below T_c .

The least-squares values of the fitting parameters are listed in Table 4-1 together with the integrated enthalpy defined by $\delta H = \int (C_p - C_p^0) dT$. The δH value in table is in good agreement with DSC results obtained by Dr. Kawamura at Showa Shell Sekiyu ($0.10 \text{ J/g} = 60 \text{ J/mole}$), but the high-resolution ac value is more accurate. Also for comparison are the Landau parameters and δH value for MHPOBC.

Table 4-1. Landau parameters for fitting the $\text{SmA} - \text{SmC}_\alpha^*$ heat capacity data with Eq. (4.1). The units of A and B are $\text{J K}^{-1} \text{g}^{-1}$. The values of background slope of E in units of $\text{J K}^{-2} \text{g}^{-1}$ are $E=0.0055$ for MHPOBC and $E=0.0047$ for MHPOCBC. Also given are integrated enthalpies δH in both J g^{-1} and J mol^{-1} units and values of t_0 .

System	T_c (K)	T_k (K)	B	A	$10^3 t_0$	δH (J/g)	δH (J/mol)
MHPOBC	395.92	396.170	2.132	0.243	1.92	0.66 ± 0.07	370 ± 40
MHPOCBC	378.50	378.708	1.896	0.042	1.65	0.11 ± 0.01	65 ± 6

As mentioned above, the various SmC^* - SmC^* phase transitions of MHPOBC have been detected in a relaxation-mode experiment at the Tokyo Institute of Technology [see Appendix A]. It is found that these transitions are sharp first order ones with very small latent heats: 12 J/mole for $\text{SmC}^* - \text{SmC}_\alpha^*$, 16 J/mole for $\text{SmC}_\gamma^* - \text{SmC}^*$, and 9 J/mole for $\text{SmC}_A^* - \text{SmC}_\gamma^*$. There are at least two examples of phase transitions with similarly small latent heats: (A) the restacking transitions in the plastic crystal B phase of 7O7,⁵ and (B) the lock-in transition in ferroelectric crystals of the Rb_2ZnCl_4 group.⁶ The former example involves transitions between crystal phases with different interlayer orderings.⁷ In the latter case, there is a one-dimensional modulation in the displacement of atoms, and the period of the modulation shows a subtle change at the transition. Therefore, both examples are quite similar to the case of SmC^* transitions in the sense that, in every case, there is only a rearrangement in the interlayer relationship at the phase transition, and the ordering within each layer remains essentially unchanged. It should also be noted that measurements with ac calorimetry failed to detect an anomaly at the above-mentioned lock-in transitions.⁸

4.3 SmC_A to SmI_A Transition and Freezing

Several cooling runs in the region of the $\text{SmC}_A^* - \text{SmI}_A^*$ transition of MHPOCBC are shown in Fig. 4-4. SmI_A^* , which is a

tilted hexatic phase with bond orientational order within the layers, is only seen on cooling since the $\text{SmC}_A^* - \text{SmI}_A^*$ transition lies below the melting point at 353.4 K. Above 349 K, the SmC_A^* phase is long-term metastable with respect to freezing. The values of C_p are reproducible on scanning T from 370 K down to 349 K and then back up to 370 K. Furthermore the C_p value at 349.3 K did not change when the sample was held at that temperature for 67h. On cooling runs made at a constant scan rate, the data show evidence of slow freezing that begins around 347.5 K and terminates with a very rapid complete freezing at 346 K. Associated with the dramatic C_p spike at 346.0 ± 0.2 K shown in Figs. 4-2 and 4-4, there is an abrupt increase in the phase shift between the oscillating power input and the resulting sample temperature oscillation. These two features: artificially high values for the apparent C_p and a jump in the phase shift ϕ are clear indications of two-phase coexistence [see Sec. 2.3]. Three of the data sets shown in Fig. 4-4 were obtained at constant scan rates. Run 1 at -0.5 K/h exhibits a rounded C_p maximum at around 347.5 K (indicating that slow freezing has begun to occur at that temperature) and freezing is complete at 346.4 K two hours later. Run 2 at -1 K/h exhibits a rounded maximum at 347.35 K and a sharp spike at 346.1 K. Run 3 at -4 K/h is so fast that no rounded C_p maximum can be resolved above 346 K, where a sharp spike occurs (off the scale used in

Fig. 4-4). Unfortunately, this run had to be terminated just below 346 K and no data are available at lower temperatures for rapid scans. Five other runs (not shown) with scan rates from -0.7 to -1.5 K/h confirm the general behavior shown for Run 2.

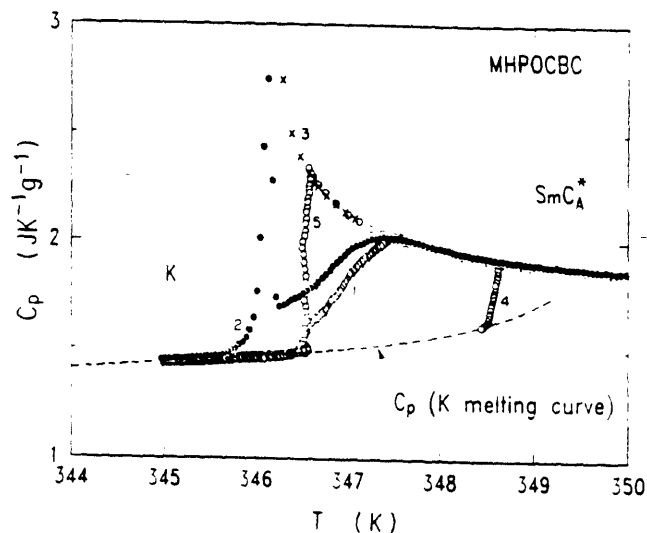


Fig. 4-4. Variation of C_p near the $\text{SmC}_A^* - \text{SmI}_A^*$ transition in MHPOCBC. Below 349 K, the system freezes into crystal K at rates that are very sensitive to temperature. The dashed curve represents the C_p melting curve obtained when K is heated. Runs 1-3 were made at constant scan rates of -0.5 , -1.0 , and -4 K/h, respectively. Runs 4 and 5 were quench-and hold runs with the temperature held approximately constant at 348.5 - 348.6 K and 346.5 K.

As discussed in Chapter 2, these C_p data (except the sharp spike at 346.1 K) represent average values for two coexisting phases α and β : $C_p(\text{coex}) = X_\alpha C_p(\alpha) + X_\beta C_p(\beta)$, where X_α is the mass fraction of the sample in the α phase and $X_\beta = 1 - X_\alpha$. This is the rare case when one can measure $C_p(\text{coex})$ because the phase conversion rate is very slow compared to our experiment time scale for $T > 346.2$ K. The fact that there is a sharp C_p spike at 346.1 K (with anomalous phase shift ϕ) indicates that the phase conversion rate becomes fast compared to our experiment time scale at this temperature. We will argue below that at this temperature the bond orientational order becomes quite well developed and that it accelerates the crystallization. The anomalously high C_p spike values obtained in the ac mode cannot be used to calculate the latent heat since the phase conversion rate is not ideally fast and the sinusoidal modulation of the sample temperature is distorted by phase conversion effects.

In order to characterize the rate of freezing at constant temperature and the dependence of this rate on T , two more runs were carried out where the sample was cooled rapidly to a temperature below 349 K and then held at approximately constant temperature until freezing was complete. These “quench-and-hold” runs are included in Fig. 4-4 and also shown in Fig. 4-5. Freezing into the crystal K phase required 7h

at $T_1 \approx 348.5 \sim 348.6$ K (Run 4) and 2h at $T_2 \approx 346.5$ K (Run 5). From rapid constant-scan-rate runs, one can estimate that the freezing occurs in ≤ 0.5 h at 346 K. Also shown in Figs. 4-4 and 4-5 is a smooth dashed curve giving the variation of C_p for crystal K when it is heated. The data obtained on cooling runs agree very well with this curve after freezing is complete. Furthermore, $C_p(K)$ was also measured for several runs on heating after freezing was complete, and again the agreement (not shown) with the dashed curve is excellent.

As a confirmation that freezing is occurring during the waiting period of the quench-and-hold runs and also during constant-rate scans for temperatures below the value for the rounded C_p maximum, we compared the sample temperature with the bath temperature. When freezing occurs, the release of latent heat raises the sample temperature slightly above the expected value, as shown in Fig. 4-6. These results are completely consistent with the freezing behavior described above.

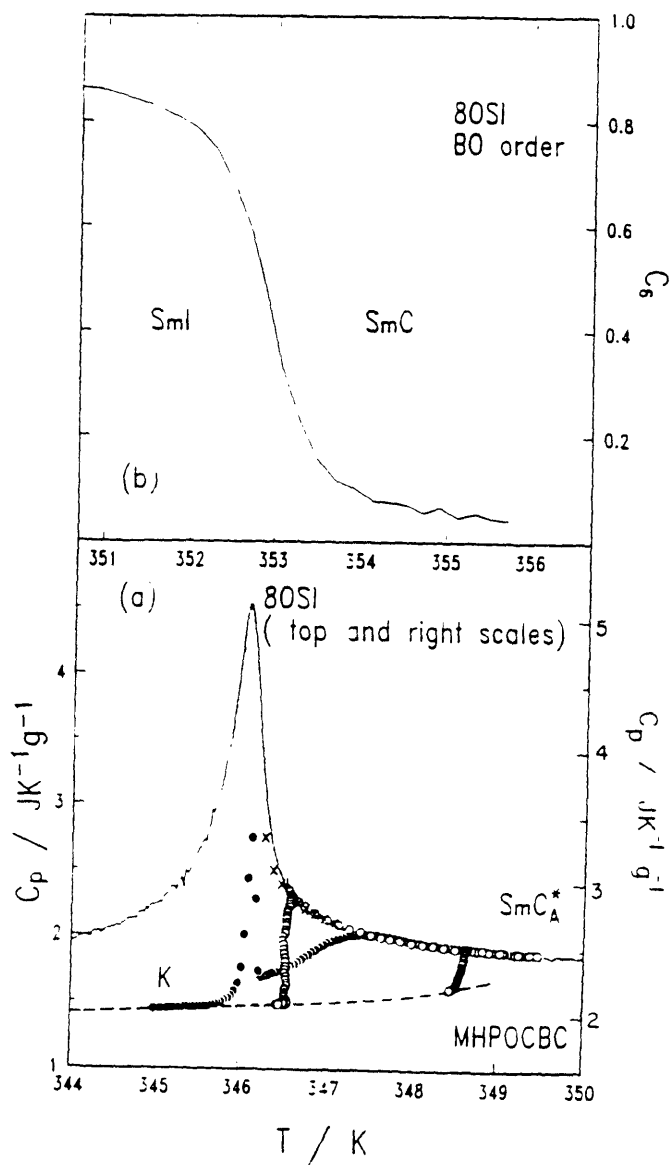


Fig. 4-5. (a) Comparison of SmC-SmI heat capacity variation for 8OSI (Ref. 9)

with MHPOCBC data from Runs 2-5. Note that the sharp C_p spike at 346 K corresponds to the position of the effective transition temperature in 8OSI. (b) Bond-orientational order C_6 for 8OSI. The temperature of the pseudo-transition in this 8OSI x-ray sample is low since the sample was held at high temperatures for a long time and “ T_0 ” shifted down; see Ref. 9.

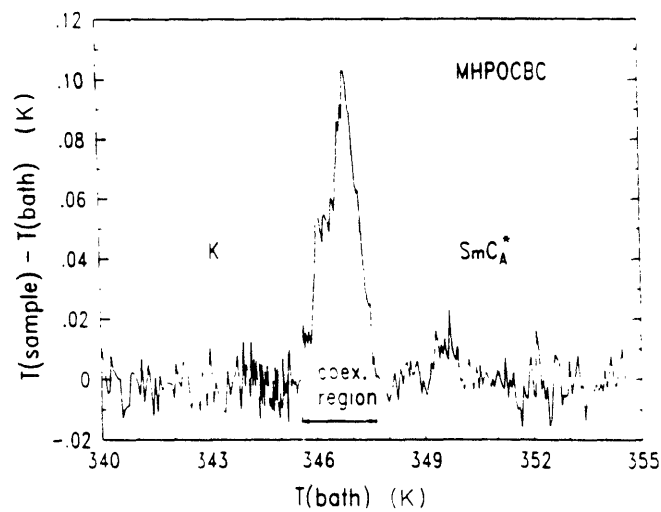


Fig. 4-6. Plot of [$T(\text{sample}) - T(\text{bath})$] for MHPOCBC cooling run 2 made at a scan rate of -1 K/h. The region where $T(\text{sample})$ is anomalously high corresponds to the liberation of latent heat during freezing.

As shown in Fig. 4-5, MHPOCBC exhibits pretransitional excess heat capacity on cooling that is associated with the approach to the $\text{SmC}_A^* - \text{SmI}_A^*$ transition. However, on ac-calorimeter time scales, the sample freezes at or above this transition. Since our calorimeter requires at least 3 min to measure C_p at each point, meaningful data cannot be obtained at scan rates greater than ~ 4 K/h which is 50~ 100 times slower than typical DSC scans. A comparison between our MHPOCBC data and C_p data for racemic 8OSI is given in Fig. 4-5. 8OSI is a chiral compound that exhibits stable hexatic SmI^* and plastic crystal CrJ^* phases and the racemic analogs SmI and CrJ .⁹ Furthermore, the integrated enthalpy for the SmC to SmI transition $\delta H(8\text{OSI})$ is 4.2 Jg^{-1} , in reasonably agreement with the DSC estimate of the enthalpy for MHPOCBC (4.5~6.5 J/g).

Figure 4-5(a) shows that the size and the shape of the MHPOCBC C_p wing matches that for 8OSI quite nicely if one shifts the origins of the T and C_p scales without changing the scale sizes. Furthermore, the sharp spike in the heat capacity of MHPOCBC at 346 K corresponds to the position of $C_p(\text{max})$ in 8OSI, which is the “effective” transition temperature for this supercritical material.^{9,10} The variation of the long-range bond-orientational hexatic order parameter C_6 for 8OSI is shown in Fig. 4-5(b). Due to the presence of a finite tilt field, there is long-range bond orientational order above the effective SmC -

SmI transition temperature. Let us assume that $C_6(T)$ for MHPOCBC is similar to that shown for 8OSI. Thus we would expect $C_6 \approx 0.04$ at 349 K rising to $C_6 \approx 0.23$ at 346.5 K and $C_6 \approx 0.54$ at “ T_c ”=346 K. These values are based on the hypothesis that in the absence of freezing MHPOCBC would undergo a continuous supercritical evolution of bond-orientational order like 8OSI and not a discontinuous first-order $\text{SmC}_A^* - \text{SmI}_A^*$ transition.

We propose that the SmC_A^* phase does not freeze easily to crystal K for moderate ranges of supercooling. However, it seems reasonable that the bond-orientationally ordered SmI_A^* phase can freeze much more easily since only translational lock-in is required. The equilibrium freezing point of MHPOCBC is 353.4 K. In the range from 349 K down to 346.5 K, the extent of C_6 ordering is rather fragmentary, and the freezing proceeds only gradually. But when T approaches 346 K, C_6 increases dramatically and the rate of freezing does so also.

Although our measurements were not designed to characterize the freezing kinetics, it is possible to obtain a preliminary view of this interesting feature. The fraction $X(t)$ crystallized at a given time t after a quench can be estimated from $C_p(t) = X C_p(K) + (1 - X) C_p(\text{SmC}_A^*)$, where $C_p(K)$ is given by the dashed line in Fig. 4-5. For a two-dimensional Avrami model of

nucleation and growth,¹¹ which is appropriate for the freezing of a smectic liquid crystal, one has $X=1-\exp[-A(t)]$, where $A(t)=fG_xG_y\dot{N}_0\int(t-\tau)^2e^{-v\tau}d\tau$. G_x and G_y are linear growth rates, f is a geometric shape factor, $\dot{N}=\dot{N}_0e^{-v\tau}$ is the two-dimensional nucleation rate (number of nuclei formed per unit area per sec) that decays with time, and τ is an incubation time. For $vt\gg 1$ (long times, associated with slow growth), $A(t)\approx\left(\frac{f}{v}\right)G_xG_y\dot{N}_0t^2$, and for $vt\ll 1$ (the regime probed when the growth is rapid), $A(t)\approx\left(\frac{f}{3}\right)G_xG_y\dot{N}_0t^3$. In these limits, one can write $A(t)=B_nt^n$, which leads to $\ln\left[\ln\frac{1}{(1-X)}\right]=\ln A=n\ln t+\ln B_n$. Thus a log-log plot of $\ln(1-X)^{-1}$ vs t should yield a limiting slope of $n=3$ at short times, curving down to a final limiting slope of $n=2$ at long times. Such plots of our data over the most reliable range $0.15<X<0.95$ are curved for Run 4 at early times and yield $n=2$ at later times and are quite straight for Run 5 yielding $n=3$. This trend toward the homogeneous nucleation limit for the rapidly freezing system is just what one would expect.

References

1. A.D.L. Chandani, E. Gorecka, Y. Ouchi, H. Takezoe and A. Fukuda, *Jpn. J. Appl. Phys.* 28, L1265 (1989).
2. Ch. Bahr and D. Fliegner, *Phys. Rev. Lett.* 70, 1842 (1993).
3. T. Isozaki, K. Hiraoka, Y. Takanishi, H. Takezoe, A. Fukuda, Y. Suzuki, and I. Kawamura, *Liquid Crystals*, 12, 59 (1992).
4. T. Isozaki, H. Takezoe, A. Fukuda, Y. Suzuki and I. Kawamura, *J. Mater. Chem.* 4, 237 (1994).
5. J. Thoen and G. Seynhaeve, *Mol. Cryst. Liq. Cryst.* 127, 229 (1985).
6. K. Nomoto, T. Atake, B.C. Chaudhuri, and H. Chihara, *J. Phys. Soc. Jpn.* 52 3475 (1983), and references therein.
7. J. Collett, L.B. Sorensen, P.S. Pershan, J.D. Lister, R.J. Birgeneau, and J. Als-Nielsen, *Phys. Rev. Lett.* 49, 553 (1982).
8. K. Hamano, Y. Ikeda, T. Fujimoto, K. Ema, and S. Hirotsu, *J. Phys. Soc. Jpn.* 49, 2278 (1980); K. Ema, H. Saito, and K. Hamano (unpublished).
9. C.W. Garland, J.D. Lister and K.J. Stine, *Mol. Cryst. Liq. Cryst.* 170, 71 (1989).
10. H. Yao, T. Chan, and C.W. Garland, *Phys. Rev. E*, to appear.

11. J.E. Burke and D. Turnbull, *Prog. Met. Phys.* 3, 220 (1952);
H. Orihara, Y. Ishibashi and Y. Yamada, *J. Phys. Soc. Jpn.*
57, 4101 (1988).

Chapter 5

Twisted-Grain-Boundary Phases In Chiral Liquid Crystals

5.1 Structure of TGB_A Phase

We have seen in Chapters 3 and 4 that the chirality of liquid crystal molecules can induce certain kinds of helical structure in liquid crystal phases such as N^* and SmC^* . As the chirality increases, more complicated liquid crystal phases can be formed. The blue phases BP_I , BP_{II} , and BP_{III} are examples of structures that can occur between the isotropic (I) and cholesteric (N^*) phases. Experimental data show that BP_I has a body-centered cubic structure, BP_{II} has a simple cubic structure, and BP_{III} is amorphous but with short-range chiral order.¹ High-resolution adiabatic scanning calorimetry by Thoen² demonstrated that the I- BP_{III} transition is weakly first order (like a N-I transition in achiral compounds), while BP_{III} - BP_{II} , BP_{II} - BP_I , and BP_I - N^* transitions are strongly first order (no pretransitional effects in C_p) but have very small latent heats.

In order to discuss the effects of chirality on the structures of smectic liquid crystals, one can make an analogy between a

superconductor and a SmA liquid crystal, as first done by de Gennes.³ The SmA phase is a layered phase with the director normal to the plane of the layers. According to the analogy, the application of a twist or bend distortion to a SmA liquid crystal is analogous to the application of a magnetic field to a superconductor. There are two types of superconductors. For a type-I material, there is only one phase transition between the normal metal state and the superconducting (Meissner) state. In the Meissner state, the magnetic induction is expelled from the superconductor ($B=0$ up to a critical external field H_c). However, for a type-II material, in addition to the normal and Meissner phases, a more complicated superconducting state can exist even in the mean-field approximation. The magnetic induction can penetrate the material in a lattice of flux vortices referred to as the Abrikosov flux lattice. There is experimental evidence for the existence of even more complicated flux vortex states in High- T_c superconductors that may be described as flux liquids or flux glasses.⁴ In Table 5-1 we list detailed information about the superconductor-liquid crystal analogy⁵ obtained by comparing Ginzburg-Landau mean-field theory of superconductivity and Chen-Lubensky model of liquid crystals. According to this analogy, the TGB_A phase corresponds to the Abrikosov flux lattice phase and N^* corresponds to the normal metal state. Thus the TGB_A-N^* transition is analogous to the melting of the Abrikosov flux lattice to the metallic state. This transition is found to be first

order in some high- T_c superconductors.⁴ By the same analogy, SmA corresponds to the Meissner phase. Thus TGB_A to SmA transition corresponds to the expulsion of magnetic induction B from the superconductor. This transition is predicted to be second order in mean field theory but may be first order due to fluctuation effects.

There have been very few experimental results on the thermodynamic properties (heat capacity and latent heats) for the phase transitions between the vortex flux states in superconductors. These thermal anomalies have been estimated to be very small,³ and maybe this is the reason why the phase transitions between the vortex flux states have eluded calorimetry experiments. Recall that in order to measure small latent heats, one needs to use high-resolution adiabatic calorimeter or relaxation calorimeter [see Chapter 2]. If the superconductor-liquid crystal analogy is valid, one may gain some insights about the vortex flux states by studying the phase transitions of the liquid crystal analog, i.e., the N^* , TGB_A , and SmA phases.

Recently there have been both theoretical and experimental advances in the study of twisted smectics. Renn and Lubensky⁵ postulated a specific model for the liquid crystal analog of the type-II Abrikosov flux lattice. This model consists of regularly spaced grain boundaries of screw dislocations which are parallel to each other within a given grain boundary but are rotated by a

Table 5-1. The de Gennes analog between liquid crystals and type-II superconductors.

Superconductor (SC)	Liquid crystal (LC)
ψ = Cooper pair amplitude	ψ = density wave amplitude
\mathbf{A} = vector potential	$\bar{\mathbf{n}}$ = nematic director
$\mathbf{B} = \nabla \times \mathbf{A}$ = magnetic induction	$\bar{\mathbf{k}}_0 \equiv \bar{\mathbf{n}} \cdot \nabla \times \bar{\mathbf{n}}$ = twist
normal metal	nematic phase
normal metal in a magnetic field	cholesteric (N^*) phase
Meissner phase	Smectic-A phase
Meissner effect	twist expulsion
London penetration depth λ	twist penetration depth λ_2
superconducting coherence length ξ	smectic correlation length ξ
vortex (magnetic flux tube)	screw dislocation
Abrikosov flux vortex lattice	twist grain boundary TGB_A phase
Abrikosov flux vortex liquid	twisted line liquid ($N_L^* = N^*$ with SRO of screw dislocation lines)
—————	Smectic- C^* phase (due to negative gradient coefficient c_{\perp}) ^{9,10}

fixed angle with respect to the screw axis in adjacent grain boundaries. Thus the grain boundaries separate the sample into SmA blocks, each of which is rotated about the pitch axis by a discrete amount relative to adjacent blocks. See Fig. 5-1 for a sketch of this structure. The resultant phase has been named a “twist-grain-boundary” (TGB_A) phase. On the experimental front, Goodby et al.⁶ reported the discovery of a novel SmA-like phase composed of chiral molecules in which the layers twist along an axis parallel to the layer planes, thus forming a macroscopic helical structure. They referred to this phase as smectic- A^* . Their optical, calorimetric (DSC), and x-ray investigations⁷ showed that the TGB_A phase of Renn and Lubensky was a feasible model for this smectic- A^* phase.

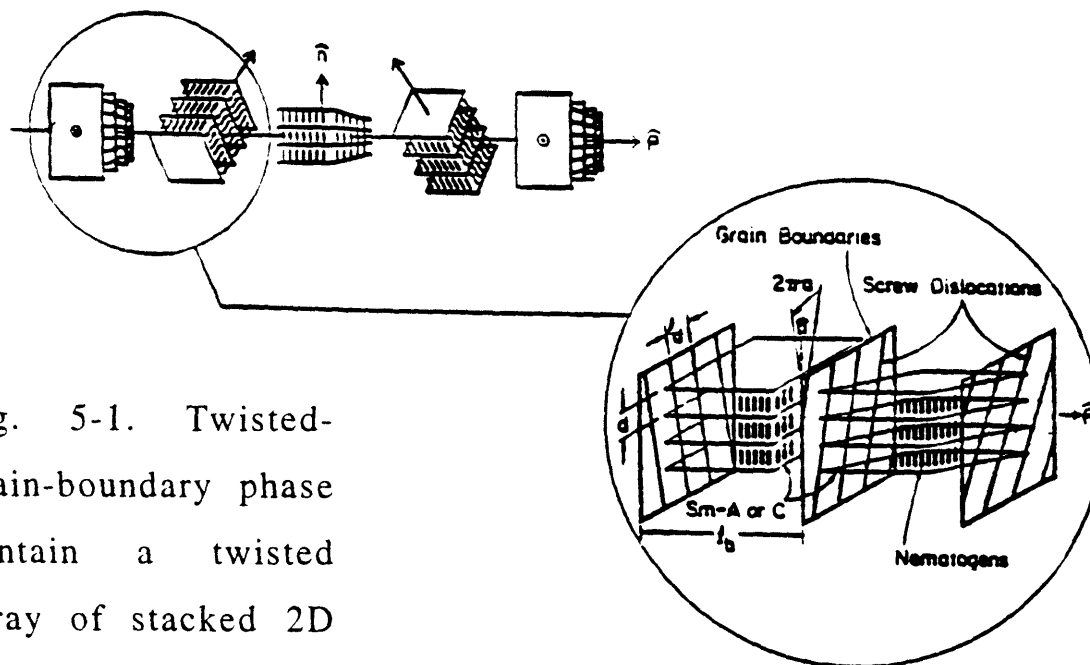


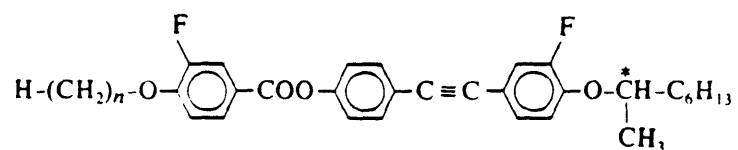
Fig. 5-1. Twisted-grain-boundary phase contain a twisted array of stacked 2D smectic slabs. Sketch taken from Ref.5.

Further experimental studies have confirmed the existence of TGB_A phases. A helical structure with a 0.5- μm pitch along a pitch axis that is parallel to 4.1-nm thick smectic layers has been found by freeze fracture in the liquid crystal 14P1M7.⁸ The layers are disrupted by a lattice of screw dislocations oriented normal to the helical pitch axis. The rotation of smectic blocks occurs in discrete steps of about 17° , the screw dislocations are 15 nm apart and the grain boundaries are 24 nm apart.

More recently, tilted smectic analogs of the TGB_A phase described above have been predicted theoretically and found experimentally.⁹⁻¹¹ Instead of twisted blocks of SmA, the structure of the new phase involves blocks of SmC. Thus the new phase is called TGB_C . Indeed, there may possibly be more than one type of TGB_C phase.

5.2 Experimental Phase Diagram

TGB_A phases have been found in a new series of chiral molecules with a tolan core (called $n\text{FBTFO}_1\text{M}_7$) synthesized at the Centre de Recherche Paul Pascal (CRPP) in Bordeaux France.¹² The structural formula for this series is



where $n=7-18$, and the chemical name is 3-fluoro-4[(R) or (S)-1-methylheptyloxy] 4'-(4''-alkoxy-3''-fluorobenzoyloxy) tolan. The molecular weight for the $n=9$ member of the series is 604.78 g.

The N^* - TGB_A - SmA phase sequence is observed in several compounds with moderate chain lengths ($n=8\sim 10$) and the N^* - TGB_A - SmC^* sequence for longer chain lengths ($n=11\sim 14$). The experimental phase diagram determined from x-ray studies, optical microscopy, and DSC is shown in Fig. 5-2.

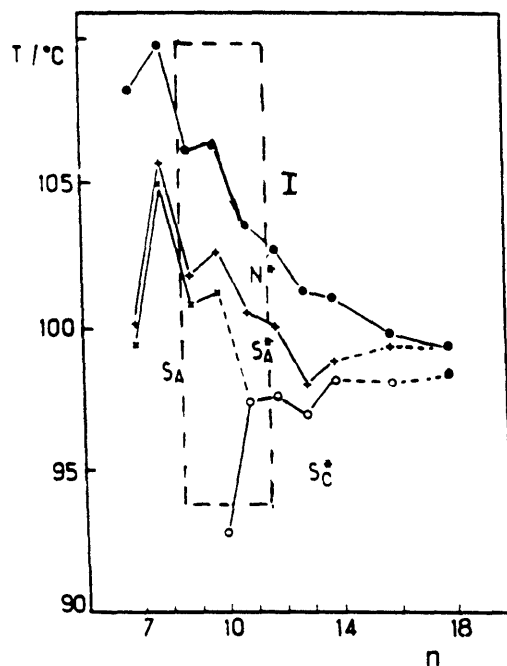


Fig. 5-2. Phase diagram for $nFBTFO_1M_7$ homologs with terminal chain length n . S_A^* denotes our TGB_A phase; S_A and S_C^* are SmA and SmC^* . Taken from Ref. 12 with corrections. A detailed phase diagram corresponding to the dashed rectangle has been obtained from our C_p data; see Fig. 5-7.

Although numerous phase transitions occur in nFBTFOM (we will suppress the subscripts on O and M), the principle interest is the N*-TGB_A and TGB_A-SmA (or TGB_A-SmC*) transitions. The only published evidence concerning these transitions is the DSC data obtained by the group at CRPP.¹² Their result for the n=10 homolog is shown in Fig. 5-3 as a typical example of such DSC data. The scanning rate used was 0.1 K/min, which is slow for DSC but very fast compared to our ac calorimeter scan rate of ~0.1 K/h. Although DSC is a sensitive tool for detecting small enthalpy changes, the temperature resolution is poor. Furthermore, DSC cannot distinguish between first-order and second-order transitions. In order to study the thermodynamic behavior at TGB_A phase transitions, I have carried systematic studies on a series of nFBTFOM liquid crystals using our high-resolution ac calorimeter (calorimeter A) and the new complex calorimeter (calorimeter B) capable of measuring latent heat in the relaxation mode.

DSC Data File: c1f0
 Sample Weight: 5.540 mg
 Thu May 23 12:39:31 1991
 C10H210<F>CD2<>C=C<F>0G8xH17

PERKIN-ELMER
 7 Series Thermal Analysis System

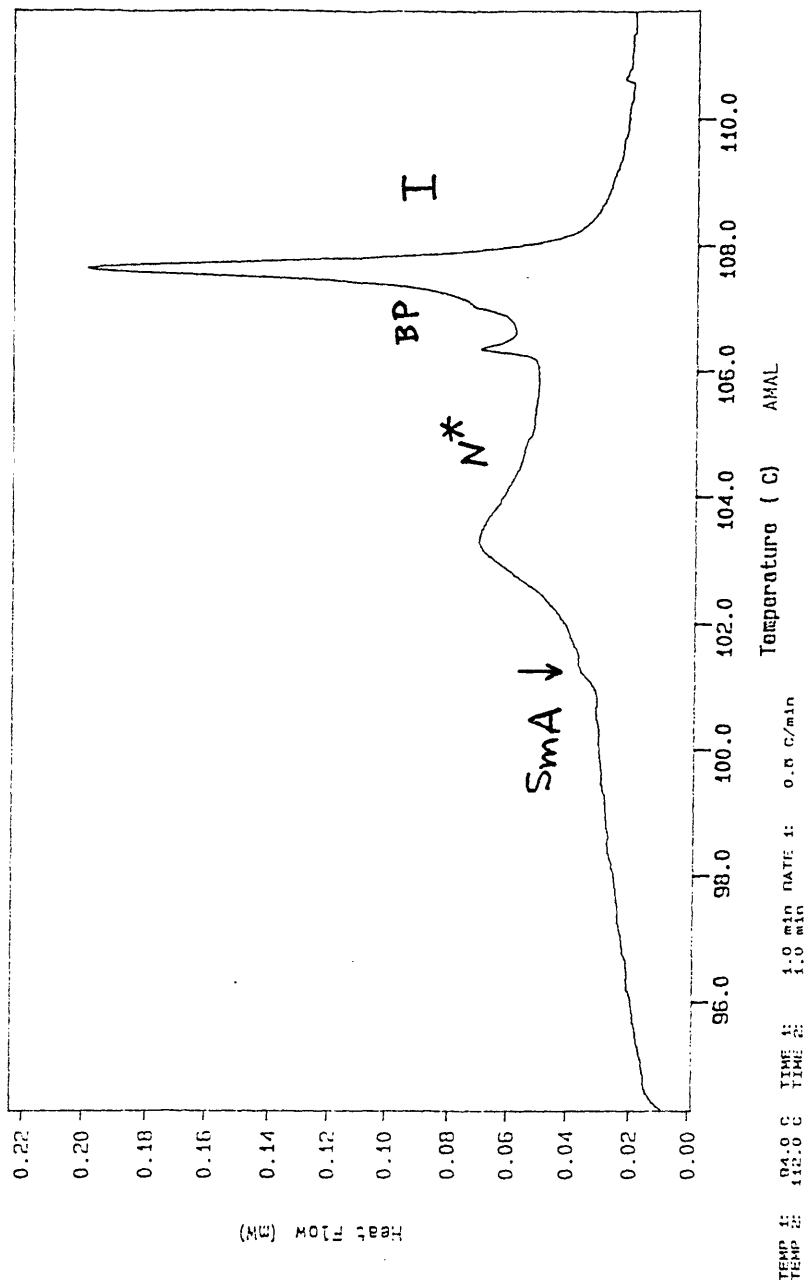


Fig. 5-3. DSC data on $10\text{FBTFO}_1\text{M}_7$ obtained at CRPP in Bordeaux, France.

5.3 Heat Capacity Data From ac Calorimetry

A. Overall View of Heat Capacity Data

I have made heat capacity measurements on the homologous nFBTFOM materials for $n=9,10,11$, and an equimolar mixture of $n=10$ and $n=11$. The C_p data for $n=9$ and $n=10$ with the corresponding phase shift data are shown in Fig. 5-4. These data were obtained in the ac mode at the standard operation frequency $\omega_0 = 0.19635$ (T_{ac} periods of 32 s). Notice the rich structure of features in the phase shift data. The sharp spikes are indications of first-order two-phase coexistence, which has been confirmed by relaxation calorimetry described later. Also notice the presence of “steps” in the phase shift data. The C_p data corresponding to these steps exhibit very small anomalies. Relaxation calorimetry has revealed that these steps in ϕ also indicate two-phase coexistence, as we will discuss later. An overview of the C_p data for all four investigated samples is given in Fig. 5-5.

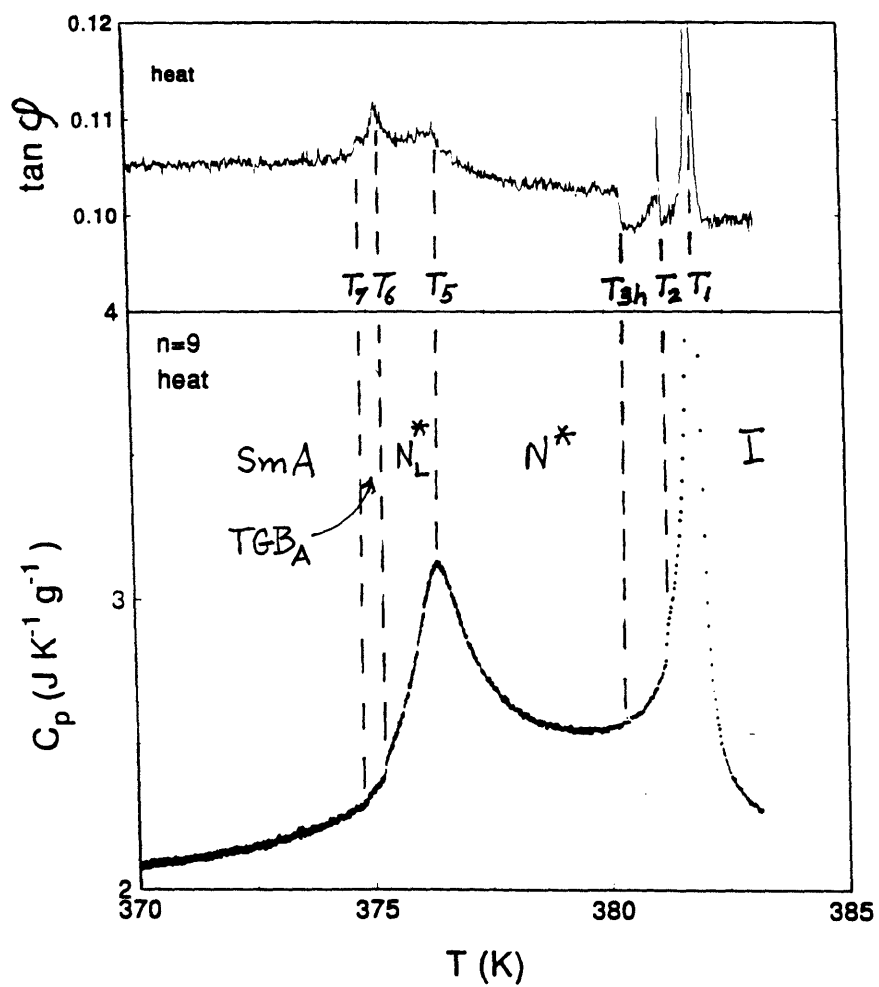


Fig. 5-4. (a) ac calorimetry C_p and phase shift data on 9FBTFOM.

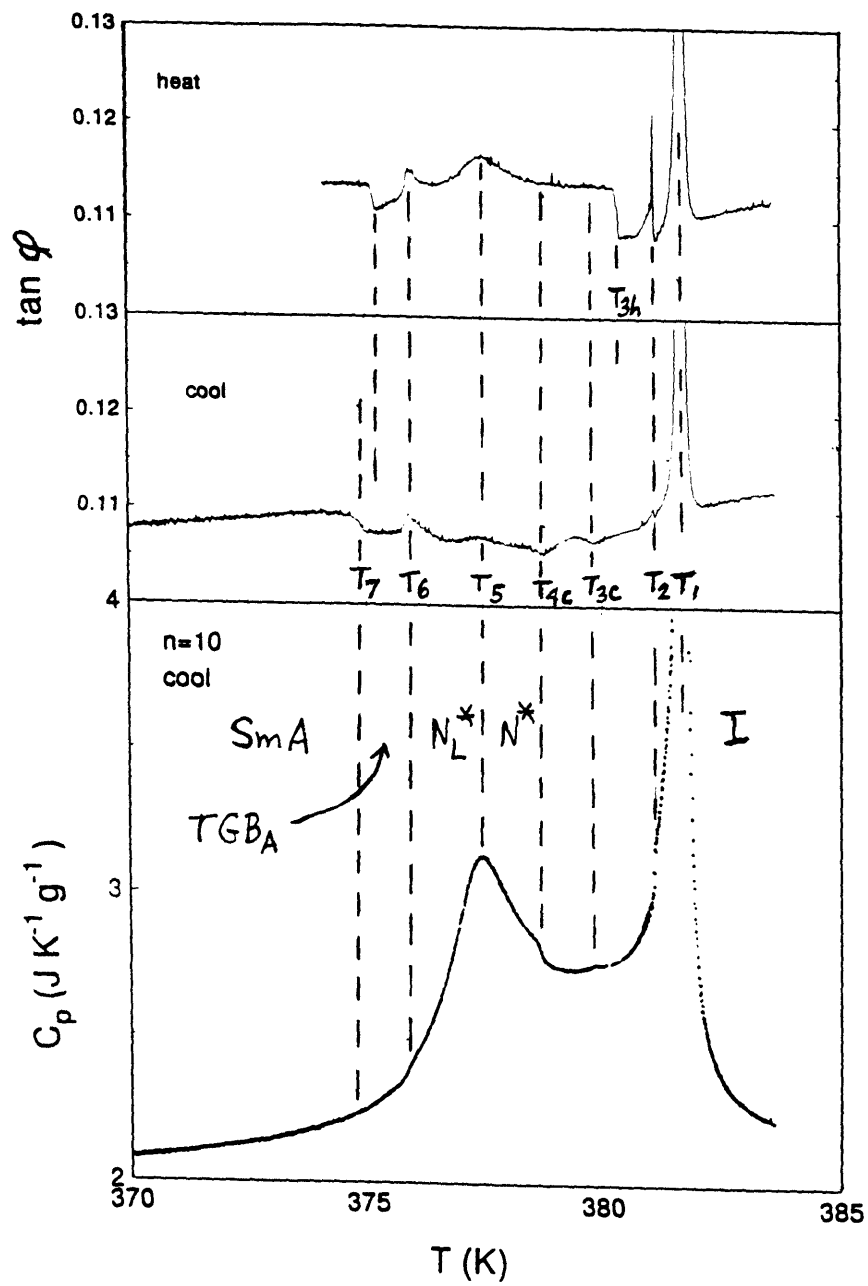


Fig. 5-4. (b) ac calorimetry C_p and phase shift data on 10FBTFOM.

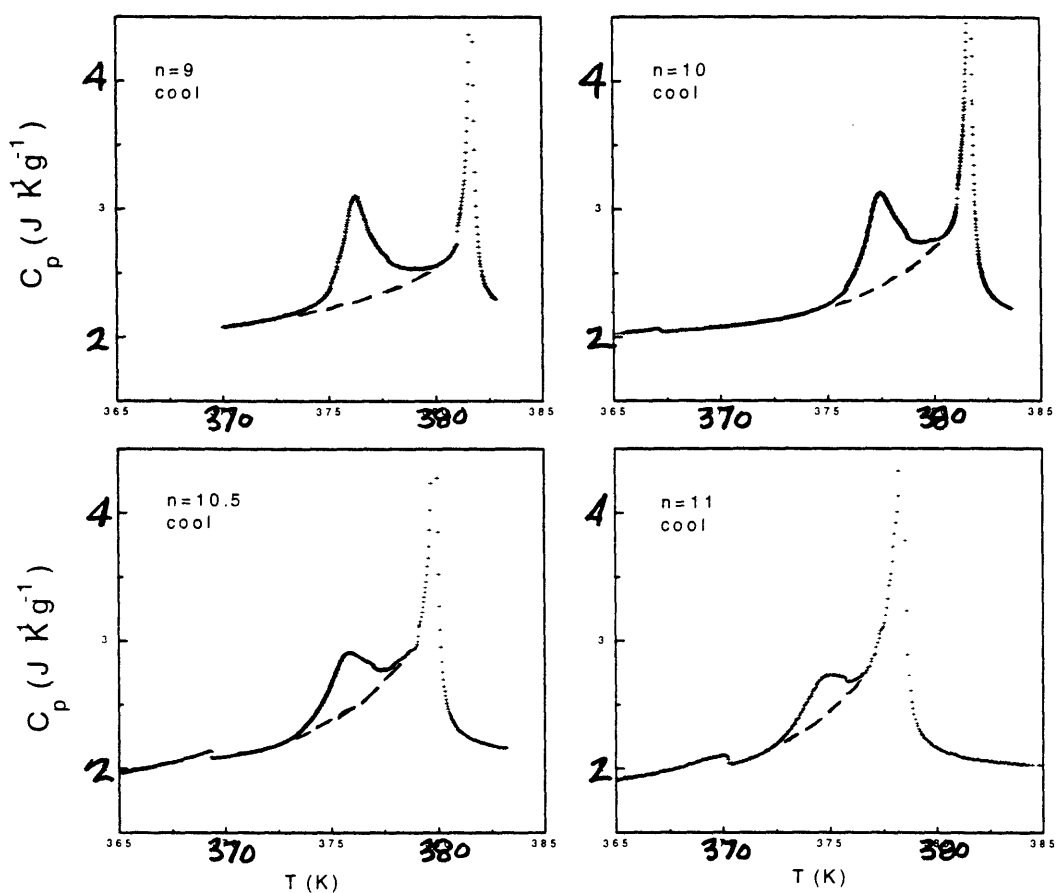


Fig. 5-5. ac calorimetry heat capacities for nFBTFOM. The dashed lines represent the normal low-T tail observed in lower chirality materials with the I-BP-N* phase sequence but no TGB_A phase.²

B. Discussion Of the Phase Shift ϕ

The zero-dimensional model discussed in Sec. 2.1 is only the simplest approximation to a complicated thermal system. Although this model has been demonstrated to be applicable to our set-up for measurements of C_p , the phase shift behavior has not been fully discussed. In the past, an abrupt increase (spike) in the phase shift ϕ was taken to as a qualitative indication of two-phase coexistence. This practice was supported empirically by the appearance of ϕ spikes at N-I transitions and melting (crystal K-SmA or K-N) transitions, both of which are well known to be first order. Such an empirical “rule-of-thumb” already implied that the anomaly in phase shift is caused by thermal properties of the sample. It is clear that the silver sample cell, heater, electrical leads, and GE vanish do not have such anomalous behavior since they do not have any phase transitions in the investigated temperature range. We will argue that the observed ϕ anomalies are caused by changes in the effective sample thermal conductivity. In the case of TGB_A materials, the phase shift is more sensitive to first-order phase transitions than the C_p data itself.

Many authors¹³ have discussed the one-dimensional model for thermal analysis shown schematically in Fig. 5-6. In ac calorimetry, a sinusoidal power is input onto one surface of the sample. The sample temperature is monitored at the opposite

surface. The system exchanges heat with a thermal bath. Assume the heat flow can be described by a simple one-dimensional diffusion equation; then in the steady state the sample temperature has the same ac component as in the zero-dimensional model. Under the condition $\tau_{\text{int}} \ll \tau_{\text{ext}}$, one obtains¹³

$$\tan \varphi \approx \frac{\frac{1}{\omega R C_p^{\text{sys}}} - \omega \tau_{\text{int}} \left(\frac{1}{24} \frac{\tau_{\text{int}}}{\tau_{\text{ext}}} + \frac{1}{6} \right)}{1 + \frac{1}{2} \frac{\tau_{\text{int}}}{\tau_{\text{ext}}} - \left(\frac{1}{6!} \frac{\tau_{\text{int}}}{\tau_{\text{ext}}} + \frac{1}{5!} \right) (\omega \tau_{\text{ext}})^2}, \quad (5.1)$$

where τ_{int} is the internal thermal diffusion time of the sample (depending on its thermal conductivity and geometry), R is the thermal resistance between the sample cell and the thermal bath (including exchange gas, electrical leads, etc.), and $\tau_{\text{ext}} = R C_p^{\text{sys}}$ is the time constant for heat exchange between the sample and the bath. This model predicts that the phase shift φ depends not only on R and C_p^{sys} but also on the sample thermal conductivity and the operating frequency ω . At very low frequencies $\omega \rightarrow 0$ and when $\tau_{\text{int}} \ll \tau_{\text{ext}}$, Eq. (5.1) reduces to the result for a zero-dimensional model Eq. (2.16b): $\tan \varphi \approx 1/\omega R C_p^{\text{sys}}$. Since R is a smooth function of T , $\tan \varphi$ is almost inversely proportional to the heat capacity C_p^{sys} in the low-frequency limit.

It should be realized that our experimental setup cannot be fully described by the zero-dimensional model. Actually, our experimental data on the phase shift φ exhibit some features of the one-dimensional model. The $\tan \varphi$ data we obtained are indeed

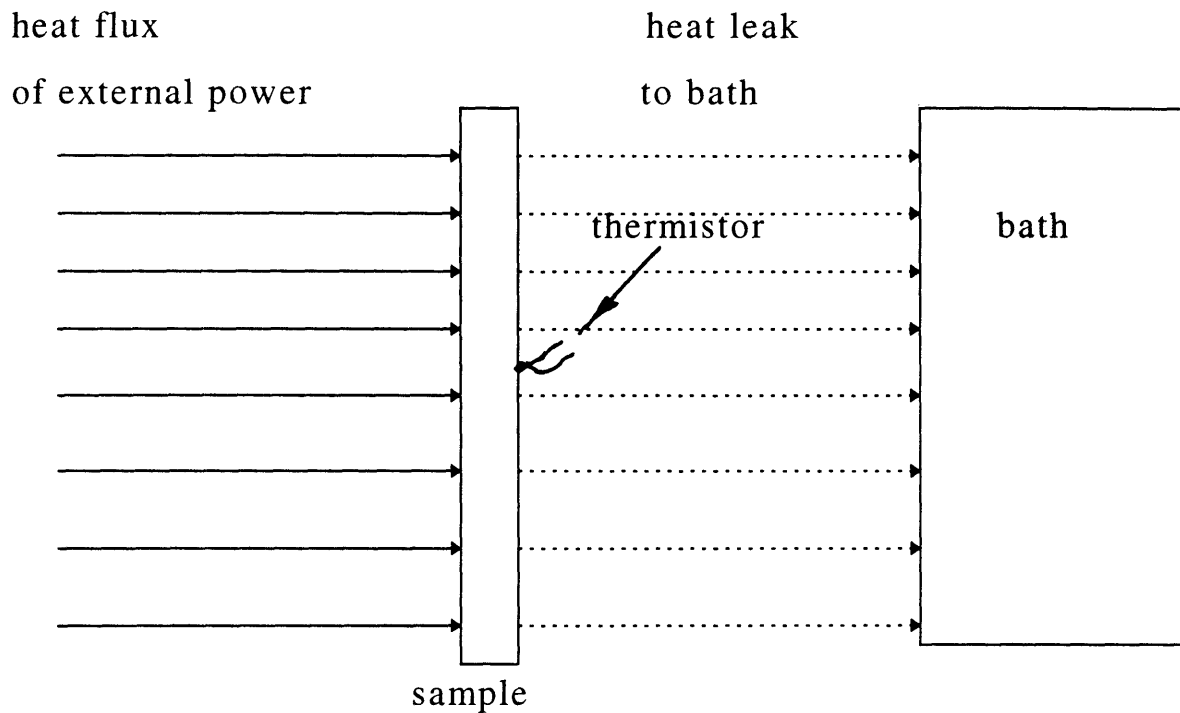


Fig. 5-6. One-dimensional model for thermal analysis. The sample is slab-like with power input on one surface and thermistor on the other surface monitoring the temperature at this back surface.

almost inversely proportional to the heat capacity C_p^{sys} when the operating frequency is very low in the ac mode (say $\omega_0/9$). However, Fig. 5-4 clearly shows that the phase shift data have more complicated structures at the standard frequency ω_0 ; and this is presumably due to the behavior of the effective thermal

conductivity of the sample, which can be quite complicated in a two-phase coexistence region where many small domains form. (Note that if one treat the ac calorimetry as a kind of spectroscopy to measure the dynamic heat capacity, the phase shift should be reformulated and it has contributions from slow dynamics. See Chapter 6.)

C. Transition Temperatures

The phase transitions and anomalous features in nFBTFOM materials observed with high-resolution calorimetry are listed in Table 5-2A. A phase diagram based on these data is shown in Fig. 5-7. Detailed analysis of the order of transitions will be given later. Note that there is a large metastability for the cholesteric (N^*) phase on heating. On cooling, the BP_{II} - BP_I transition occurs at temperature T_{3c} followed by the BP_I - N^* transition at T_{4c} , which is about 1 K lower than T_{3c} . On heating, no BP_I phase is observed and N^* transforms directly to BP_{II} at T_{3h} , which is ~ 0.4 K higher than T_{3c} . The rounded C_p feature at T_5 is reproducible on heating and cooling but it should be noted that there is no thermodynamic phase transition here, as discussed later.

We also list transition temperatures obtained by the CRPP group in Table 5-2B. Note that the temperature scales for DSC data are poor(systematically low by 0.8-1.15 K compared to our high-resolution ac calorimetry results in Table 5-2A). If the DSC transition temperature values for a given n are all increased by the same amount, there is reasonably good agreement with our C_p

data. Also note that the TGB_A range obtained by optical microscopy agrees well with that given by our C_p measurements, as shown in Fig. 5-7.

Table 5-2A. Transition Temperatures (in $^{\circ}C$) of nFBTFOM (C_p data). The symbol N_L^* denotes a cholesteric line liquid, which has short-range TGB_A structure.¹⁴ N^* and N_L^* both have the same symmetry, and T5 is not a transition temperature.

		n=9	n=10	n=10.5	n=11
T1	I-BP _{III}	108.7	108.4	106.8	105.3
T2	BP _{III} -BP _{II}	108.1	107.8	106.1	104.6
T3h	N^* -BP _{II}	107.2	107.0	105.5	104.1
T3c	BP _{II} -BP _I	missing	106.6	105.3	103.6
T4c	BP _I - N^*	104.7	105.3	104.0	102.7
(T5)	N^* - N_L^*	103.2	104.1	103.0	101.5
T6	N_L^* - TGB_A	102.0	102.5	100.8	missing
T7	TGB_A -SmA	101.4	101.4	100.0	N/A
T8	TGB_A -SmC [*]	N/A	N/A	N/A	97.0
T9	SmA-SmC [*]	N/A	94.2	96.3	N/A

Table 5-2B. Transition Temperatures (in °C)
of nFBTFOM (microscopy and DSC data
from CRPP¹²)

	n=9 micro	n=9 DSC	n=10 micro	n=10 DSC	n=11 micro	n=11 DSC
T1		107.6		107.6		104.6
T2	106.3	106.8	106.8	107.0	103.7	104.0
T3h		106.2		106.35		103.2
T3c	106.1		106.1		103.5	
T4c			105.2			
(T5)		102.0		103.2		~100.6
T6	101.8		102.6		100.5	
T7	100.8	100.4	101.2	101.1		
T8					97.4	96
T9			~96			
freeze	59.4		63.4		68	

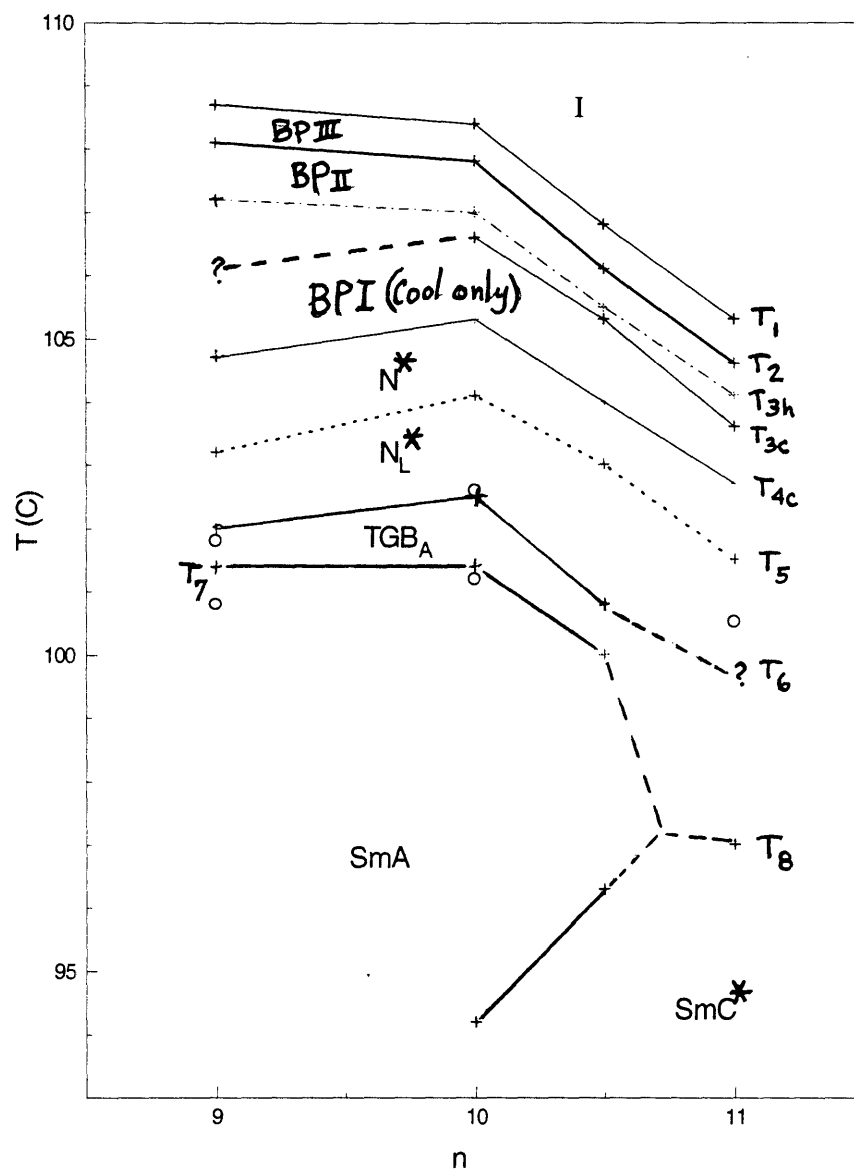


Fig. 5-7. Phase diagram for nFBTFOM obtained from our C_p data.

D. Features in N^* Phase

Detailed views of C_p data in the N^* - TGB_A - $SmA(SmC^*)$ region are shown in Figs. 5-8a-d. These C_p data exhibit large rounded peaks (T_5) in the middle of the N^* phase. This is the sort of behavior which usually represents supercritical enthalpy evolutions not true thermodynamic phase transitions.¹⁵ A recent paper by Kamien and Lubensky¹⁴ proposes a model of “twisted line liquids” that are cholesterics with melted entangled screw dislocation lines(short range order) that may explain this feature. We denote this chiral line liquid as N_L^* . Notice also the very small C_p features at the N_L^* - TGB_A and TGB_A - SmA transitions to be discussed below.

E. N_L^* - TGB_A Transitions

The N_L^* - TGB_A transitions (T_6) show up in the ac C_p data as small steps, detailed views of which are shown in Fig.5-9. The corresponding phase shift data show peaks at the standard frequency ω_0 [see Figs. 5-4(a) and (b)], which indicates two-phase coexistence. This first-order character has been confirmed for $n=9$ by relaxation Calorimetry to be described in Sec. 5.4. Note that the C_p step is most distinct for $n=9$ and becomes progressively less distinct for $n=10$ and 10.5 . No step could be detected in the C_p data for $n=11$ but a smeared ϕ anomaly was seen at 373.8 K.

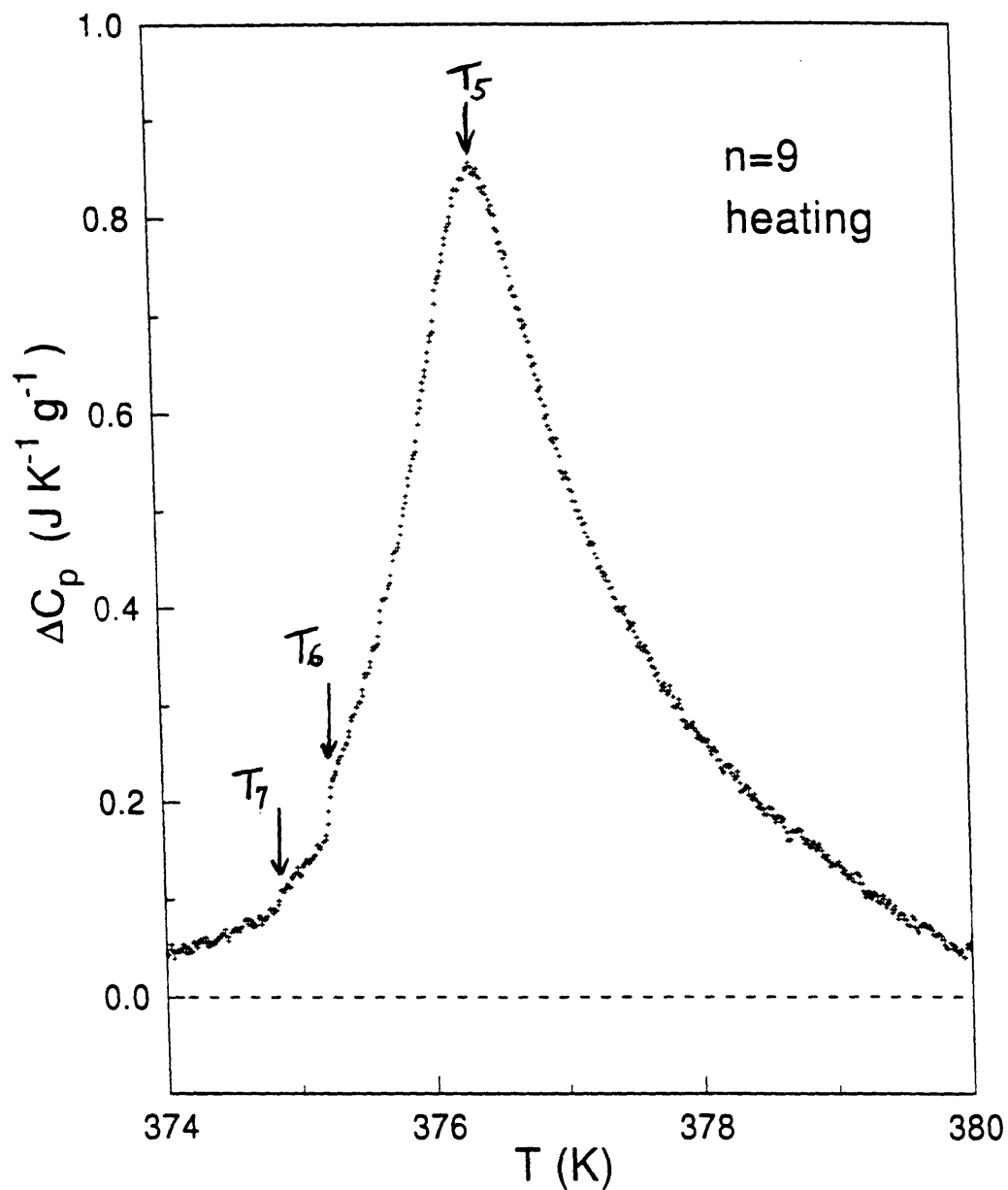


Fig. 5-8. (a) Excess heat capacity (above the dashed line in Fig. 5-5) for 9FBTFOM. Transitions are marked by arrows. The total integrated enthalpy $\delta H = \int \Delta C_p dT$ is 1.91 J/g.

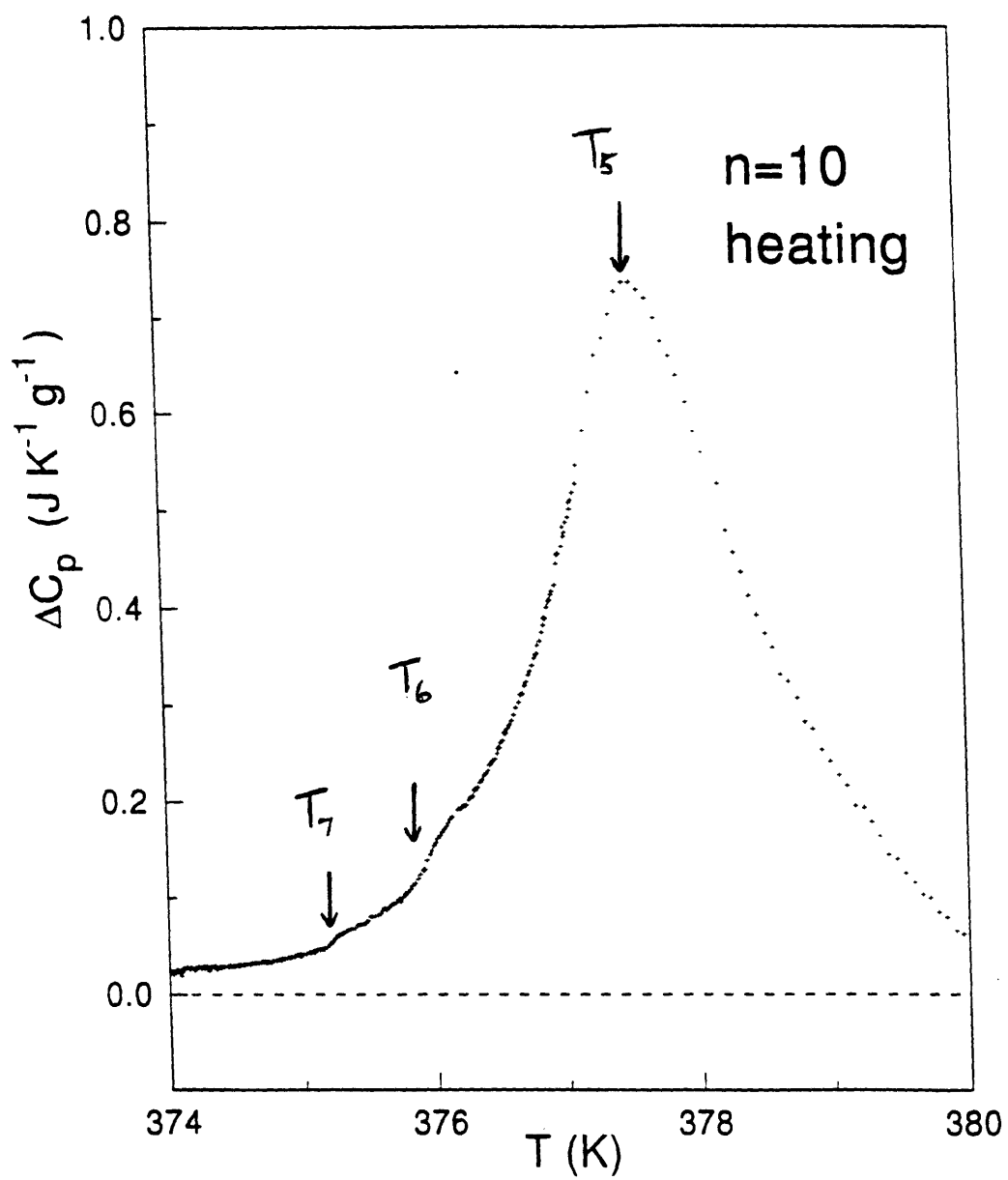


Fig.5-8. (b) ΔC_p for 10 FBTFOM.

$\delta H = 1.53 \text{ J/g.}$

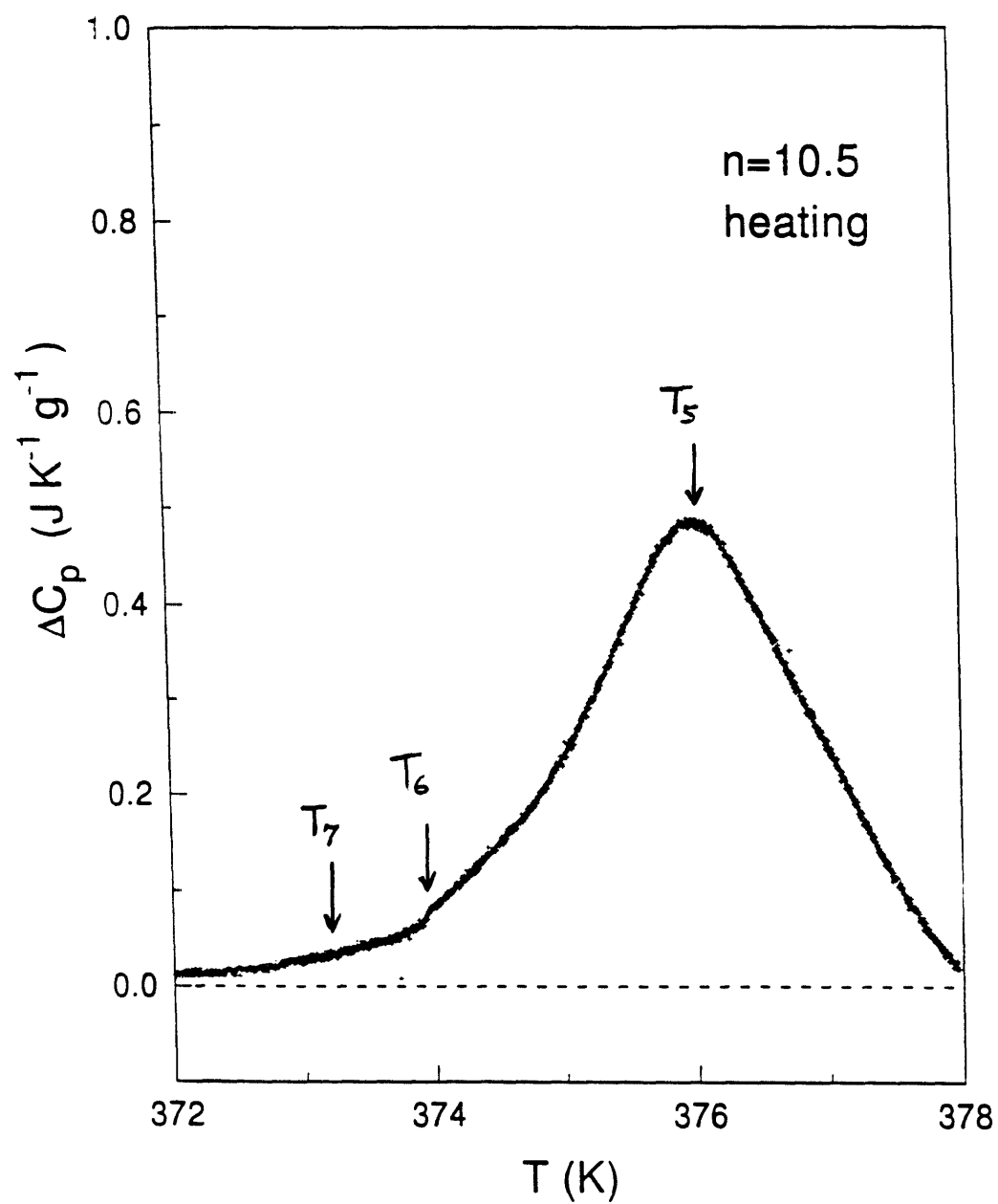


Fig. 5-8. (c) ΔC_p for equimolar mixture of 10FBTFOM and 11FBTFOM. $\delta H = 1.05 \text{ J/g}$.

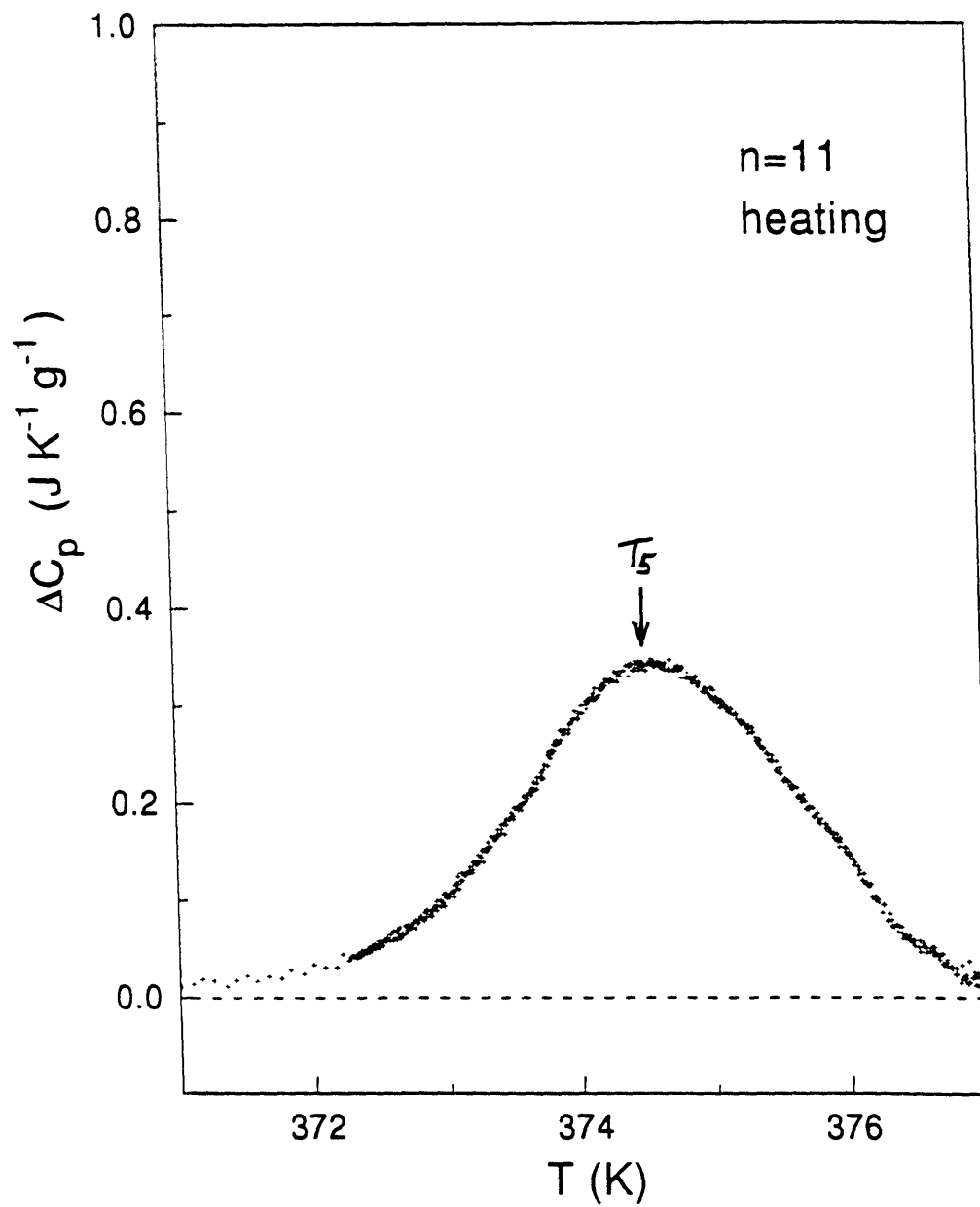


Fig. 5-8. (d) ΔC_p for 11 FBTFOM.
 $\delta H = 0.90 \text{ J/g.}$

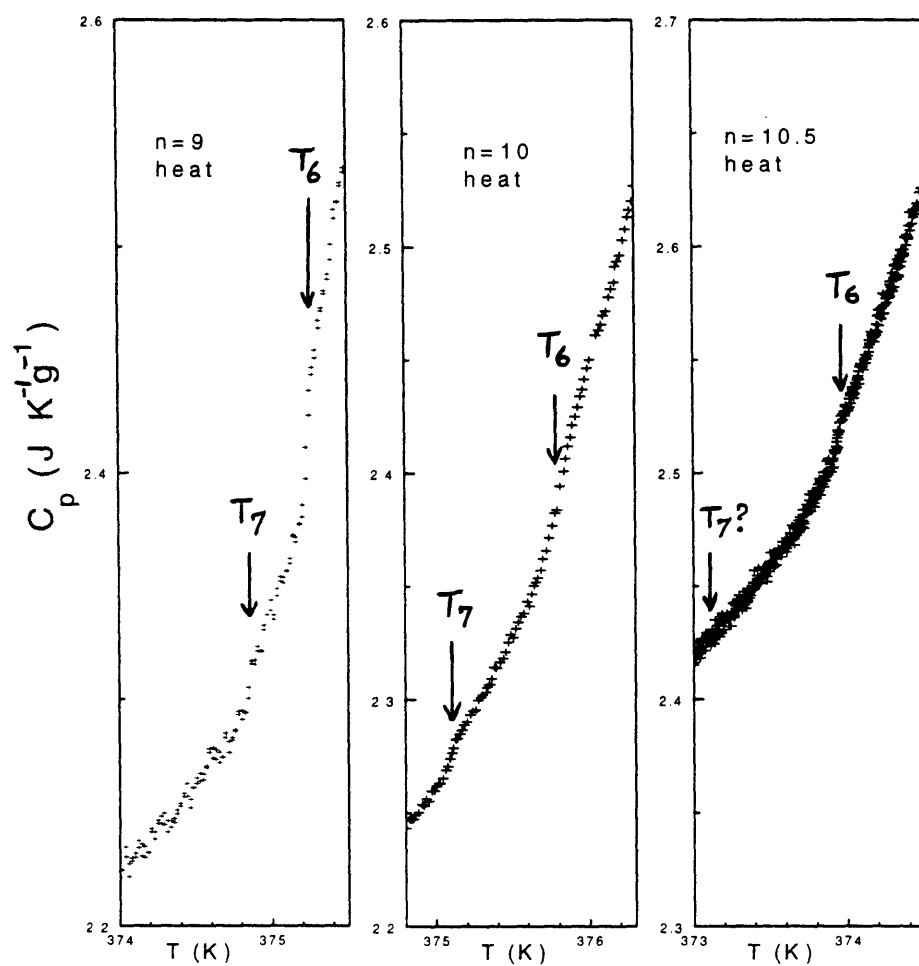


Fig. 5-9. Detail of C_p variation for nFBTFOM in the region of the N_L^* - TGB_A (T_6) and TGB_A -SmA (T_7) transitions.

F. TGB_A -SmA Transitions

The TGB_A -SmA transitions give rise to very small indistinct features in the ac C_p data (see Fig. 5-9 at the positions marked T_7), but the corresponding phase shifts exhibit clear steps and significant hysteresis. The positions of the ϕ step differed on heating and cooling runs by 0.25 K for $n=10$. In the case of $n=11$, a badly smeared step-like ϕ variation occurred in the vicinity of T_6 to T_7 but this should be associated with the N^* - TGB_A transition since microscopic textures show no SmA phase.¹² The first-order character of this transition has been confirmed by relaxation calorimetry.

G. SmA-SmC* and TGB_A -SmC* Transitions

The SmA-SmC* and TGB_A -SmC* transitions are shown in Fig. 5-10. The C_p data for the SmA-SmC* transitions show Landau mean-field behavior as explained for achiral SmA-SmC and chiral SmA-SmC* transitions in Chapter 3. No phase shift anomaly has been observed for these transitions, indicating that they are second-order transitions. No SmA-SmC* transition was found in the $n=9$ material, which is consistent with the microscopic texture and DSC results obtained at CRPP.¹² The C_p data of the SmA-SmC* transitions can be well described by the Landau model [see Chapter 3]. The fitting parameters obtained with Eq. (3.14) are given in Table 5-3, and the least-squares best fit lines are shown in Fig. 5-10. The TGB_A -SmC* transition for $n=11$ cannot be

described well by the same model since the C_p data in this case exhibit a small anomaly below the transition (broad “hump” at ~369 K). This small feature may be due to neglected couplings between the polarization P and the tilt angle θ .¹⁶

Table 5-3. Fitting parameters for representing SmA-SmC* transitions with Eq. (3.14) (or Eq. (3.5)). The units are $J K^{-1} g^{-1}$ for A and B , $J K^{-2} g^{-1}$ for E , $J K^{-0.5} g^{-1}$ for A^* , K for T_0 and T_k .

	B	E	A	A*	T ₀	T _k	10 ³ t ₀
n=10	2.039	0.0134	0.031	0.029	367.15	368.06	7.44
n=10.5	2.043	0.0466	0.072	0.083	369.30	370.64	10.9

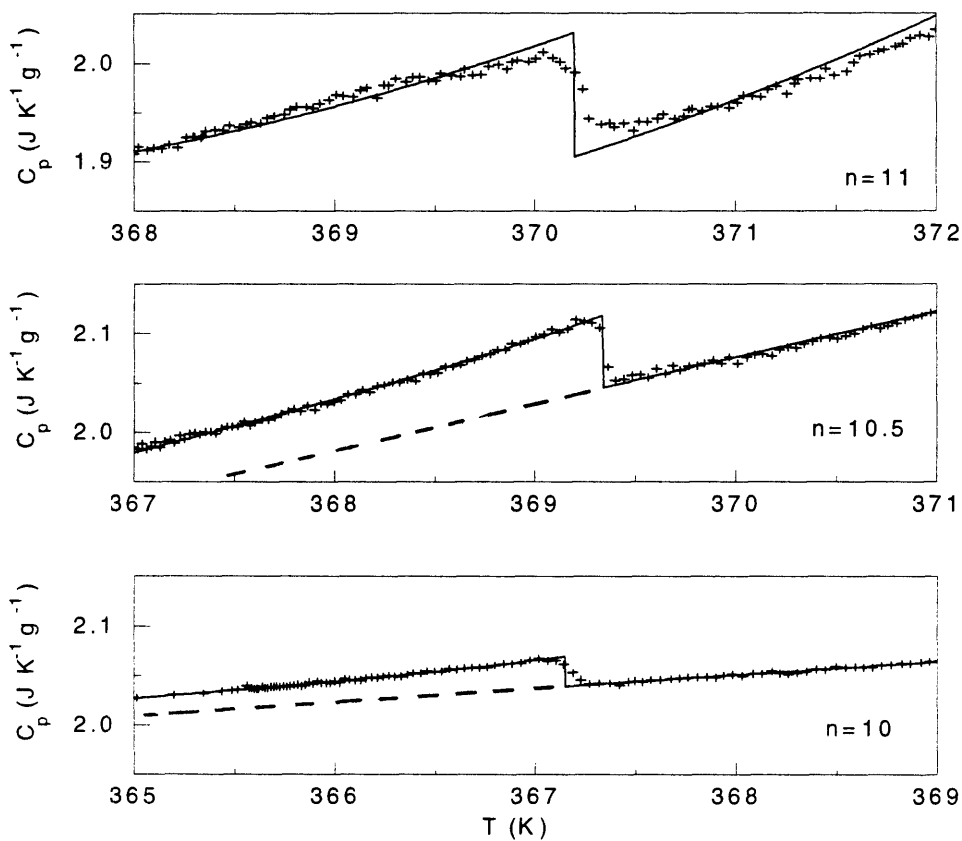


Fig. 5-10. C_p data for SmA-SmC* transitions in nFBTFOM (n=10 and 10.5) and also for the TGB_A-SmC* transition in 11FBTFOM. The lines represent Landau fits, where C_p^0 is given by the dashed line below T_0 . As can be seen, no good Landau fit was possible for 11FBTFOM.

5.4 Relaxation Calorimetry Data

A. N_L^* - TGB_A and TGB_A -SmA Transitions and Feature at T_5

We have stressed that ac calorimetry cannot measure latent heats. In order to confirm the first-order character for the N_L^* - TGB_A and TGB_A -SmA transitions we have carried out measurements on the n=9 material with our relaxation calorimeter (calorimeter B). An effective heat capacity C_{eff} was introduced in Chapter 2, and it will be used here to calculate the latent heats. This effective heat capacity in the T_5 - T_7 transition region is plotted in Fig. 5-11. The C_{eff} data obtained with calorimeter B near the N_L^* - TGB_A and TGB_A -SmA transitions show hysteresis on heating and cooling runs. A comparable hysteresis in the $\tan\phi$ anomalies was observed in ac calorimetry data on n=10 (see Fig. 5-4b). This hysteresis is one indication these transitions are first order. Furthermore, the C_{eff} data in the transition region are anomalously higher than the C_p value obtained in the ac mode indicating that there are latent heat effects. Recall that outside a two-phase coexistence region, the C_{eff} values are identical to the system heat capacity C_p^{sys} . We have compared the C_{eff} data with ac mode data obtained at frequency $\omega_0/9$ in Fig.5-11.

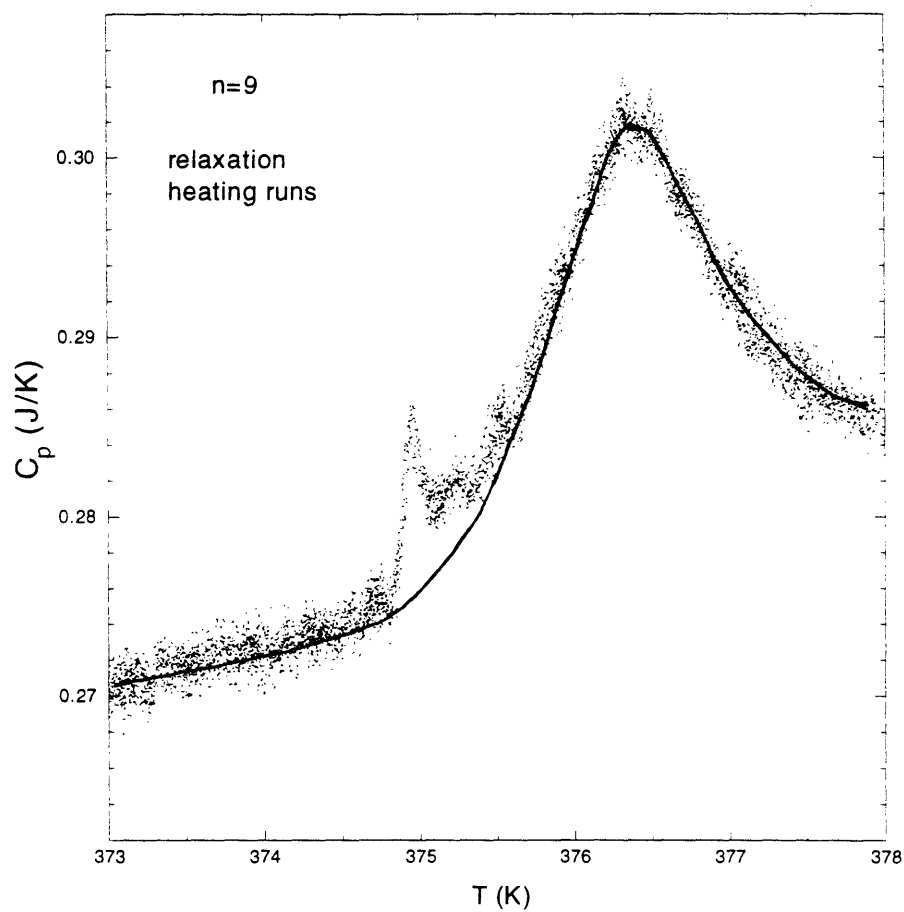


Fig. 5-11. Effective heat capacity of 9FBTFOM in the T_5 - T_7 transition region. Data points were obtained with the new relaxation calorimeter operating in its ramped power (nonadiabatic scanning) mode. The solid line represents ac calorimetry data obtained at $\omega_0/9$.

In the rounded region at T_5 the C_{eff} (relaxation) curve is identical to the C_p (ac) data, indicating that there are no latent heat effects in this rounded region. We have compared (not shown here) ac mode C_p data obtained at ω_0 , $\omega_0/3$, and $\omega_0/9$; no differences could be found. This indicates that there are no finite frequency rounding effects. The rounding of this T_5 feature cannot be due to impurities, since other transitions of the same sample show very sharp peaks. Thus the data near T_5 shown in Fig. 5-11 represent true static C_p values. Since there is no latent heat and no singularity in C_p , we conclude that the rounded feature at T_5 does not correspond to a thermodynamic phase transition. In contrast to that, the $N_L^* - \text{TGB}_A$ (T_6) and $\text{TGB}_A - \text{SmA}$ (T_7) transitions have finite latent heats and are first order.

Latent heats for the $\text{TGB}_A - N^*$ and $\text{TGB}_A - \text{SmA}$ transitions can be calculated by Eq. (2.8) or Eq. (2.10). In Fig. 5-12, the line is our choice for the C_p^{sys} , and the '+' signs represent the C_{eff} values (in units of J/K). Latent heats correspond to the shaded areas. The latent heat for the $N_L^* - \text{TGB}_A$ transition is $8.2 \text{ mJ/g} = 4.95 \text{ J/mole}$, and that for $\text{TGB}_A - \text{SmA}$ transition is $40.1 \text{ mJ/g} = 24.2 \text{ J/mole}$. We must stress that these are very small latent heats.

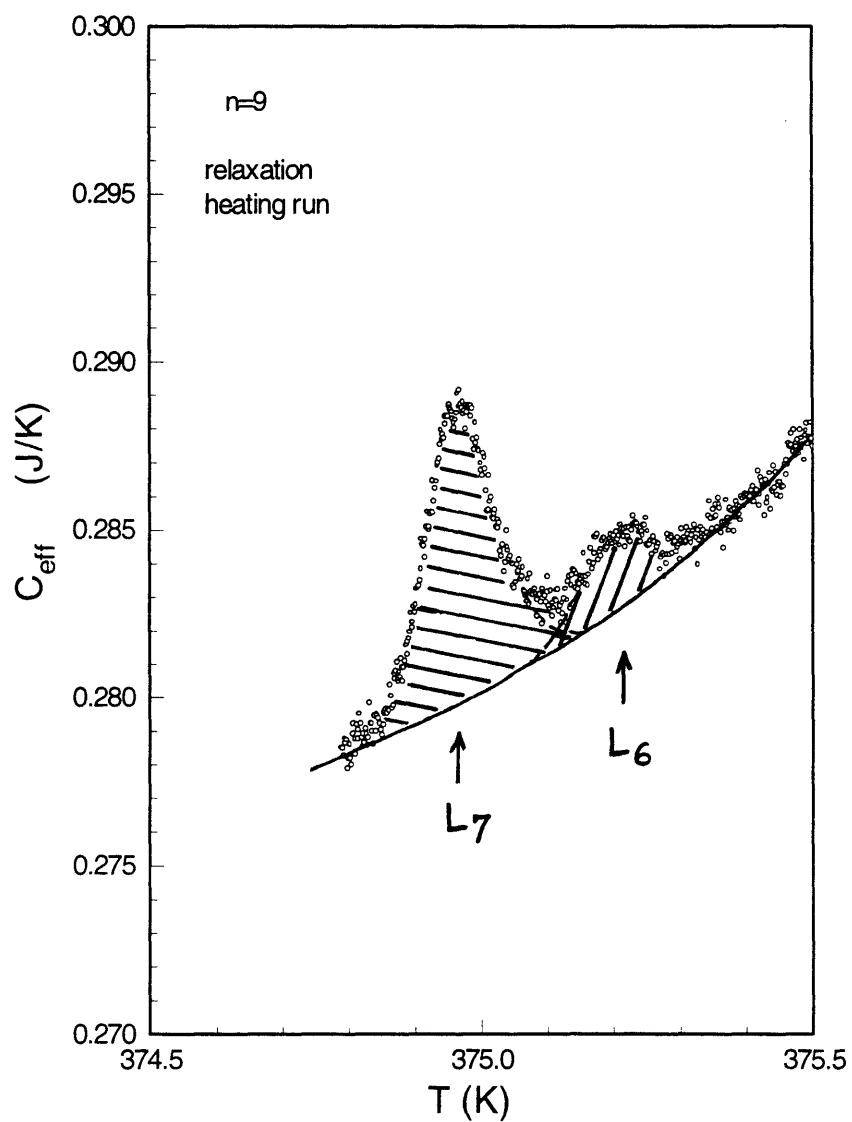


Fig. 5-12. Calculation of latent heats for the $N_L^* - TGB_A$ and $TGB_A - SmA$ transitions in 9FBTFOM.

As mentioned in Chapter 4, the various SmC^* - SmC^* phase transitions of MHPOBC have been detected with relaxation calorimetry. It is found that these are sharp first order transitions with very small latent heats: 12 J/mole = 21.5 mJ/g for SmC^* - SmC_α^* , 16 J/mole = 28.5 mJ/g for SmC_γ^* - SmC^* , and 9 J/mole = 16 mJ/g for SmC_α^* - SmC_γ^* . Another example of phase transitions with similarly small latent heats are the restacking transitions in the plastic crystal B phase of 7O.7 with latent heats 5 to ~15 J/mole = 12.5 to ~38 mJ/g.¹⁷

The latent heats for the N_L^* - TGB_A transition is 4.95 J/mole = 8.2 mJ/g and that for TGB_A - SmA transition is 24.2 J/mole = 40.1 mJ/g. These are among the smallest latent heats ever detected by high-resolution calorimetry in a small sample like ours (32 mg compared to more than 10 g usually used in adiabatic calorimetry).

The author believes that when comparing the resolution of high-resolution calorimeters, one should compare the smallest HEAT that can be detected by the machines, not the latent heats in units of J/mole or J/g. By investigating the data obtained from the relaxation mode, we believe that we have achieved ultra-high resolution thermal analysis with the new Calorimeter B in its nonadiabatic scanning mode operation.

B. BP_{II}-BP_{III} Transition

The BP_{II}-BP_{III} transition for the n=9 material was also investigated with both the ac mode and the relaxation mode. It is found to be first order as expected from J. Thoen's work on blue phase transitions.² In Fig. 5-13 we display the analysis of

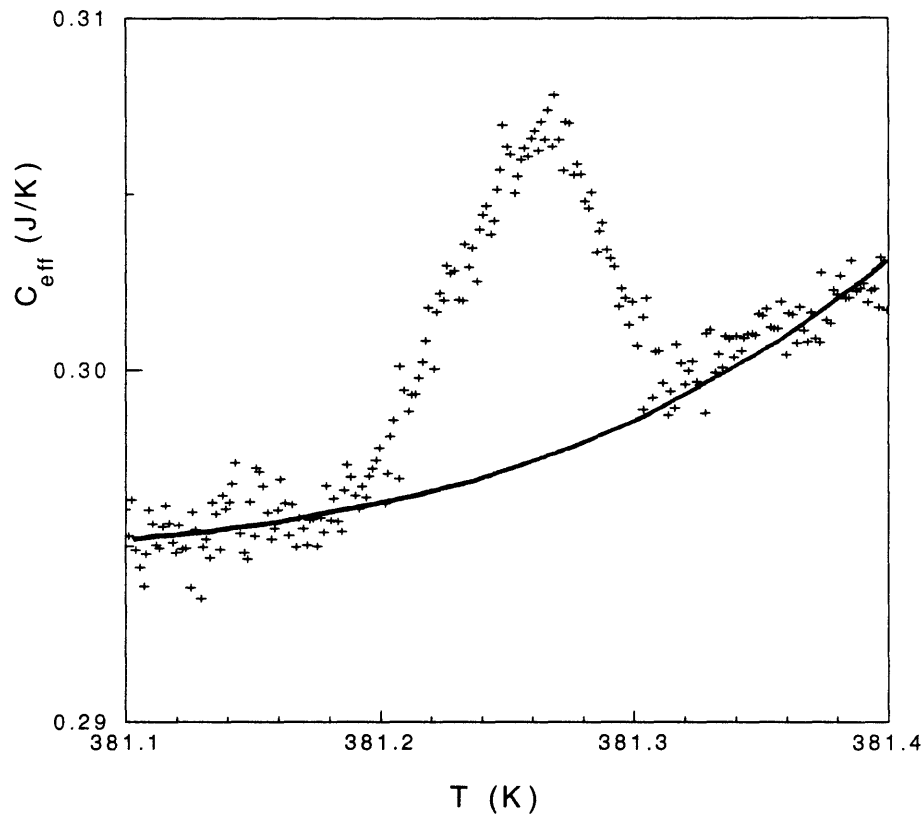


Fig. 5-13. Calculation of the latent heat for the BP_{II}-BP_{III} transition in 9FBTFOM.

the C_{eff} data and the calculation of the latent heat $L = 19.9 \text{ mJ/g} = 12.0 \text{ J/mole}$. This can be compared to Thoen's value of $L = 3.6 \text{ mJ/g} = 1.9 \pm 0.5 \text{ J/mole}$ for the same transition in cholesteryl nonanoate (CN).

5.5 Discussion

We have demonstrated using high-resolution calorimetry that the $N_L^* - \text{TGB}_A$ and $\text{TGB}_A - \text{SmA}$ transitions are first-order and have obtained the latent heats for these transitions. We also demonstrated that above the $N_L^* - \text{TGB}_A$ transition temperature and inside the range of the N^* phase, there is a rounded C_p feature (T_5) indicating large enthalpy changes but no thermodynamic phase transition.

Our experimental results on the TGB materials may provide useful information about the corresponding phase transitions in superconductors. In Table 5-1 we listed detailed information about the superconductor-liquid crystal analogy.⁵ According to this analogy, the TGB_A phase corresponds to the Abrikosov flux vortex lattice phase. Thus the $N_L^* - \text{TGB}_A$ transition at T_6 is analogous to the melting of the Abrikosov lattice, which is found to be first order in some high- T_c superconductors.⁴ The experimental evidence for this first-order character in superconductors is hysteresis in the transport properties at finite fields. So far it seems there are no thermodynamic measurements on this transition in type II

superconductors although theory predicts first order.¹⁸ If we make the mapping between smectic liquid crystals and superconductors, our thermodynamic measurements on these TGB_A materials confirms that the melting of an Abrikosov vortex lattice is a first-order transition. The region between T_6 and T_5 (where the large rounded C_p feature has its maximum) for our chiral liquid crystal samples, denoted by N_L^* , can be mapped onto a vortex liquid state in superconductors. The TGB_A -SmA transition corresponds to the transition of the Abrikosov vortex lattice into the Meissner phase, and our results indicate clearly that it is a first-order transition. See Fig. 5-14 for a sketch of the universal phase diagram for type-II superconductors and chiral liquid crystal paths for $n=9,10,11$ materials.

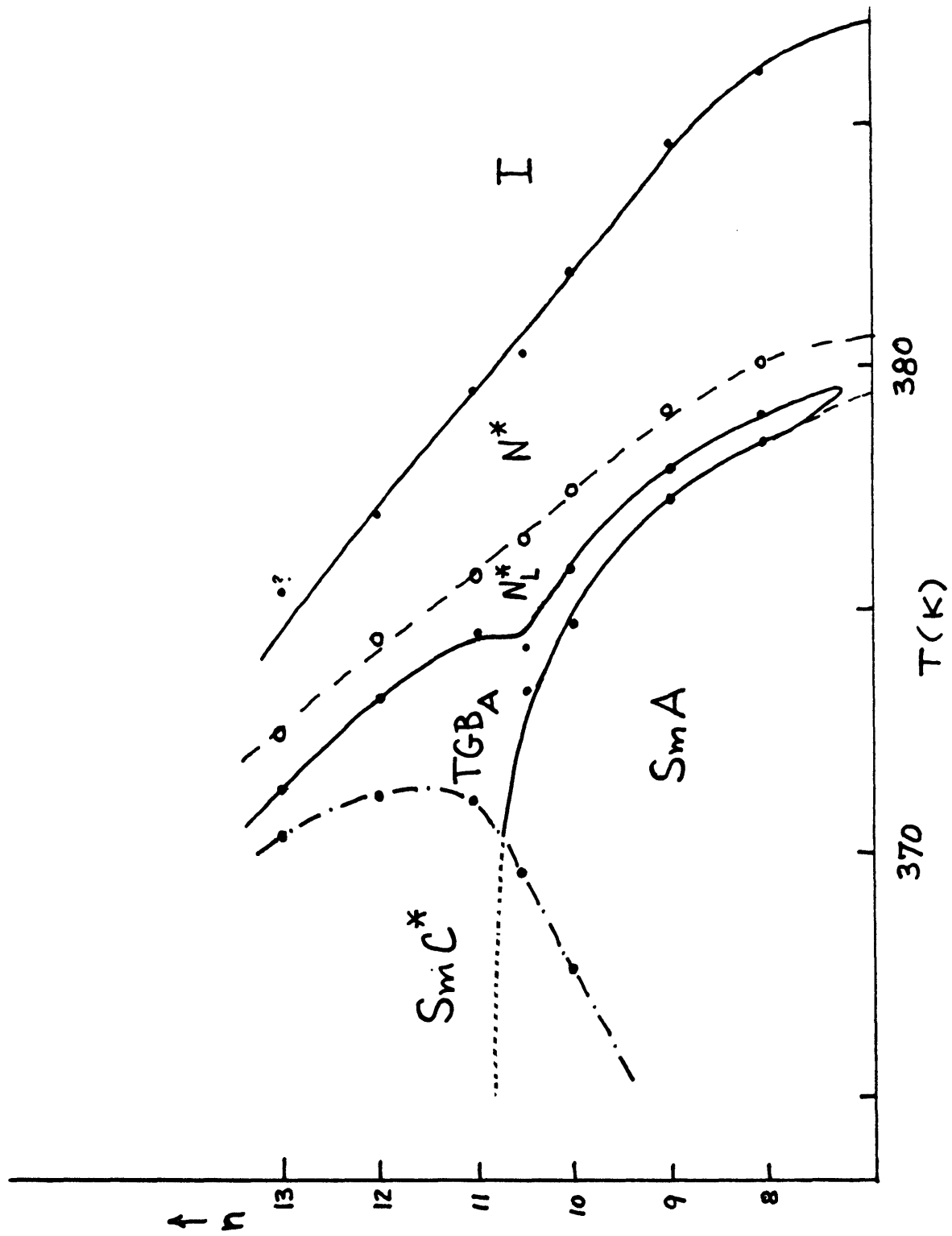


Fig. 5-14. Universal phase diagram for type-II superconductors and chiral liquid crystals.

References

1. D.C. Wright, and N.D. Mermin, Rev. Mod. Phys. 61, 385 (1989).
2. J. Thoen, Phys. Rev.A37, 1754 (1988).
3. P.G. de Gennes, Solid State Common. 10, 753 (1972).
4. D.S. Fisher, M.P.A. Fisher, D.A. Huse, Phys. Rev. B 43, 130 (1991)
5. S.R. Renn and T.C. Lubensky, Phys. Rev.A 38, 2132 (1988).
6. J.W. Goodby, M.A. Waugh, S.M. Stein, E. Chin, R. Pindak, and J. Patel, Nature (London), 337, 449 (1989).
7. G. Srajer, R. Pindak, M.A. Waugh, and J.W. Goodby, Phys. Rev. Lett. 64, 1545 (1990).
8. K.J.Ihn, J.A.N.Zasadzinski, R.Pindak, A.J.Slaney, J.Goodby, Science 258, 275 (1992).
9. S.R. Renn and T.C. Lubensky, Mol. Cryst. Liq. Cryst., 209, 349 (1991).
10. T.C. Lubensky and Y. Hatwalne, 15th International Liquid Crystal Conference, Budapest July 1994.
11. L. Navailles, P. Barois and H.T. Nguyen, Phys. Rev. Lett., 71, 545 (1993).
- 12.A. Bouchta, H.T. Nguyen, M.F. Achard, F. Hardouin, C. Destrade, R.J. Twieg, A. Maaroufi and N. Isaert, Liq. Cryst. 12, 575 (1992).
- 13.P.F. Sullivan and G. Seidel, Phys. Rev. 173, 679 (1968); J.D. Baloga and C.W. Garland, Rev. Sci. Instrum. 48, 105

- (1977); J.M. Viner, D. Lamey, C.C. Huang, R. Pindak, and J. W. Goodby, Phys. Rev. A, 28, 2433 (1983).
14. R. D. Kamien and T.C. Lubensky, J. Phys.I, 3, 2123 (1994).
 15. H. Yao, T. Chan, C.W. Garland, to appear in Phys. Rev. E
 16. T. Carlsson, B. Zeks, C. Filipic, A. Levstik, and R. Blinc, Mol. Cryst. Liq. Cryst. 163 , 11 (1988).
 17. J. Thoen and G. Seynhaeve, Mol. Cryst. Liq. Cryst. 127, 229 (1985).

Chapter 6

Suggestions For Future Work

Calorimeter A and Calorimeter B described in Chapter 2 have been demonstrated to be high-resolution calorimeters. However, further improvements could be made.

6.1 Nonadiabatic Scanning Calorimetry

One possibility is to carry out continuous scanning over a wide range of temperature in the linear power mode, in the same style as adiabatic scanning calorimetry and DSC. This will make the measurements more efficient and will not lose any information during the “hold” period in our current method. It is obvious that one can not measure the thermal resistance R in this continuous mode, but R can be measured in a separate run with the current method. One should also try to increase the thermal resistance. This will keep the heat leak small and reduce the uncertainties in C_p data from relaxation mode measurements.

6.2 Calorimetry Spectroscopy

The heat capacity is usually regarded as a static property. However, some researchers have generalized the concepts and studied “dynamic heat capacity” or “frequency dependent heat

capacity". The ac calorimetry described in Chapter 6 can be used for this kind of calorimetry spectroscopy.¹

Actually, the ac calorimetry data obtained outside the two-phase coexistence region can only be interpreted as the static heat capacity if the operation frequency is low enough (data obtained with relaxation mode can better represent the static heat capacity.¹). By changing the operating frequency in ac calorimetry, one can analyze the real part as well as the imaginary part of the complex heat capacity $C_p^*(\omega)$.¹

Reference

1. H. Yao, T. Chan, and C. W. Garland, Phys. Rev. E, to appear.